Title
The Evolution and Stability of Massive Stars

Author
SHIODE, JOSHUA HAJIME

Publication Date
2013

Peer reviewed|Thesis/dissertation

The Evolution and Stability of Massive Stars

By

Joshua Hajime Shiode

A dissertation submitted in partial satisfaction of the

requirements for the degree of

Doctor of Philosophy

in

Astrophysics

in the

Graduate Division

of the

University of California, Berkeley

Committee in charge:

Professor Eliot Quataert, Chair
Professor Steven E. Boggs
Professor Daniel Kasen
Professor Christopher McKee

Fall 2013

The Evolution and Stability of Massive Stars

Abstract

The Evolution and Stability of Massive Stars

by

Joshua Hajime Shiode

Doctor of Philosophy in Astrophysics

University of California, Berkeley

Professor Eliot Quataert, Chair

Massive stars are the ultimate source for nearly all the elements necessary for life. The first stars forge these elements from the sparse set of ingredients supplied by the Big Bang, and distribute enriched ashes throughout their galactic homes via their winds and explosive deaths. Subsequent generations follow suit, assembling from the enriched ashes of their predecessors. Over the last several decades, the astrophysics community has developed a sophisticated theoretical picture of the evolution of these stars, but it remains an incomplete accounting of the rich set of observations. Using state of the art models of massive stars, I have investigated the internal processes taking place throughout the life-cycles of stars spanning those from the first generation ("Population III") to the present-day ("Population I"). I will argue that early-generation stars were not highly unstable to perturbations, contrary to a host of past investigations, if a correct accounting is made for the viscous effect of convection. For later generations, those with near solar metallicity, I find that this very same convection may excite gravity-mode oscillations that produce observable brightness variations at the stellar surface when the stars are near the main sequence. If confirmed with modern high-precision monitoring experiments, like *Kepler* and *CoRoT*, the properties of observed gravity modes in massive stars could provide a direct probe of the poorly constrained physics of gravity mode excitation by convection. Finally, jumping forward in stellar evolutionary time, I propose and explore an entirely new mechanism to explain the giant eruptions observed and inferred to occur during the final phases of massive stellar evolution. This mechanism taps into the vast nuclear fusion luminosity, and accompanying convective luminosity, in the stellar core to excite waves capable of carrying a super-Eddington luminosity out to the stellar envelope. This energy transfer from the core to the envelope has the potential to unbind a significant amount of mass in close proximity to a star's eventual explosion as a core collapse supernova.

For my parents, who have supported me
in everything I have ever pursued.
I love you.

Contents

List of Figures

List of Tables

Acknowledgments

My path to a Ph.D. has been anything but straight. I have had many ups and downs, deep doubts and moments of clarity. But for all the trials, I am incredibly happy and grateful to have had the opportunity to learn, teach, study and discover alongside the amazing people I have come to know here at Berkeley. I feel so fortunate to have developed lifelong friends and colleagues among the staff, faculty, postdocs and students here, who have each helped me get through the trials and celebrate the successes.

To my research advisor, Eliot Quataert, I am deeply grateful for the time and knowledge you have shared with me over the last six years. Since even before we began working together, you have been a tremendous source of insight into the workings of the universe and the process of scientific research. I aspire to be as broadly knowledgeable and generous with that knowledge as I know you to be.

To my friends and colleagues in The Compass Project, you gave me a place to feel at home when I felt adrift as a graduate student. I am so excited to see all the amazing things Compass is doing as it continues to grow and become even better than the already wonderful organization I joined in 2010. And thank you to the Coalites, who expanded the home I found in Compass, and are among the most important reasons I am finding my way into an exciting, impactful career.

To the students I've taught over the years, you taught me more about myself and how to communicate the depth and beauty of science than you know.

To my friend Justin, I may never have made it to this point if it were not for our conversations and the understanding you helped me find. It is of course always a work in progress, but I am so much farther along today thanks to you.

To my friends and family, I love you all. Thank you for all your support and encouragement.

Chapter 1

Introduction

1.1 The evolution of massive stars

The nuclear fusion reactors in the cores of massive stars synthesize the elements necessary for all of life on earth (Burbidge et al. 1957).[1] Through their radiative output, stellar winds, and often violently explosive deaths, these stars also dominate the energy injection into the interstellar media of their host galaxies (McKee 1986). And yet, despite decades of study, there remain significant gaps in our understanding of how massive stars evolve from birth to death. Which combinations of initial mass, metallicity, angular momentum, and stellar multiplicity lead to the observed populations of red and blue supergiants (R/BSG), Luminous Blue Variables (LBV) and Wolf-Rayet (WR) stars? And which to each of the many classes of supernovae (SNe) and varieties of stellar remnants? These are just a sample of the big questions we face, and each requires better understanding of the details of massive stellar evolution. In the following, I will propose new solutions and more refined questions that will help propel us forward in our attempts to understand the lives and deaths of massive stars.

Viewed from their cores, the evolution of massive stars is a relatively simple story of the fusion of successively heavier and more positively charged elements: from hydrogen and helium to carbon, neon and oxygen and on to the iron-peak elements (e.g., Burbidge et al. 1957; Clayton 1984; Kippenhahn & Weigert 1990). Most of these burning phases drive convection in the core and subsequently in shells of matter overlying the inert ashes of a previous phase (Woosley et al. 2002). Once a sufficiently large iron core is assembled from the ashes of Silicon burning, it overcomes the support of degeneracy pressure and collapses to form a neutron star or black hole, potentially accompanied by a brilliant SN display (Woosley et al. 2002). But to stop at this level of description is to overlook a variety of insufficiently answered questions about the extent of mixing by convection (e.g., Browning et al. 2004; Lebreton & Goupil 2012), turbulent entrainment (Meakin & Arnett

[1] For the rest of this work, I will use the term "massive star" to refer to any star that will eventually undergo core collapse, which may or may not give rise to a supernova (SN).

2007), double-diffusive (Langer et al. 1983; Merryfield 1995; Rosenblum et al. 2011) and shear-induced instabilities (Maeder & Meynet 2000; Heger et al. 2000); not to mention the secondary effects, like the excitation of waves at boundaries between convective and radiative zones (Meakin & Arnett 2007; Quataert & Shiode 2012).

Outside the core, the envelope of a massive star undergoes its own complicated evolution. On the main sequence, we naively expect a massive star to have a radiative envelope sitting atop its convective core, shining at nearly its Eddington limit (Eddington 1926; Henyey et al. 1964; Kippenhahn & Weigert 1990). This radiative envelope contains an ever smaller fraction of the stellar mass as the total mass increases (Kippenhahn & Weigert 1990; Woosley et al. 2002). However, Rogers & Iglesias (1992), in their computation of the OPAL opacities in the early nineties, showed that metal absorption lines provide enhanced opacity at $\log \mathrm{T} \approx 5.2$, which has important consequences for the envelopes of massive stars with near-Solar metallicity. With the envelope already near the Eddington limit for electron scattering, this enhanced opacity causes thin shell convection zones to develop due to the locally super-Eddington flux; these near-surface convection zones excite waves that can explain the velocity fields observed at the surfaces of massive stars (Cantiello et al. 2009). This opacity enhancement may also produce a variety of fast-acting pulsational instabilities that could lead to enhanced mass loss (e.g., Glatzel & Kiriakidis 1993; Cantiello et al. 2009; Saio 2011). Most calculations suggest that massive stellar envelopes are likely to become *even more unstable* during later evolutionary phases, as they lose mass while attempting to carry an ever-increasing nuclear fusion luminosity (e.g., Yoon & Cantiello 2010; Glatzel 2008; Saio 2011; Suárez-Madrigal et al. 2013).

At their very surfaces, massive stars are being vigorously eroded by strong stellar winds (e.g., Heger et al. 2003; Vink 2011). On the main sequnce, they are subject to intense winds driven by radiation pressure on metal lines in their atmospheres, leading to mass loss rates that can approach $\sim 10^{-4}\,\mathrm{M}_\odot\,\mathrm{yr}^{-1}$ (Castor et al. 1975; Lamers & Cassinelli 1999; Vink 2011). The driving mechanism for these winds is subject to clumping instabilities (Owocki 2009, and references therein), and recent investigations have begun to quantify the extent of this clumping for several example massive stars. As a result, it seems that empirical estimates of steady mass loss rates have been overestimated (perhaps by as much as a factor of 30) (e.g., Bouret et al. 2005; Fullerton et al. 2006). This implies a significant discrepancy between observed stellar populations and theoretical evolution calculations, requiring some additional mass loss mechanism separate from the steady winds expected during hydrogen and helium-burning (Smith & Owocki 2006; Smith 2011). Luckily, just such a mechanism has made itself highly conspicuous: eruptive mass loss.

The most prevalent examples of eruptive mass loss, which I define as short (in an evolutionary sense) periods of mass loss enhanced relative to steady-state wind expectations ($\dot{M} \gtrsim 10^{-3}\,\mathrm{M}_\odot\,\mathrm{yr}^{-1}$), come from observations of the class of post-main-sequence stars known as LBVs. While LBVs exhibit a range of mass loss behaviors, the most intense of these is often referred to as a "giant eruption," with the prime example being that of η Carinae over the period from about 1837–1860 (Humphreys & Davidson 1994). During this period, the

$\gtrsim 100\,M_\odot$ star shed $\sim 20\,M_\odot$ at a rate of $\sim 1\,M_\odot\,yr^{-1}$, for a total kinetic energy loss of $\lesssim 10^{50}$ erg (Smith et al. 2003). The cause of giant eruptions like these remains unexplained.

The canonical scenarios for the apparent evolution of massive stars dictate that LBVs are massive stars in a state of hydrogen shell burning as they make their way from the main sequence to RSG (and/or BSG) to WR star, where the specific progression and timescales depend on the initial mass, metallicity and rotation (e.g., Massey 2003). However, evidence has been piling up during the last decade of rapid advances in transient astronomy that some fraction of SN progenitors have mass loss properties similar to erupting LBVs within $\lesssim 1000$ years of explosion—much less than the 10^5 years these stars are presumed to spend burning helium *after* going through an LBV phase (Smartt 2009, and references therein). This is particularly significant given the traditional assumption that the stellar envelope and surface are basically static from carbon burning to core collapse, since the thermal time of the envelope is long relative to this phase of evolution (e.g., Woosley et al. 2002).

There are now dozens of examples of core collapse supernovae that require large pre-explosion mass loss rates, $\dot{M} \gtrsim 10^{-4}\,M_\odot\,yr^{-1}$, to explain their visual appearance. These are generally (but not always, see e.g., Foley et al. 2007) of the class known as Type IIn (Schlegel 1990), which gets its "n" from the narrow emission lines (full-width at half maximum intensity $\sim 100 - 1000\,km\ s^{-1}$) seen in their spectra (see Filippenko 1997, for a review). The standard model used to interpret the emission from this class of SNe involves the interaction of the SN ejecta with a dense, but optically-thin, photoionized wind previously ejected from the progenitor (e.g., Chevalier & Fransson 1994; Chugai & Danziger 1994). When the ejecta runs into this circumstellar material (CSM), it generates forward and reverse shocks that propagate into the wind and back into the ejecta, respectively. These are separated by a contact discontinuity and bound a dense shell of material traveling at speeds intermediate between the velocities of the ejecta $\sim$ few $\times\, 10^4\,km\ s^{-1}$ and the unshocked wind $\sim 100 - 1000\,km\ s^{-1}$. This manifests spectroscopically in emission line profiles with intermediate-width and narrow components corresponding to the dense shell and unshocked wind, respectively. Using this model, large pre-explosion mass loss rates are derived from measurements of the emission line luminosity (e.g., Chugai & Danziger 1994; Kiewe et al. 2012).

Varying the mass loss history in terms of both rates ($\dot{M} \sim 10^{-4} - 1\,M_\odot\,yr^{-1}$) and time to core collapse ($\Delta t \sim$ days $- 1000\,yr$), the interaction between SN ejecta and CSM can account for a broad range of SN characteristics, from "normal" Type IIn SNe to some of the most luminous SNe ever observed (e.g., Kiewe et al. 2012; Ginzburg & Balberg 2012; Gal-Yam 2012). For large enough wind densities (which depends on both the mass loss rate and inversely on the wind velocity), the CSM can become optically thick enough to maintain the radiative SN shock beyond the progenitor photosphere. In this case, the "shock breakout," when the radiation from the shock escapes ahead of the shock propagation, occurs in the wind, where more of the shock kinetic energy can be radiated (Falk & Arnett 1977; Chevalier & Irwin 2011; Ginzburg & Balberg 2012; Moriya & Tominaga 2012). Interaction models with a dense CSM as described above can explain some of the most luminous SNe

observed (Smith & McCray 2007; Miller et al. 2009; Gal-Yam 2012). In the particular case of 2006gy, this type of model implies $\sim 10 - 30\,M_\odot$ of CSM ejected within $\sim 10\,yr$ of explosion (Smith & McCray 2007; Ginzburg & Balberg 2012).

Finally, the most direct line of evidence for eruptive mass loss stems from the direct observation of non-terminal outbursts that approach the brightnesses of the faintest SNe. Some of these precede SNe by days to years, as in the brilliant cases of SN 2006jc (Pastorello et al. 2007; Foley et al. 2007), 2010mc (Ofek et al. 2013), and potentially 2009ip (Mauerhan et al. 2013; Fraser et al. 2013). Other events without subsequent SNe have been observed and are collectively known by the observationally-derived, but obfuscating name: SN Imposters (Van Dyk & Matheson 2012).

1.1.1 The scope of this work

This dissertation will attempt to address discrepancies between observations and theory during both the main sequence and final burning stages of massive stellar evolution. I will apply perturbative theory and the recent advances in our understanding of stellar convection coming from high-fidelity numerical simulations to inspect the stability of models of massive main sequence stars of a range of metallicities. Using these methods, I will show that high metallicity stars of $\sim 100\,M_\odot$ may be violently unstable on the main sequence, while the earliest generations of stars are stabilized by the viscous effect of convection (Chapter 2). For lower masses, this very same convection in the stellar core excites gravity-mode oscillations which may be observable thanks to the recent development of part-per-million-precision photometric monitoring with *Kepler* (Koch et al. 2010) and *CoRoT* (Auvergne et al. 2009) (Chapter 3). Observing these modes would provide an important new window into the physics of gravity-wave excitation by convection, which is otherwise unobservable even in our closest stellar laboratory: the Sun.

Perhaps most excitingly, I will propose an entirely new mechanism for generating eruptions during the final phases of stellar evolution: one that relies on the vigorous convection taking place in the bellies of these beasts (Chapter 4). In these late phases, the convection is so strong that, rather than excite gravity-modes with observable, steady-state surface amplitudes, it can excite dynamic gravity waves capable of transporting energy, via a process analogous to quantum mechanical tunneling, from the neutrino-cooled core to the stellar envelope. Once there, this wave energy has the potential to violently expel solar masses worth of material shortly before the star's explosive death. This may provide a natural explanation for the precursor events of SN 2006jc, 2009ip, and 2010mc, as well as the massive circumstellar environments inferred to exist around the progenitors of Type IIn SNe.

Before we get into any of that, there are a few theoretical preliminaries to address. In §1.2, I describe the basic procedure for constructing and evolving the one-dimensional numerical models of massive stars used throughout this work. In practice, I use the `MESA star` stellar evolution code to compute stellar models, so I refer the reader to Paxton et al.

(2011) and Paxton et al. (2013) for a detailed description of the specific implementation used in `MESA star`. In Chapters 2 and 3, I investigate the effects of perturbations on top of the equilibrium models built with `MESA star`. Thus in §1.3, I describe the formalism I use to describe quasi-adiabatic linear non-radial stellar oscillations.

1.2 How to build a star

From a theoretical perspective, the problem of stellar evolution is the challenge of solving a set of nonlinear, coupled differential equations for the thermodynamic and compositional structure of a self-gravitating ball of gas in a series of quasi-equilibrium (both hydro and thermodynamic) configurations (e.g., Henyey et al. 1964; Eggleton 1971; Paxton et al. 2011). The equations that must be solved include:

$$\frac{dr}{dm_r} = \frac{1}{4\pi r^2 \rho}, \tag{1.1}$$

$$\frac{dP}{dm_r} = -\frac{Gm_r}{4\pi r^4} - \frac{1}{4\pi r^2}\frac{d^2 r}{dt^2}, \tag{1.2}$$

$$\frac{dL}{dm_r} = \epsilon_{\rm nuc} - \epsilon_\nu - T\frac{ds}{dt}, \tag{1.3}$$

$$\frac{dT}{dm_r} = -\frac{Gm_r T}{4\pi r^4 P}\nabla_\star, \tag{1.4}$$

$$\frac{dX_i}{dt} = \left(\frac{dX_i}{dt}\right)_{\rm nuc} + \left(\frac{dX_i}{dt}\right)_{\rm mix}, i = 1, ..., {\rm N}_{\rm species}, \tag{1.5}$$

where G is the gravitational constant, the two time derivatives on the right-hand side of eqn. 1.5 are the change in composition due to nuclear burning and mixing, respectively, and the rest of the variables are defined in Table 1.1. These equations, along with appropriate boundary conditions for the center and surface of the stellar model, serve to define the stellar evolution problem. The scope of this numerical challenge depends on the spatial resolution of each model, the number of species (X_i) one wishes to track, and the desired temporal resolution for the evolution.

To construct the one-dimensional numerical models of massive stars I use throughout this dissertation, I employed the new, open-source `star` stellar evolution program in the Modules for Experiments in Stellar Astrophysics (`MESA`; Paxton et al. 2011, 2013).[2] `MESA star` solves the set of equations described above (eqns. 1.1 – 1.5) using modern computing algorithms for large matrices (see Paxton et al. 2011, for a detailed description). As an open-source tool, `MESA star` has been tested and extended by hundreds of users as part of an open online community of modelers. This community has shown `MESA star`'s capability to model the evolution of everything from gas giant planets with rocky cores to super-massive

[2] As `MESA` is under continuous development, I have employed several different versions of `star` for the investigations presented here.

Table 1.1: List of variables used in the text

Name	Description
$\alpha_{\rm MLT}$	Fraction of pressure scale height for mixing length
α_{sc}	Dimensionless efficiency of semiconvective mixing
β	Fraction of wave energy that reaches the envelope
c_s	Speed of sound
$\gamma_{\rm rad}$	Damping rate due to radiation
$\gamma_{\rm leak}$	Damping rate of g-modes due to leakage out of g-mode cavity
γ_ν	Damping rate due to neutrino losses
Γ_1	$\equiv \left(d\ln P/d\ln\rho\right)_s$
Γ_3	$\equiv \left(d\ln T/d\ln\rho\right)_s + 1$
$e_{\rm int}$	Internal energy per unit mass
$\rm E_{bind}$	Stellar binding energy
$\dot{E}_g$	Energy input into g-modes by convection
$\epsilon_{\rm nuc}$	Nuclear energy generation rate per unit mass
ϵ_ν	Neutrino emission rater per unit mass
$\epsilon_{\rm grav}$	$\equiv -T\frac{dS}{dt}$, gravitational energy generation rate
$\epsilon_{\rm net}$	$\equiv \epsilon_{\rm nuc} - \epsilon_\nu - \epsilon_{\rm grav}$, net energy generation rate per unit mass
ϵ_ρ	$\equiv \left(d\ln\epsilon/d\ln\rho\right)_T$
ϵ_T	$\equiv \left(d\ln\epsilon/d\ln T\right)_\rho$
$\vec{F}$	Local stellar flux
g	Local gravity
H	Pressure scale height
η	Overshoot fraction of scale height
$K_{\rm rad}$	Radiative conductivity
k_r	Radial wavenumber
k_h	Horizontal ($\perp r$) wavenumber
κ	Rosseland mean opacity
L_r	Stellar luminosity as a function of radius
$L_\star$	Total stellar luminosity
$\rm L_{conv}$	Convective luminosity
$\rm L_{max,\,conv}$	Maximum luminosity convection can carry
$\rm L_{damp}$	Radiative damping luminosity for acoustic waves (see Chapter 5)
$\rm L_{Edd}$	$\equiv 4\pi GM_\star c/\kappa$, Eddington luminosity
$\rm L_{rad}$	Radiative luminosity
$\rm L_{wave}$	Wave luminosity (for convectively excited waves)
$\mathcal{L}$	$\equiv \min(r, H)$, convective mixing length
ℓ	Spherical harmonic quantum number

Continued on Next Page...

Table 1.1 — Continued

Name	Description
Λ	$\equiv \sqrt{\ell(\ell+1)}$
m_r	Mass interior to given point in star
M_{ad}	Adiabatic mass (containing part of star where $t_{\rm therm} \gtrsim \tau_{\rm mode}$)
$M_\star$	Total stellar mass
$\mathrm{M_{ej}}$	Mass ejected via wave-driven mass loss
$\mathcal{M}_{\rm conv}$	$\equiv v_{\rm conv}/c_s$, convective mach number
δm	Surface brightness perturbation due to oscillation mode
μ	Convective viscosity
N	Brunt-Väisälä frequency
$\nabla_{\rm ad}$	$\equiv (d\ln T/d\ln P)_s$, adiabatic temperature gradient
$\nabla_\star$	$\equiv d\ln T/d\ln P$, actual temperature gradient
ν	Linear frequency (of waves)
ν_c	Linear convective turnover frequency
ξ_r	Magnitude of radial displacement for perturbation
ξ_h	Magnitude of horizontal ($\perp r$) displacement of perturbation
ω	Angular frequency of perturbation
ω_{ac}	Acoustic cutoff frequency
ω_c	Outer convective turnover frequency
$\omega_\star$	$\equiv GM_\star/R_\star^3$, stellar natural frequency
Ω	Rotation angular frequency
$\delta\omega$	Imaginary component of oscillation mode frequency
P	Total pressure
ϕ	Azimuthal angle
Φ	Gravitation potential
r	Radius coordinate in star
$r_{\rm damp}$	Radius where $\mathrm{L_{rad}} = \mathrm{L_{damp}}$ (see Chapter 5)
$r_{\rm in}$	Radius of the bottom of a mixed mode's evanescent zone (see Chapter 4)
$r_{\rm out}$	Radius of the top of a mixed mode's evanescent zone (see Chapter 4)
$r_{\rm prop}$	Radius where excited g-mode begins to propagate (see Chapter 4)
R_{ad}	Adiabatic radius (containing part of star where $t_{\rm therm} \gtrsim \tau_{\rm mode}$)
$R_\star$	Radius of photosphere
ρ	Density
ρ_c	Central density
s	Entropy per unit mass
S_ℓ	Lamb frequency for perturbations of spherical harmonic number ℓ
t	Time
$\mathrm{t_{nuc}}$	Nuclear burning timescale

Continued on Next Page...

Table 1.1 — Continued

Name	Description
$t_{\rm therm}$	Thermal (Kelvin-Helmholtz) timescale
T	Temperature
$T_{\rm eff}$	Stellar effective temperature
$\tau_{\mathcal{L}}$	$\equiv 1/N$, convective turnover time of the largest eddies
$t_{\rm leak}$	Timescale for leakage out of the g-mode cavity (see Chapter 5)
$\tau_{\rm mode}$	Mode period
t_{ν}	Timescale for damping to neutrinos (see Chapter 5)
τ_{w}	Wave optical depth
θ	Polar angle
$v_{\rm esc}$	Escape velocity
$v_{\rm group}$	Group velocity of wave
v_{r}	Radial velocity (associated with pulsation)
δv	Surface velocity perturbation due to oscillation mode
x	$\equiv r/R_{\star}$, fractional radius
X_i	Mass fraction of species i
X_{ctr}	Central mass fraction of hydrogen
Y	Helium mass fraction
$Y_{\ell}^{m}(\theta,\phi)$	Spherical harmonic of degree ℓ and order m
Z	Metallicity (mass fraction)

($\mathrm{M} \sim 1000\,\mathrm{M}_{\odot}$), first-generation stars. More detailed descriptions of the specific stellar models used are left to the methods sections of each of Chapters 2, 3, and 4.

1.3 How to make a star ring: quasi-adiabatic stellar oscillations

In Chapters 2 and 3, I investigate the stability and observability of stellar oscillations in a range of main sequence stellar models. In these investigations, I consider the response of stars to general, non-spherically symmetric perturbations and the subsequent driving and damping of the oscillation modes these perturbations excite. In Chapter 4, I am not concerned with the standing oscillation modes I consider in the previous two chapters, but still employ the physics of wave propagation in stars to understand energy transport during their final burning stages. Below, I present a formalism for describing the propagation and energetics of waves in stellar interiors.

In the following chapters, I employ the formalism of linear non-radial oscillations, with an assumption of quasi-adiabaticity to simplify the calculations (cf., Unno et al. 1989). In practice, I use the `ADIPLS` oscillation package distributed with `MESA` (Christensen-Dalsgaard

2008a, June 2011 release) to compute *adiabatic* oscillation eigenfunctions and frequencies, and then compute the next-order perturbations to the energy transport given the stellar model and eigenfunctions as background conditions. I refer the reader to Christensen-Dalsgaard (2008b) and the lecture notes at `http://users-phys.au.dk/jcd/oscilnotes/` for a detailed description of the computation of adiabatic linear non-radial oscillations and the specifics of `ADIPLS`. Below I provide a simplified description of the quasi-adiabatic mode calculations performed for this work.

1.3.1 Adiabatic linear non-radial oscillations

To derive the equations that describe adiabatic linear non-radial oscillations, I perturb the equations of stellar structure, described above in eqns. 1.1 – 1.4, under the assumption that perturbations are adiabatic (cf., Unno et al. 1989). I introduce small, Eulerian perturbations such that for each variable, $f(\vec{r},t) \rightarrow f_0(r) + f'(\vec{r},t)$ where $f_0(r)$ satisfies the equilibrium equations. I assume that the perturbations are of the form $f'(\vec{r},t) = f'(r)Y_\ell^m(\theta,\phi)e^{i\omega t}$ and that the perturbations are adiabatic in a Lagrangian sense, i.e., $\delta P/P = \Gamma_1 \delta\rho/\rho$, where $\delta x = x' + \delta r \cdot \nabla x$, for all x.

The resulting fourth-order set of linear, ordinary differential equations may be solved, with appropriate boundary conditions, for the oscillations supported by a star. As presented in many other references, these equations are:

$$\frac{d\xi_r}{dr} = -\left(\frac{2}{r} + \frac{1}{\Gamma_1 P}\frac{dP}{dr}\right)\xi_r + \frac{1}{\rho c_s^2}\left(\frac{S_\ell^2}{\omega^2} - 1\right)P' + \frac{\ell(\ell+1)}{\omega^2 r^2}\Phi' \tag{1.6}$$

$$\frac{dP'}{dr} = \rho\left(\omega^2 - N^2\right)\xi_r + \frac{1}{\Gamma_1 P}\frac{dp}{dr}P' - \rho\frac{d\Phi'}{dr} \tag{1.7}$$

$$\frac{1}{r^2}\frac{d}{dr}\left(r^2\frac{d\Phi'}{dr}\right) = 4\pi G\left(\frac{P'}{c_s^2} + \frac{\rho\xi_r}{g}N^2\right) + \frac{\ell(\ell+1)}{r^2}\Phi', \tag{1.8}$$

plus the equation for adiabaticity of the perturbations given above, with the buoyancy, or Brunt-Väisälä, frequency defined as

$$N^2 = g\left(\frac{1}{\Gamma_1}\frac{d\ln P}{dr} - \frac{d\ln\rho}{dr}\right), \tag{1.9}$$

the Lamb frequency defined as

$$S_\ell^2 = \ell(\ell+1)\frac{c_s^2}{r^2}, \tag{1.10}$$

and the rest of the variables as defined in Table 1.1.

To select the regular solution at the center, the solutions are matched to a second-order series expansion as $r \rightarrow 0$. At the surface of the stellar model (i.e., the photosphere), I employ a vanishing Lagrangian pressure perturbation and the vacuum potential as the outer boundary conditions (though other choices, like matching to atmospheric eigenfunctions,

can be made). The `ADIPLS` package employs either shooting or relaxation algorithms to solve for the oscillation eigenfunctions and frequencies (Christensen-Dalsgaard 2008b).

These equations permit two primary types of oscillations, those with buoyancy as their restoring force and those with pressure gradients as their restoring force. The former are typically known as gravity-modes or g-modes and the latter as pressure-modes or p-modes (e.g., Unno et al. 1989).

Local Approximation

To gain some intuition about the types of modes, we examine the oscillation equations in the local (WKB) approximation, where the radial wavelength of the perturbations is much shorter than the local radius, i.e., $k_r r \gg 1$. To examine the behavior of oscillations in this approximation, we begin by ignoring the derivatives of the equilibrium variables, which vary on the stellar length scale, in comparison with those of the perturbations, which vary across the much shorter wavelength. From this analysis, we find a second order equation for the radial displacement ξ_r:

$$\frac{d^2\xi_r}{dr^2} = \frac{\omega^2}{c_s^2}\left(\frac{N^2}{\omega^2} - 1\right)\left(\frac{S_\ell^2}{\omega^2} - 1\right)\xi_r, \tag{1.11}$$

which has the solution $\xi_r \propto e^{i\int k_r dr}$, with

$$k_r^2 = \frac{\omega^2}{c_s^2}\left(\frac{N^2}{\omega^2} - 1\right)\left(\frac{S_\ell^2}{\omega^2} - 1\right) \tag{1.12}$$

This representation captures a key quality of linear non-radial oscillations: each eigenmode may only propagate where its frequency is less than or greater than both the local values of two characteristic frequencies in the star: the Brunt-Väisälä (N) and Lamb (S_ℓ) frequencies. As the Brunt-Väisälä frequency describes buoyancy oscillations, where $N^2 > 0$, a slowly displaced parcel of fluid (low-frequency perturbation) feels a restoring buoyant force; where $N^2 < 0$, the displaced parcel feels a buoyant acceleration in the direction of motion, giving rise to the dynamically unstable oscillation known as convection (e.g., Böhm-Vitense 1958; Kippenhahn & Weigert 1990). The Lamb frequency is the minimum frequency of sound waves of a given spherical harmonic degree, ℓ, and is given by eqn. 1.10. Where the mode frequency is intermediate between N and S_ℓ, the oscillation is locally evanescent, and decays either exponentially or as a power law.

Figure 1.1 shows the run of Brunt-Väisälä and Lamb frequencies in a $30\,M_\odot$, solar metallicity star on the Zero-Age Main Sequence (ZAMS), in what is known as a propagation diagram. Interior to $\sim 16\,M_\odot$, the star is convective and the Brunt-Väisälä frequency is negative (marked "convective core" in the figure). Exterior to that point, dipole ($\ell = 1$) low frequency modes ($\omega^2 \lesssim 10^{-7}\,s^{-2}$) may propagate in the blue shaded region as g-modes, but will be evanescent in the convective core. High-frequency dipole modes ($\omega^2 \gtrsim 10^{-6}\,s^{-2}$) may propagate as p-modes in the green shaded region, with higher frequency p-modes

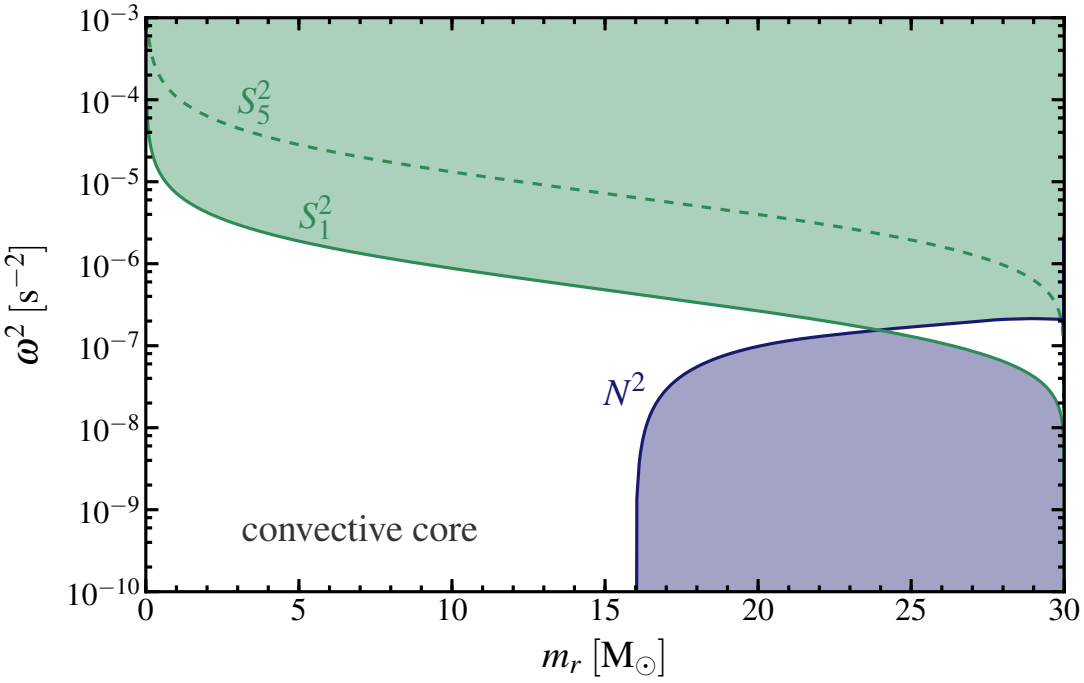

Figure 1.1: Propagation diagram for a $30\,\mathrm{M}_\odot$, solar metallicity star at the ZAMS, which shows the run of the Brunt-Väisälä and Lamb frequencies (for $\ell = 1, 5$) in the stellar interior. Interior to $\sim 16\,\mathrm{M}_\odot$ the Brunt-Väisälä frequency is negative, indicating the presence of a convective core. Exterior to that point, in the shaded blue region, g-modes of degree $\ell = 1$ may propagate. P-modes of the same ℓ are allowed to propagate in the shaded green region bounded on the bottom by the local maximum of the Brunt-Väisälä and S_1^2 frequencies. For intermediate frequencies (at a given position), shown in white, modes are locally evanescent. Propagation diagrams like this will appear throughout this work to guide understanding of where modes of different character are allowed to propagate.

capable of penetrating further in towards the core. For higher ℓ modes, the inner turning point for p-modes, where the mode frequency is approximately equal to the appropriate Lamb frequency, moves out in the star for fixed mode frequency. In the later phases of evolution, there can be multiple convective regions and a much more significant overlap in the Brunt-Väisälä and Lamb frequencies, such that waves of a given frequency can have mixed character, acting as g-modes in some parts of the star and p-modes in others (see e.g., Chapter 4).

1.3.2 The quasi-adiabatic assumption

I calculate the perturbative driving and damping rates for the adiabatic modes following the formalism of Unno et al. (1989). I approximate the imaginary component of the mode frequency (driving or damping rate) from the second-order expression for the entropy perturbation

$$\delta\omega \equiv \Im(\omega) = \frac{1}{2}\frac{\int_0^{M_{ad}} \frac{\delta T}{T}^* \delta\left(\epsilon_{\rm net} - \frac{1}{\rho}\nabla\cdot\vec{F}\right) dm}{\omega^2 \int_0^{M_{ad}} |\delta r|^2 \, dm} \tag{1.13}$$

The above represents the integration of the change in entropy due to the perturbation (mode) over one oscillation period, $2\pi/\omega$, and over the adiabatic mass, M_{ad}, of the star, defined as where

$$\frac{t_{\rm therm}}{\tau_{\rm mode}} \equiv \frac{\int_m^M c_V \, T \, dm}{\tau_{\rm mode}} \gtrsim 1 \tag{1.14}$$

(cf., Noels 1998). In this formalism, positive (negative) imaginary values represent mode driving (damping).

I further separate the integral in the numerator into work integrals, as in Unno et al.

(1989), such that

$$\delta\omega = \frac{1}{2}\frac{W_{\rm nuc} + W_\nu + W_{\rm rad} + W_{\rm grav} - \dot{E}_{\rm conv}}{E_{mode}} \tag{1.15}$$

$$E_{mode} = \omega^2 \int_0^{M_{ad}} |\delta r|^2 \, dm \tag{1.16}$$

$$W_{\rm nuc} = \int_0^{M_{ad}} \frac{\delta T^*}{T} \, \delta\epsilon_{\rm nuc} \, dm \tag{1.17}$$

$$W_\nu = -\int_0^{M_{ad}} \frac{\delta T^*}{T} \, \delta\epsilon_\nu \, dm \tag{1.18}$$

$$W_{\rm rad} = \int_0^{M_{ad}} \frac{\delta T^*}{T} \, \delta\left(-\frac{1}{\rho}\nabla\cdot\vec{F}_{\rm rad}\right) dm \tag{1.19}$$

$$W_{\rm grav} = \int_0^{M_{ad}} (\Gamma_1 - 1)(\Gamma_3 - 1)\left|\frac{\delta\rho}{\rho}\right|^2 \epsilon_g \, dm \tag{1.20}$$

$$\epsilon_g = -\left(\epsilon_{\rm nuc} + \epsilon_\nu - \frac{1}{\rho}\nabla\cdot F\right) \tag{1.21}$$

where eqn. 1.20 follows from Aizenman & Cox (1975). Below I provide more details on the meanings of each of these work integrals.

Nuclear driving

Oscillation modes with large amplitudes near regions of nuclear burning in the stellar interior can couple to this energy generation for mode driving, a process called the ϵ-mechanism (e.g., Unno et al. 1989). Over one pulsation cycle, ignoring other effects, a mode will experience a net gain in energy due to the excess energy generated during the phase of positive temperature perturbation, due to the strong, positive temperature dependence of most nuclear processes, $(d\ln\epsilon/d\ln T)_\rho \sim 4 - 40$.

Taking equation 1.17, and plugging in for the Lagrangian perturbation to the nuclear energy generation, $\delta\epsilon_{\rm nuc}$, I find

$$W_{\rm nuc} = \int_0^{M_{ad}} \left|\frac{\delta T}{T}\right|^2 \left(\frac{\epsilon_{\rho,i}}{\Gamma_3 - 1} + \epsilon_{T,i}\right)\epsilon_i \, dm, \tag{1.22}$$

where the sum over consecutive indices, i, represents a sum over the nuclear reactions taking place. I have also used the fact that the Lagrangian perturbations are adiabatic to eliminate the density perturbation in favor of the temperature perturbation.

As pointed out by Unno et al. (1989) the values of $\epsilon_{T,\rho}$ are in general, frequency dependent. When the timescales associated with the individual reactions are sufficiently short or long compared to the mode period, simple approximations can be made to give appropriate, modified $\epsilon_{T,\rho}$ values (as in the treatment of the p-p chain in Unno et al. 1989).

However, when the timescales are comparable, one must account for phase shifts between the thermodynamic and abundance perturbations (cf., Kawaler 1988; Sonoi & Shibahashi 2012). In our investigation of massive main sequence stars in Chapter 2, we include these phase shifts for mode driving by the CNO-cycle.

Neutrino damping

Modes with large amplitudes in regions with high enough densities and temperatures for neutrino losses will experience a damping due to neutrino losses, which is analogous but opposite in sign to the nuclear driving discussed above. Except during silicon burning, neutrino losses are primarily due to pair-production-annihilation, which has $\epsilon_T \approx 9$ (Clayton 1984; Woosley et al. 2002). As neutrino losses are energetically unimportant on the main sequence, this does not affect the stability calculations in Chapters 2 and 3. However, neutrino losses are the dominant source of damping considered for gravity modes in the cores of massive stars nearing core collapse, which is the focus of Chapter 4.

Radiative damping

Equation 1.19 can be rewritten as

$$\begin{aligned} W_{\rm rad} = &- \int_0^{R_{ad}} \frac{\delta T^\star}{T} \frac{d(\delta \mathrm{L}_{\rm rad})}{dr} dr \\ &+ \int_0^{R_{ad}} \frac{\delta T}{T} \Lambda^2 L_r \, \frac{T'/T}{d\ln T / d\ln r} \\ &+ \int_0^{R} \frac{\delta T}{T} \Lambda^2 \, \xi_h \frac{dL_r}{dr} \frac{dr}{r}. \end{aligned} \tag{1.23}$$

Focusing on the first term (dominant) in this expression, damping occurs whenever the temperature perturbation and radial derivative of the luminosity perturbation are of the same sign. That is to say, if, at the temperature maximum, there is more perturbed luminosity leaving the top of the layer than entering the bottom, there is radiative damping.

The luminosity perturbation itself can be written as

$$\begin{aligned} \frac{\delta \mathrm{L}_{\rm rad}}{\mathrm{L}_{\rm rad}} = \, & 4\frac{\xi_r}{r} + 4\frac{\delta T}{T} - \frac{\delta \kappa}{\kappa} - \frac{1}{\nabla_\star}\left(1 - \frac{d\ln \nabla_{ad}}{d\ln p}\right)\frac{\delta T}{T} \\ & + \frac{\nabla_{ad} - \nabla_\star}{\nabla_\star}\left(\frac{\Lambda^2 \xi_h}{r}\right) + \frac{\nabla_{ad}}{\nabla_\star}\left[\left(\frac{4\pi r^3 \rho}{m_r} - \frac{\omega^2}{\omega_\star^2}\frac{x^3}{q} - 4\right)\frac{\xi_r}{r} + \frac{1}{g}\frac{d\Phi'}{dr}\right]. \end{aligned} \tag{1.24}$$

For oscillation modes with significant amplitude in the stellar core, radiative diffusion generally leads to modest damping of modes. Radiative damping becomes increasingly important as mode energy shifts into the stellar envelope, where the local thermal time is shorter. At low enough effective temperatures and high enough metallicities, the opacity

perturbation term ($\delta\kappa/\kappa$) can provide strong driving by blocking flux at compression (maximum positive temperature perturbation) such that $d(\delta L_R)/dr$ changes sign (e.g., Cox 1980). This is known as the κ-mechanism.

Convective damping

The characteristic convective damping timescale for stars with convective cores is $\sim (M_\star R_\star^2/L_\star)^{1/3}$ (e.g., Zahn 1989). For massive stars, this is ~ 4 orders of magnitude shorter than the thermal time, which is the characteristic growth time of perturbations due to the ϵ-mechanism (κ-driving can give rise to much more rapid growth). This highlights the importance of including convective damping in calculations of the pulsational stability of massive stars (as I have done in Chapter 2). The subtlety is that the effective convective viscosity is significantly suppressed relative to the above estimate because of the mismatch between the convective turnover time and the mode periods of interest (Goldreich & Nicholson 1977; Zahn 1989).

Recent simulations by Penev et al. (2009a) have shown that, in agreement with the analytic work of Goldreich & Nicholson (1977) and Zahn (1989), interaction between pulsations and convective eddies indeed acts like a viscosity, damping oscillatory modes in convection zones. This damping is particularly important for the investigation presented in Chapter 2; I leave a detailed description to §2.3.2.

1.3.3 Stochastic wave excitation

While convection acts to viscously damp oscillations with significant amplitude *within* convection zones, as described above, it also stochastically excites both p- and g-modes (Goldreich & Kumar 1990). Convective excitation of p-modes is responsible for the solar 5-minute oscillations (see Christensen-Dalsgaard 2002, for a recent review) and analogous oscillations observed in other stellar types (Bedding 2011). Excitation of g-modes in the stably-stratified regions adjacent to convection zones is much more efficient than that of p-modes, as both convective and g-mode perturbations are roughly incompressible (Goldreich & Kumar 1990); we focus on the excitation of g-modes here as it is relevant to each of Chapters 2, 3, and 4.

The power spectrum of g-modes excited by stellar convection at and above the characteristic convective turnover frequency, $\omega_c \sim v_{\rm conv}/\mathcal{L}$, has been calculated using both heuristic physical arguments (setting the wave pressure in the stable layer equal to the convective ram pressure; Press 1981; Garcia Lopez & Spruit 1991) and by solving the inhomogeneous wave equation with convective source terms (Press 1981; Goldreich & Kumar 1990; Kumar et al. 1999; Belkacem et al. 2009a). Recently, Lecoanet & Quataert (2013) reviewed these approaches and extended them to more realistic radiative-convective boundaries; I summarize here the key results that will be used in later chapters.

Lecoanet & Quataert (2013) showed that the total luminosity in convectively excited, propagating g-modes in an adjacent radiative zone can be as large as $\mathcal{M}_{\rm conv}^{5/8}{\rm L}_{\rm conv}$. This energy

is distributed across a range of frequency and length scales determined by the properties of the convection, but resides predominantly in modes with $\omega \gtrsim \omega_c$, and $k_h \gtrsim \mathcal{L}^{-1}$. These results depend on the details of the turbulence in the convection zone and overshoot region and the structure of the buoyancy frequency at the convective-radiative transition. Using this result, we will show in Chapter 3 that the convective cores of main sequence massive stars may excite g-modes with observable surface amplitudes and in Chapter 4 that convection during the final stages of stellar evolution excites gravity waves that can lead to dramatic mass loss events.

1.4 Summary of chapters

In Chapter 2: "The Stability of Massive Main Sequence Stars as a Function of Metallicity" (originally published as Shiode, Quataert, & Arras 2012), I present an investigation of the stability of massive main sequnce stars. This work looks primarily at the stability of radial oscillations in massive main sequence stars with $M_\star \gtrsim 120\,\mathrm{M}_\odot$ across a range of metallicities from primordial (Population III) to solar. This investigation follows up on earlier work by (Baraffe et al. 2001) (and to a lesser degree Sonoi & Umeda 2011), which concluded that Population III stars on the main sequence are unstable due to nuclear-burning driving (the ϵ-mechanism) of their radial fundamental mode. Motivated by recent numerical simulations of the interaction between convection and periodic shear flows by Penev & Sasselov and collaborators (2009a; 2009b; 2011), I included a formulation of convective damping ignored in all prior work. I found that this added viscous damping serves to stabilize stars with metallicities $Z \lesssim 2 \times 10^{-3}$, which would otherwise appear to be unstable due to the ϵ-mechanism. This suggests that low-metallicity massive main sequence stars, which lack the necessary metals for line-driven winds (see §1.1), are unlikely to experience significant mass loss on the main sequence. However, our calculations are sensitive to the form of the convective viscosity, highlighting the need for further work simulating the convection-pulsation interaction at high resolution. For more metal-rich stars, with $Z \gtrsim 2 \times 10^{-3}$, I confirm previous calculations and find strong instability due to the driving effect of opacity variations (the κ-mechanism). In these stars, there are enough metals in the stellar envelope to produce an appreciable enhancement to the opacity in the "iron-bump" at $\log T \sim 5.2$ (Rogers & Iglesias 1992). This changes both the envelope and oscillation mode structure, resulting in strong κ-mechanism driving that is many orders of magnitude stronger than the ϵ-mechanism driving.

Chapter 3 is entitled "Convectively Excited Gravity Modes in Main Sequence Stars" (originally published as Shiode, Quataert, Cantiello, & Bildsten 2013). Motivated by the high precision photometric monitoring campaigns *Kepler* and *CoRoT*, I investigated whether gravity-mode oscillations excited by convection in the cores of massive stars could produce an observable signature at the stellar surface. While there is a long history of observing convectively-excited pressure modes (known as "solar-like oscillations"), and recent detections of potentially convectively-excited mixed modes, the direct excitation of

gravity modes by convection remains poorly constrained. Using a simple formalism for the excitation, recently updated by Lecoanet & Quataert (2013), I predicted the flux and surface velocity perturbations produced by convectively excited gravity modes (g-modes) in main sequence stars. I found the convective cores in stars $\gtrsim 2\,M_\odot$ can excite g-modes to sufficient amplitudes to be detectable with high precision photometry if the thickness of the convective overshoot region is $\lesssim 30$ per cent of a pressure scale height. The energy flux into convectively excited waves is steep, decaying toward high frequencies, but the change in surface amplitude and damping with frequency largely compensates for this, leading to a relatively flat surface amplitude spectrum. Thus, the incoherent sum of many g-modes would likely produce the appearance of excess photometric variability, with amplitudes of $\sim$ 10 micromagnitudes at frequencies $\lesssim 10\,\mu$Hz ($0.8\,d^{-1}$) near the solar metallicity zero-age main sequence. Overshoot shifts the characteristic excitation frequency higher, since this frequency is given by the convective velocity over the length scale of the convection at the edge of the core where the excitation predominantly occurs. I found that this surface manifestation of convectively-excited g-modes should increase with main sequence evolution, as the mode damping decreases and ever lower frequency modes are able to reach the surface. Near the terminal-age main sequence (exhaustion of hydrogen in the core) the flux perturbations may reach up to $\sim$ 100 micromagnitudes. Our convective excitation model corroborates past predictions that g-modes in the Sun, which are excited by envelope convection rather than core, have surface velocity amplitudes $\lesssim 0.3\,\text{mm s}^{-1}$. All together, our work implies that massive main sequence stars likely provide the best site for detecting the direct excitation of g-modes by stellar convection.

Chapter 4 is entitled "Setting the Stage for Interacting Supernovae I: Theory of Wave-Driven Mass Loss," which was originally published as Quataert & Shiode 2012. Here I introduce a mechanism that may provide a natural explanation for the eruptions observed and inferred to occur during the $\sim$ year leading up to core collapse supernovae. During the final stages of stellar evolution, by which I mean carbon fusion and beyond, the fusion luminosity in the cores of massive stars is many orders of magnitude larger than the emergent luminosity of the star, since neutrinos provide the dominant cooling. This large fusion luminosity drives vigorous convection in the stellar core, which carries $\sim 10\%$ of the nuclear luminosity, requiring mach numbers approaching 0.03. This convection efficiently excites internal gravity waves in adjacent, stably-stratified regions of the core; the energy flux in these waves can itself be much larger than the Eddington luminosity in the stellar envelope. In some progenitors, this wave energy is capable of reaching the stellar envelope and depositing $\lesssim 3 \times 10^{48}\,\text{erg}$, enough to unbind a significant fraction of the envelope in an energetic eruption. In this Chapter, we use one example of a 40 $M_\odot$, low metallicity star burning oxygen convectively in the core to demonstrate how these energetic, convectively excited waves could lead to mass-loss during the final phases of massive star evolution. This mechanism, which we term "wave-driven mass loss," provides a natural explanation for the seeming preponderance of giant eruptions just prior to core-collapse, which have been directly observed and inferred from the circumstellar interaction seen in some core-collapse

SNe (see §1.1).

In the final Chapter, entitled "Setting the Stage for Interacting Supernovae II: Wave-Driven Mass Loss in Supernova Progenitors," I investigate the probability of wave-driven mass loss for a grid of SN progenitor models. For this work, we use `MESA star` to construct a grid of 1-D stellar evolution models for stars ranging in mass from 12 – 100 $M_\odot$, metallicity from 0 to Solar, initial rotation from 0 to 0.8 critical, and two different mass loss prescriptions. For each progenitor, we address whether the waves convectively excited in the core are capable of tunneling out to the envelope at any point during the evolution to core collapse. None of the progenitors excite sufficiently luminous waves to drive mass loss during core carbon fusion. During core neon and oxygen fusion, most progenitors that retain their hydrogen envelopes and become giants excite a super-Eddington flux in waves that is likely to tunnel to the envelope, carrying $10^{46} - 10^{48}$ erg. This is sufficient to produce circumstellar environments with $\sim 10^{-3} - 1\,M_\odot$ out to $\lesssim 300$ AU. However, only a subset of the progenitors have waves capable of driving an outflow prior to core collapse, primarily because the timescale to heat up and inflate the stellar envelope can be longer than the time to core collapse in many cases. In addition, in the most compact progenitors, the energy-bearing convectively excited waves during O and Ne fusion have frequencies below the envelope's acoustic cutoff frequency and are thus prohibited from tunneling. At silicon fusion, during the final days of a star's life, waves in almost all progenitors are capable of transporting $\sim 10^{47}$ erg of energy from the core to the stellar envelope. However, due to the short remaining time before explosion, this energy likely cannot do more than inflate the envelope. In most compact progenitors, this may inflate up to $\sim 0.5\,M_\odot$ from $\sim 0.5\,R_\odot$ to $\sim 10\text{s} - 100\text{s}\,R_\odot$. Due to the strong, inverse correlation between burning timescale and helium core mass, the timescale of a pre-SN outburst can be used to place an upper limit on the core mass of the associated progenitor.

Chapter 2

The Stability of Massive Main Sequence Stars as a Function of Metallicity

An earlier version of this chapter was previously published as Shiode, J. H., Quataert, E., & Arras, P. 2012, MNRAS, 423, 3397.

Abstract

We investigate the pulsational stability of massive ($M \gtrsim 120$ M$_\odot$) main sequence stars of a range of metallicities, including primordial, Population III stars. We include a formulation of convective damping motivated by numerical simulations of the interaction between convection and periodic shear flows. We find that convective viscosity is likely strong enough to stabilize radial pulsations whenever nuclear-burning (the ϵ-mechanism) is the dominant source of driving. This suggests that massive main sequence stars with $Z \lesssim 2 \times 10^{-3}$ are pulsationally stable and are unlikely to experience pulsation-driven mass loss on the main sequence. These conclusions are, however, sensitive to the form of the convective viscosity and highlight the need for further high-resolution simulations of the convection-oscillation interaction. For more metal-rich stars ($Z \gtrsim 2 \times 10^{-3}$), the dominant pulsational driving arises due to the κ-mechanism arising from the iron-bump in opacity and is strong enough to overcome convective damping. Our results highlight that even for oscillations with periods a few orders of magnitude shorter than the outer convective turnover time, the "frozen-in" approximation for the convection-oscillation interaction is inappropriate, and convective damping should be taken into account when assessing mode stability.

2.1 Introduction

Several rounds of investigations over the course of the last seventy years have shown that massive main sequence stars above a critical mass near 100 $M_\odot$ are vibrationally unstable in their fundamental radial mode (e.g. Ledoux 1941; Schwarzschild & Härm 1959; Simon & Stothers 1970; Ziebarth 1970). In these stars, the low density contrast between the stellar core and envelope allows the fundamental mode to reach large amplitude near the core, where it may readily couple to the highly temperature sensitive nuclear energy generation (the ϵ-mechanism). This results in linear instability with growth times shorter than the stellar evolutionary time. The resulting non-linear evolution of this instability, which several authors proposed could lead to significant pulsation-driven mass loss, remains an unsolved problem despite considerable effort (e.g. Appenzeller 1970; Ziebarth 1970; Papaloizou 1973).

The introduction of OPAL opacities in stellar models in the early nineties (Rogers & Iglesias 1992) enhanced the linear instability of massive stars of approximately solar metallicity. Glatzel et al. (1993; 1999) found that the enhanced opacity in the stellar envelope due to transitions in heavy element isotopes can produce strong radiative (κ-mechanism) and strange-mode driving. Today, these mechanisms are generally believed to be the most important sources of fundamental mode instability in massive solar-metallicity stars (Glatzel 2005).

In the investigations to date, convection has been treated in the "frozen-in" approximation, in which the interaction between pulsation and convection is ignored entirely. The validity of this approximation is unclear and needs to be explicitly quantified. The treatment of convection-pulsation interaction as an enhanced viscosity has a long history rooted in studies of tidal Q factors and the solar 5-minute oscillations (e.g. Goldreich & Nicholson 1977; Zahn 1989). Only recently, however, have these theoretical estimates been calibrated with numerical experiments. In particular, Penev et al. (2009b; 2011) have shown that for oscillation timescales of the same order as the outer convective turnover time, the interaction is well represented by an anisotropic viscosity which scales linearly with the ratio of the oscillation and outer convective turnover times (as argued for by Zahn 1989). On timescales shorter than about one-third of the outer turnover time, these authors argue for a quadratic scaling in accordance with Goldreich & Nicholson (1977).

In this paper we reconsider the linear stability of radial oscillations in massive stars, including primordial Population III stars. For primordial stars, the lack of metals excludes opacity-driven instabilities in the envelope (i.e., κ-mechanism and strange modes). The driving found previously for Population III stars above about 120 $M_\odot$ relies on nuclear-driving in the convective stellar core (ϵ-mechanism), with resulting growth times that are much longer than for opacity-driven modes (Baraffe et al. 2001; Sonoi & Umeda 2011). It is thus particularly important to check the effect of convective damping on these weakly-driven modes. We also extend our investigation to higher metallicities for ~ 100 $M_\odot$ models to examine the effect of convective damping on the stability of massive stars of a range of metallicities.

We begin by describing the equilibrium stellar models used in this work in §2.2. In §2.3, we describe our quasi-adiabatic linear stability analysis, highlighting the important contributions to mode driving and damping. We then describe our primary results in §2.4 and discuss their implications in §2.5.

2.2 Equilibrium Stellar Models

We have computed evolutionary sequences for equilibrium stellar models with initially primordial composition (i.e., Population III stars) using the `MESA star` stellar evolution code (Paxton et al. 2011)[1]. We have also computed model sequences for an initial mass of 120 $M_\odot$, and a range of metallicities from $Z = 2 \times 10^{-6}$ to solar (which we take to be $Z = 0.02$). All models are non-rotating and have mass loss turned off. The former approximation is made for simplicity, while the latter is justified for Population III stars because the line-driving mechanism for massive star winds relies on the presence of metal-line opacity in the stellar atmosphere (e.g., Lamers & Cassinelli 1999; Castor et al. 1975). For the higher metallicity models, since we are interested only in the stability of massive stars on the main sequence, the effects of mass loss are not critical.

We use the standard mixing length prescription of Böhm-Vitense (1958) and a mixing length of ~ 1.6 pressure scale heights for the convective mixing. To examine the effects of mixing on pulsational stability, we have tested schemes for determining the onset of convection that cover the likely range of convective core sizes for non-rotating stellar models—from Ledoux criterion to Schwarzschild criterion with convective overshoot. The qualitative conclusions of our stability analyses are insensitive to our choice of mixing parameters. Thus we present, as an illustrative example, models using the Schwarzschild criterion for convection and with convective overshoot of 10% of one pressure scale height above the convective core (with overshoot calculated using the prescription of Herwig 2000).

We follow the evolution of Population III stars with masses between 120 and 1000 $M_\odot$ through their main sequence (core hydrogen burning) evolution, using the parameters outlined above and a nuclear reaction network covering all the relevant reactions for hydrogen and helium burning (see Paxton et al. 2011, for details). Figure 2.1 shows the evolution of these stellar models from the Zero-Age Main Sequence (ZAMS) to a 40% central hydrogen mass fraction (X_{ctr}). For massive Population III stars ($M_\star \gtrsim 20$ $M_\odot$), hydrogen burning by the p-p chain cannot halt the gravitational contraction; the star contracts to $T_c \sim 10^8$ K and ignites He fusion by the triple-alpha process to produce enough heavy elements to sustain hydrogen burning by the CNO cycle (Marigo et al. 2001). Thus, these stars have much higher central temperatures on the main sequence than their higher metallicity counterparts.

The highly mixed models shown in Fig. 2.1 have large convective cores and correspondingly thin radiative envelopes, which expand to form red supergiants while the core is still fusing hydrogen. This is particularly true for the most massive models, as can be seen in

[1] http://mesa.sourceforge.net/

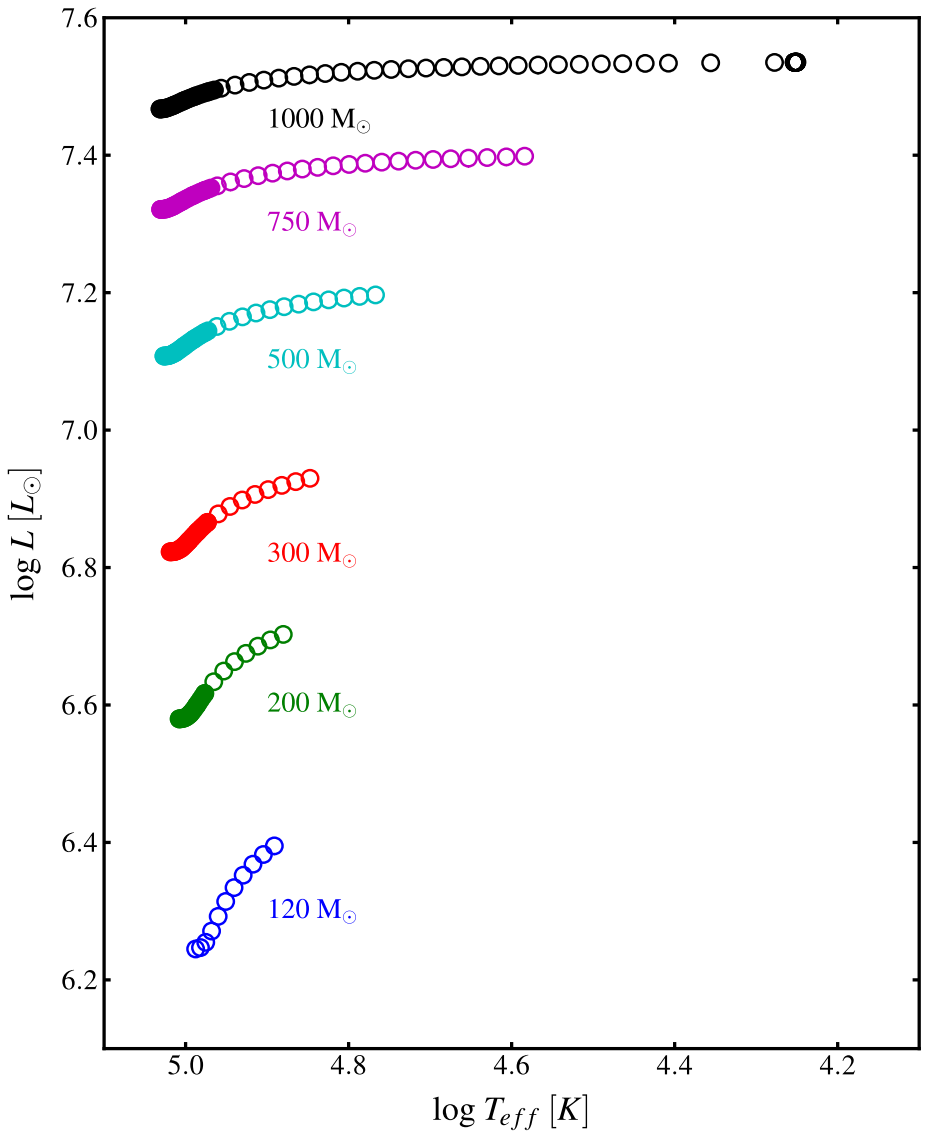

Figure 2.1: Hertzsprung-Russell Diagram for Population III Stars with masses between 120 and 1000 $M_\odot$ and initially primordial abundances. For each mass, the evolution is run with Schwarzschild mixing and 10% convective overshoot, no rotation, and zero mass loss. Each sequence shown runs from the ZAMS to a center hydrogen composition (X_{ctr}) of 40% by mass. Filled symbols indicate models with unstable radial pulsations when convective damping is ignored, while open symbols denote stable models.

Fig. 2.1.[2]

2.3 Pulsational Analysis

For each model in the sequences shown in Fig. 2.1 (and the analogous higher metallicity models), we have calculated a set of quasi-adiabatic oscillation modes as described in §1.3. Below I highlight details of the driving and damping discussed in §1.3.2 that are particularly relevant for pulsations in the massive main sequence stars under consideration in this chapter.

2.3.1 Nuclear Driving

For the high central temperatures reached in Population III stars ($\log T_c \gtrsim 8.1$), the fundamental mode period is intermediate between the proton capture and beta-decay timescales in the CNO cycle. Accounting for the phases of the abundance variations, I find a slight reduction of ϵ_T by $\sim 15\%$ from the equilibrium value determined by the temperature dependence of the $^{14}\mathrm{N}(p,\,\gamma)^{15}\mathrm{O}$ reaction. Thus I have $\epsilon_T \lesssim 8$ near the centers of massive Population III stars, somewhat smaller than the value used in Baraffe et al.'s (2001) earlier study.

2.3.2 Convective Damping

The viscous effect of convection acting to damp stellar oscillations was outlined in § 1.3.2. Here, I provide more details relevant to the study presented in this chapter.

Penev et al. (2009a) have shown through simulations that convective eddies act to viscously damp pulsations, in agreement with the analytic work of Goldreich & Nicholson (1977) and Zahn (1989). In particular, Penev et al. (2009a) find that, over the range of frequencies and spatial scales accessible in their simulations, the effective kinematic viscosity of the convection scales linearly with the ratio of the oscillation period and turnover time of the largest eddies. We refer to the latter as $\tau_{\mathcal{L}}$ below.

However, their simulations do not allow resolution of eddies with turnover times smaller than about $0.3\,\tau_{\mathcal{L}}$. That they see *no measurable viscous damping* for forcing periods less than this resolution limit implies that eddies with turnover times less than or equal to the forcing timescale dominate the viscous interaction when $t_{\mathrm{force}} \lesssim 0.3\,\tau_{\mathcal{L}}$. Thus, these authors

[2]Evolving the most massive models to a lower central hydrogen mass fraction becomes difficult because the envelope expands significantly and evolves on a timescale much shorter than the nuclear timescale. For the less mixed models we have run (those without overshoot or using the Ledoux criterion for convection), the radiative envelopes are larger for a given mass, and they do not expand to form red supergiants while still burning hydrogen in their cores. Our qualitative results regarding the stability of main sequence massive stars are insensitive to our choice of mixing parameters. However, exactly when (and if) the star evolves significantly away from its ZAMS state does depend on the details of mixing.

argue that the formalism of Goldreich & Nicholson (1977), derived on the assumption that near-resonant eddies in a Kolmogorov cascade dominate the viscosity, applies for higher frequency (shorter period) forcing.

We thus take a conservative approach, in terms of minimizing the effect of viscous damping, and assume that the change to quadratic scaling occurs *just beyond the resolution of their simulations,* at a ratio of $t_{\rm force}/\tau_{\mathcal{L}} \equiv \Pi_{\rm min} = 0.1$. Generalizing the results of Penev & Sasselov (2011), we define our fiducial, frequency-dependent kinematic viscosity to be

$$\nu\left(\omega, r\right) = \left(\frac{1}{3} v_L L\right) \min\left[\frac{1}{\Pi_{\rm min}}\left|\frac{2\pi}{\omega\tau_{\mathcal{L}}}\right|^2, \left|\frac{2\pi}{\omega\tau_{\mathcal{L}}}\right|, \Pi_{\rm max}\right]. \tag{2.1}$$

Here r is the radius of the layer, $L = \min(r, H)$ is the mixing length, v_L is the convective velocity according to mixing length theory, $\tau_{\mathcal{L}}$ is the convective turnover time of the largest eddies (which we take to be $1/N_{\rm Brunt-Väisälä}$), ω is the mode's angular frequency (and $2\pi/\omega \equiv t_{\rm force}$), and the dimensionless factor $\Pi_{\rm max} = 2.4$ represents the timescale ratio above which the viscosity is independent of forcing period (saturation period). As can be seen, the quadratic reduction applies for $(2\pi/\omega\tau_{\mathcal{L}}) < \Pi_{\rm min}$, linear reduction for $\Pi_{\rm min} \leq (2\pi/\omega\tau_{\mathcal{L}}) \leq \Pi_{\rm max}$, and unreduced for $(2\pi/\omega\tau_{\mathcal{L}}) > \Pi_{\rm max}$

Figure 2.2 shows a comparison of $\tau_{\mathcal{L}}$ and the fundamental mode period for several main sequence models. The left panel shows Population III models, while the right shows higher metallicity, 120 $M_\odot$ models. For Population III models, the fundamental mode periods are always well into the quadratic scaling regime, but for the higher metallicity cases, the mode periods tend to lie in the linear scaling or unreduced regimes, especially for the convective zones in the envelope of the star ($\log T \lesssim 6$).

For a *radial mode* within the star, the integrated rate of convective damping is given by

$$\dot{E}_{\rm conv} = \int \nu\, s_0' \left(\frac{\partial v_r}{\partial r}\right)^2 dm. \tag{2.2}$$

Plugging in the expansion in terms of modes, we find

$$\dot{E}_{\rm conv} = \int \nu\, s_0'\, \omega^2\, |k_r|^2\, \xi_r^2\, dm, \tag{2.3}$$

where s_0' is the coefficient for damping due to the radial component of the shear from Penev & Sasselov (2011, their eqn. 9), and k_r is given by the usual adiabatic oscillation equations. In accordance with eqn. 1.13, we then divide by the mode energy to calculate the integrated damping rate due to interaction with the convection.

For the modes in Population III stars described below, $(2\pi/\omega\tau_{\mathcal{L}}) < \Pi_{\rm min}$ (see eqn. 2.1). If the turnover to quadratic scaling actually occurs at mode periods shorter (longer) than what we have taken here, the damping will be stronger (weaker) than what we calculate. However, given the limiting value of $\Pi_{\rm min} \lesssim 0.3$ found by Penev et al. (2009a), we find it unlikely that the damping is weaker than calculated here (see §2.4 and 2.5 for further discussion).

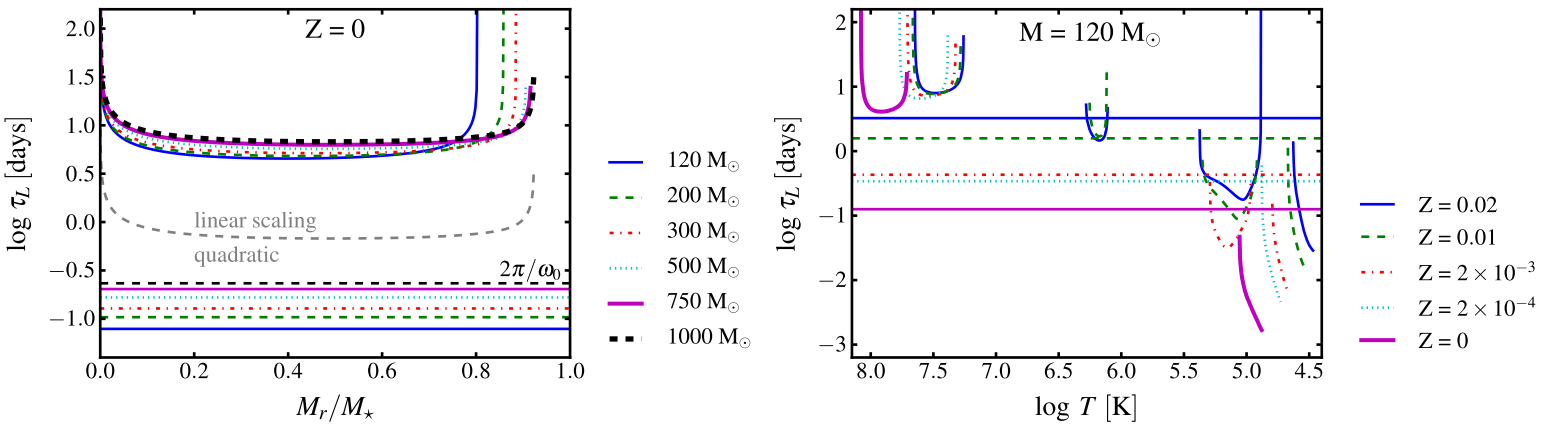

Figure 2.2: Convective turnover time, $\tau_{\mathcal{L}}$, plotted against fractional mass enclosed for a Population III main sequence model with masses from $120 - 10^3$ M$_\odot$ (left panel), and against internal temperature for 120 M$_\odot$ models for a range of metallicities (right panel). For the Population III stars, the models shown have $X_{ctr} \approx 0.7$; the variable metallicity stars have $X_{ctr} \approx 0.4$. The straight horizontal lines in each panel show the fundamental mode periods corresponding to each model plotted. For reference, the boundary between linear and quadratic scaling of the convective viscosity with mode period for the 1000M$_\odot$ Population III model is shown as the thick dashed grey line in the left panel. For all other models (in both panels) this transition occurs at a period one order of magnitude less than the convective turnover time of the stellar model.

2.4 Results

2.4.1 Zero Metallicity

Figure 2.3 shows the results of our quasi-adiabatic stability analysis for the fundamental radial modes in Population III main sequence models. The top panel shows the driving/-damping rates using the "frozen-in" approximation for convection, while the bottom panel includes the effects of convective damping. In the absence of convective damping, massive stellar models with $M_\star > 120$ M$_\odot$ have unstable fundamental modes until the central hydrogen mass fraction is $\lesssim 0.6$. The bottom panel of Fig. 2.3 demonstrates, however, that convective damping stabilizes the fundamental mode in all Population III main sequence models, regardless of mass and age. We find that this is true unless $\Pi_{\rm min}$ (which characterizes the transition from linear to quadratic suppression of convective damping) satisfies $\Pi_{\rm min} \gtrsim 0.25$. While this possibility is not completely ruled out by Penev et al.'s calibration of convective damping, we regard it as exceptionally fine-tuned.

When we ignore the effects of convective damping (top panel), our results are comparable to those of Baraffe et al. (2001, their fig. 4) to within factor of 2. The moderate disagreement likely stems from differences in the parameters used to evolve the stellar models and the $\sim 15\%$ difference in the temperature dependence of the CNO cycle between their work and ours (see §1.3.2). In particular, the reduction in temperature sensitivity leads us to conclude that the fundamental mode in 120 M$_\odot$ Population III main sequence models is stabilized by radiative diffusion in the envelope even before convective viscosity is taken into account.

While our calculations are quasi-adiabatic and theirs are non-adiabatic, this difference is likely unimportant for the modes and models shown in Fig. 2.3, which Baraffe et al. found to be unstable to the ϵ-mechanism (stars having $X_{ctr} \gtrsim 0.5$). First, the non-adiabatic region of the star, defined by the inverse inequality of eqn. 1.14, contains less than $\sim 10^{-4}$ of the total stellar mass for all models shown in Fig. 2.3. Second, the fraction of the mode energy found in the non-adiabatic zone is also always less than $\sim 10^{-4}$. Taken together, these justify our quasi-adiabatic assumption.

Figure 2.4 shows the mode energy distribution (top panel) and work integrals (bottom panel) for the fundamental radial mode in a main sequence ($X_{ctr} = 0.718$) 500 M$_\odot$, Population III stellar model. The dominant contributions to the total work integral come from the nuclear driving and convective damping, at $r/R \lesssim 0.4$ ($m_r \lesssim 100$ M$_\odot$). Similar plots for fundamental modes in other main sequence models are qualitatively the same. For more evolved models (those with lower X_{ctr}), the mode energy shifts outward into the stellar envelope and radiative diffusion is the dominant source of damping.

2.4.2 Dependence on Metallicity

We have performed the same analysis as for the Population III stars, for models with 120 M$_\odot$ and a range of metallicities from 10^{-6} to solar (taken to be 0.02). Figure 2.5 shows the results of these calculations. In the upper panel, the net growth rate (taking into account

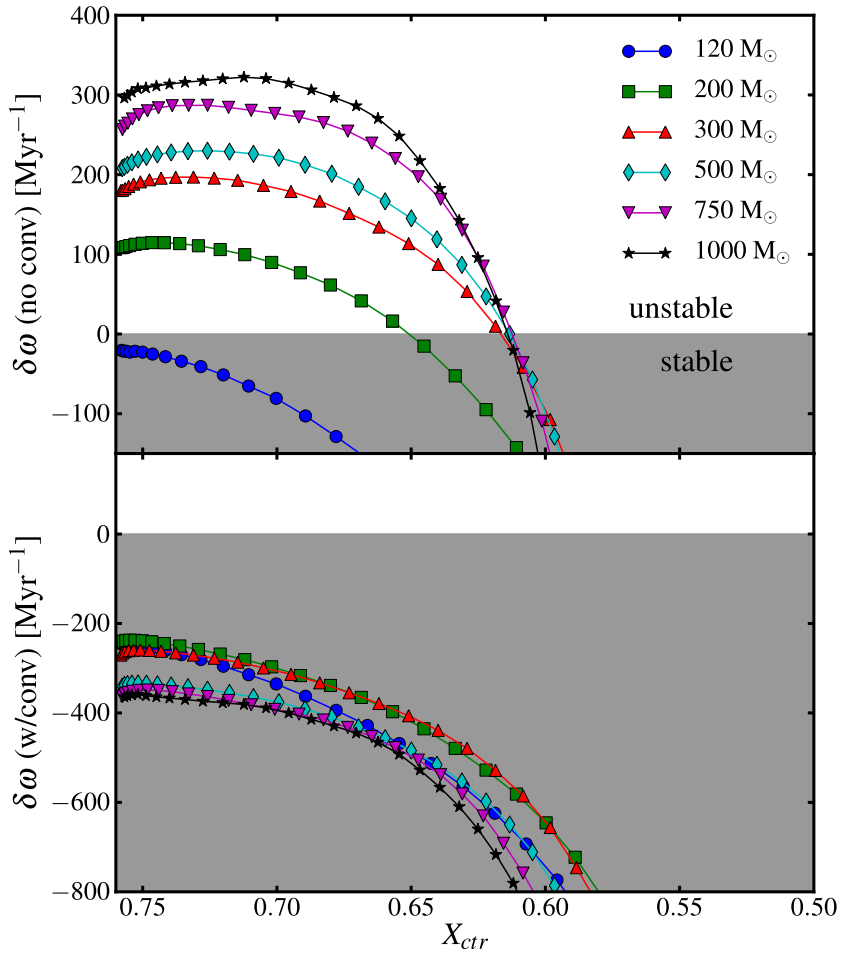

Figure 2.3: Growth rates, in units of Myr^{-1}, for the radial fundamental modes of Population III stars on the main sequence, shown versus the mass fraction of hydrogen in the star's convective core. The top panel shows the results assuming the "frozen-in" approximation for convection (for comparison with fig. 4 of Baraffe et al. 2001), while the bottom panel includes the effects of convective damping. Negative growth rates (shaded region) denote stability. Note that the 120 M$_\odot$ models are always stable in this analysis with or without convective damping, due to the lower CNO cycle temperature dependence (see §1.3.2)

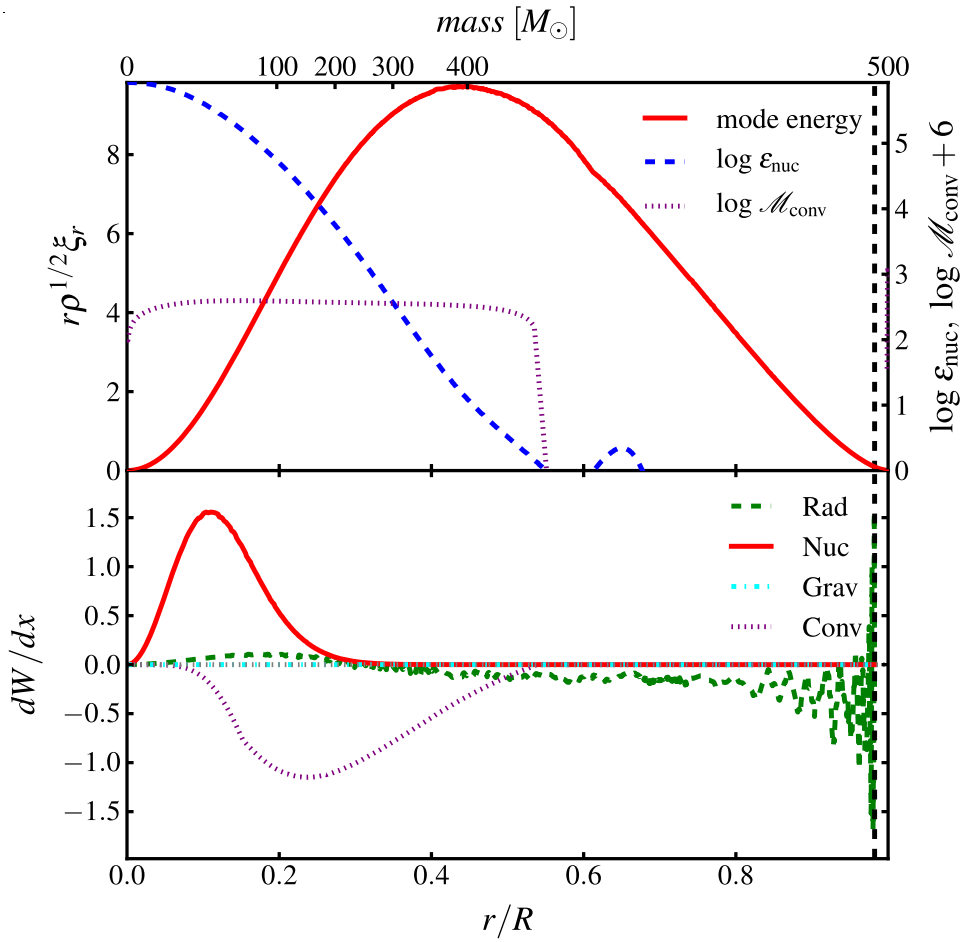

Figure 2.4: Mode energy (red solid line, top) and work integrals (bottom) for a typical, damped radial fundamental mode in a Population III, $500M_\odot$ main sequence model. All quantities are plotted versus r/R (bottom abcissa) and enclosed mass, m_r (top abcissa). The top panel also shows the nuclear energy generation rate (blue dashed, right axis) and the Mach number of the convection (purple, dotted line). The bottom panel shows the different contributions to the total work integral described in equations 1.17, 1.19, 1.20, and 2.3, with colors according to the legend.

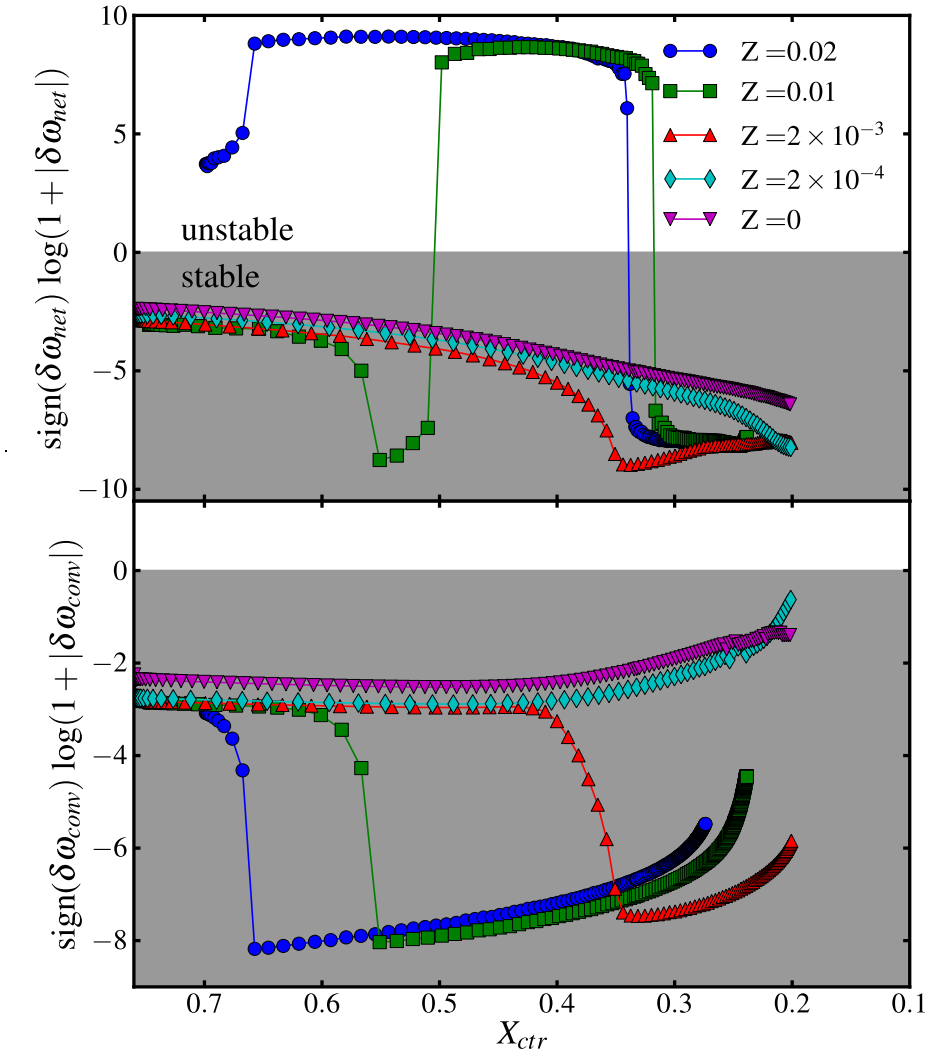

Figure 2.5: Net growth rates including convective damping (top) and the convective damping rates (bottom) for radial fundamental modes in stars on the main sequence with $M_\star = 120$ $M_\odot$ and a range of metallicities, shown versus the mass fraction of hydrogen in the star's convective core. Note the logarithmic scale of the y-axis, which highlights the large change in the magnitude of the driving/damping when the mode amplitude shifts to the envelope, as for the solar and half solar metallicity models (blue circles and green squares, respectively). The corresponding change in the magnitude of the convective damping occurs because the damping is dominated by an envelope convection zone rather than the convective core (see Fig. 2.2).

any convective damping) is shown versus the central hydrogen fraction (as in Fig. 2.3). Note the logarithmic scale for the growth and damping rates. The bottom panel shows the contribution of the convective viscosity to the damping rate. Models with $0 < Z < 2 \times 10^{-4}$ are not shown since their results are nearly identical to the $Z = 0$ models.

As shown in Fig. 2.6, the sharp transition in the net growth and convective damping rates for models with $Z \gtrsim 2 \times 10^{-3}$ is due to the shift in mode energy out into the stellar envelope (shown in the figure for models with $Z = 0.01$). This transition occurs when the low-density envelope expands due to the increased radiation pressure around the iron opacity enhancement at $\log T \approx 5.2$. When the mode energy is primarily in the stellar envelope there is the possibility for κ-mechanism driving around the iron opacity enhancement, as well as stronger convective damping in an outer convection zone where the mode and convective frequencies are comparable.

In agreement with Baraffe et al. (2001), we find that the radial fundamental modes in main sequence models with $Z \gtrsim 2 \times 10^{-3}$ are strongly driven by the κ-mechanism operating in the envelope at the location of the opacity-enhancement due (primarily) to iron transitions (Rogers & Iglesias 1992). The location of the adiabatic cutoff mass/radius, as defined by equation 1.14, relative to the location of the opacity peak at $\log T \approx 5.2$ determines when the opacity is capable of providing strong driving (cf. Cox 1980). This alignment changes with the expansion of the stellar envelope, such that only models at particular evolutionary stages on the main sequence have fundamental modes driven by the κ-mechanism.

Across the range of masses and metallicities investigated here, we find that convective viscosity always overcomes the ϵ-driving in the stellar core. However, for models with $Z \gtrsim 2 \times 10^{-3}$, the stellar and mode structures are such that κ-mechanism provides the dominant driving and is orders of magnitude stronger than the convective damping. However, this envelope driving occurs in a region where the local ratio $t_{\rm therm}/\tau_{\rm mode}$ is only slightly larger than unity and our assumption of quasi-adiabaticity is not entirely valid (as shown in Fig. 2.6). A fully-non-adiabatic method would likely provide more reliable growth-rates for these modes. Moreover, our quasi-adiabatic analysis is not capable of capturing strange-mode driving, which is also likely to be important for the same models that are unstable to the κ-mechanism (cf., Glatzel 1998).

2.4.3 Higher order and non-radial modes

In addition to the fundamental mode, we have also studied the stability of higher order radial modes and non-radial oscillations. Higher order radial modes—those having a larger number of radial nodes—have a more significant fraction of their energy outside the nuclear burning core, and have shorter wavelengths, which both lead to stabilization by radiative damping.

The presence of a large convective core prevents gravity(g)-modes from propagating to small radii and coupling to the nuclear driving (see also Sonoi & Umeda 2011). While high frequency, low angular degree pressure(p)-modes may penetrate into the burning region,

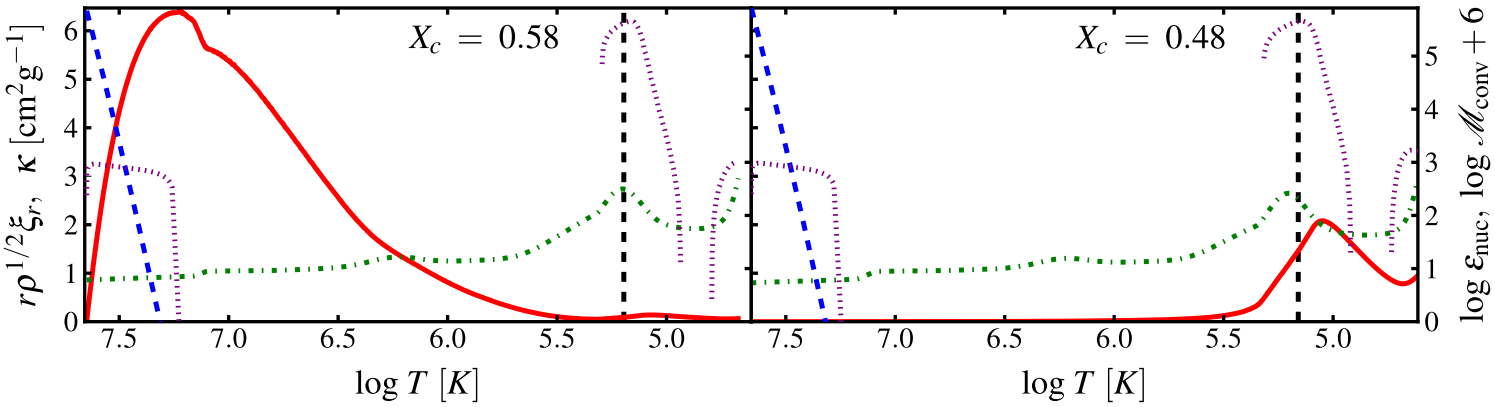

Figure 2.6: Mode energy (red) as a function of $\log T$ for $Z = 0.01$ main sequence stellar models. Shown on the left is a stable mode with $X_{ctr} \approx 0.58$, and on the right is a κ-driven mode with $X_{ctr} \approx 0.48$. Also shown are the run of opacity (green dot-dashed line, left ordinate, multiplied by 3 for clarity), convective mach number (purple dotted line, right ordinate), nuclear energy generation rate (blue dashed line, left ordinate), and adiabatic cutoff (black dashed vertical line). All values are shown versus $\log T$. In the more evolved model on the right, the low-density envelope has expanded by a factor of ~ 2 due to the enhanced radiation pressure around the iron opacity bump at $\log T \approx 5.2$.

these modes have their largest amplitudes near the stellar surface where the density is low and radiative damping dominates. Furthermore, while p- and g-modes of high enough angular degree can be trapped by the increase in N^2 at the edge of the convective core due to the chemical composition gradient, these modes experience strong radiative damping that overcomes the weak nuclear-driving they experience (cf. Unno et al. 1989).

2.5 Discussion and Conclusions

In this paper, we have studied the stability of radial and non-radial oscillation modes for massive main sequence stars of a range of metallicities, from primordial Population III stars to those of solar composition. We find that convective damping is likely to stabilize modes that would otherwise be unstable by the ϵ-mechanism (driving by nuclear fusion). This is particularly important for primordial stars whose high effective temperatures imply that there is no driving due to opacity variations in the stellar envelope (the κ-mechanism). Thus, we conclude that massive Population III stars are linearly stable on the main sequence, supporting the idea that such stars are unlikely to experience any pulsation-driven mass loss during their main sequence evolution.

The calculations in this paper build on those of Baraffe et al. (2001) and Sonoi & Umeda (2011), who found that the fundamental radial oscillations in Population III stars with $M_\star > 120$ M$_\odot$ are unstable due to the ϵ-mechanism. However, both Baraffe et al. and Sonoi & Umeda neglected convective damping. Recent hydrodynamic simulations by Penev et al. (2009a) have shown that the convective viscosity scales linearly with the oscillation period for periods of the same order as the turnover time of the largest eddies (in agreement with Zahn 1989) and quadratically for much shorter periods (in agreement with Goldreich & Nicholson 1977). The transition between these regimes is not directly accessible to the simulations; we have taken a conservative estimate of $\Pi_{\rm min} = 0.1$, in agreement with the simulations, in order to minimize the convective viscosity. If $\Pi_{\rm min} \gtrsim 0.25$, some ϵ-driven modes remain unstable, but this is an extremely fine-tuned value, given Penev et al.'s result that $\Pi_{\rm min} \lesssim 0.3$.

Even more recent simulation work by Ogilvie & Lesur (2012) calls the work of Penev et al. into question, finding that the viscosity always scales with the period ratio squared (as Goldreich & Nicholson 1977), and may in fact be negative (i.e., driving) in the short period forcing regime of interest for this work. These latter simulations use a smaller forcing amplitude than that of Penev et al., leading to relatively noisier measurements, and a smaller simulation box which may not capture the full spectrum of turbulence on the large scales within a stellar convection zone. This latter aspect may be crucial to their measurement since they infer that the negative contribution to the viscosity is dominated by the effect of the largest scale eddies. The sensitivity of our results to the exact form of the convective viscosity highlights the need for higher resolution simulations of the convection-oscillation interaction, particularly using larger simulation domains to capture the interaction with the large-scale eddies.

Stellar models with sufficiently high metallicity, $Z \gtrsim 2 \times 10^{-3}$, have strong opacity variations in their envelopes which can provide κ-mechanism driving. We find that the fundamental mode in these models are destabilized by the κ-mechanism operating near the iron-bump in opacity for much of their main sequence evolution. This driving is orders of magnitude stronger than the convective damping. These models experience large linear growth rates that approach non-adiabiticity ($\delta\omega \lesssim \omega$). For lower metallicity models, the ϵ-mechanism provides the dominant driving but is overcome by convective damping as in Population III models. In all of the massive stellar models we have considered, we find that damping due to convective viscosity is stronger than the driving by the ϵ-mechanism in stellar interiors for radial modes.

Both Baraffe et al. and Sonoi & Umeda estimate that massive Population III stars may lose a few (for $M_\star \lesssim 1000$ M$_\odot$) or up to $\sim 10\%$ (for $M_\star \gtrsim 1000$ M$_\odot$) of their total stellar mass due to pulsation-driven mass loss during the proposed unstable phase of the main sequence. As Sonoi & Umeda highlight, the convective cores of stars $\gtrsim 500$ M$_\odot$ comprise $\gtrsim 90\%$ of the stellar mass, implying that pulsation-driven mass loss may expose the convective core, perhaps further increasing mass loss by mixing nuclear-processed material to the surface to initiate a radiation-driven wind, or by increasing the duration of the proposed pulsationally unstable phase. If, instead, the pulsations are damped by convective viscosity as we have concluded, there may be no significant mass lost during the main sequence phase for massive Population III stars.

In order to fully address the mass loss properties of massive primordial stars, we must address their stability at more evolved stages. However, as stars evolve off the main sequence, their fundamental radial mode becomes increasingly non-adiabatic as the mode energy shifts to the expanding, low-density stellar envelope. Analyzing these modes requires a non-adiabatic calculation, which we leave to future work.

With all oscillatory modes in main sequence Population III stars likely stabilized by convective damping, evidence points to there being no mass loss on the main sequence for these metal-free stars, so long as the non-rotating stellar models used here are a reasonable approximation. The question of what happens as these stars evolve thus becomes all the more crucial for assessing the fates of the first stars.

Acknowledgments

We thank Gordon Ogilvie for useful discussions regarding calibration of the convective viscosity. We also thank the anonymous referees for useful comments. This work was supported by NASA Headquarters under the NASA Earth and Space Science Fellowship Program - Grant 10-Astro10F-0030.

Chapter 3

Convectively Excited Gravity Modes in Main Sequence Stars

An earlier version of this chapter was previously published as Shiode, J. H., Quataert, E., Cantiello, M., & Bildsten, L. 2013, MNRAS, 430, 1736.

Abstract

We predict the flux and surface velocity perturbations produced by convectively excited gravity modes (g-modes) in main sequence stars. Core convection in massive stars can excite g-modes to sufficient amplitudes to be detectable with high precision photometry by *Kepler* and CoRoT, if the thickness of the convective overshoot region is $\lesssim 30$ per cent of a pressure scale height. The g-modes manifest as excess photometric variability, with amplitudes of ~ 10 micromagnitudes at frequencies $\lesssim 10\,\mu$Hz ($0.8\,\mathrm{d}^{-1}$) near the solar metallicity zero-age main sequence. The flux variations are largest for stars with $M_\star \gtrsim 5$ $\mathrm{M}_\odot$, but are potentially detectable down to $M_\star \sim 2-3$ $\mathrm{M}_\odot$. During the main sequence evolution, radiative damping decreases such that ever lower frequency modes reach the stellar surface and flux perturbations reach up to ~ 100 micromagnitudes at the terminal-age main sequence. Using the same convective excitation model, we confirm previous predictions that solar g-modes produce surface velocity perturbations of $\lesssim 0.3\,\mathrm{mm\ s}^{-1}$. This implies that stochastically excited g-modes are more easily detectable in the photometry of massive main sequence stars than in the Sun.

3.1 Introduction

At the interfaces between convective and radiative zones in stellar interiors, convective motions transfer a fraction of their kinetic energy into waves in the radiative layer (e.g., Press 1981; Goldreich & Kumar 1990; Belkacem et al. 2008). Studying the details of this energy transfer is important for our understanding of mixing at convective boundaries, the evolution of shear layers and the excitation of stellar oscillations in many contexts.

The Sun provides an exquisite laboratory for studying convectively excited sound waves (p-modes), with a forest of modes observed at the solar surface (see Gizon et al. 2010; Christensen-Dalsgaard 2002, for recent reviews). These sound waves have been detected in many other stars as well, with rapid growth in the sample of observed "solar-like oscillators" in the past several years thanks to high precision monitoring campaigns like *Kepler* (Bedding 2011).

To date, gravity modes (g-modes) have not been convincingly observed at the solar surface (see Appourchaux et al. 2010, for a recent review). Gravity modes are observed in several other stellar types, including, for example, white dwarfs (Winget & Kepler 2008) and slowly-pulsating B-stars (De Cat 2007). In each of these cases, the g-modes are linearly unstable, rather than stochastically excited as in the case of solar-like oscillations. In the interesting case of the mixed gravity and pressure modes recently observed in giants (see e.g., Bedding et al. 2011; Beck et al. 2011), the convective excitation occurs in the envelope where the modes behave locally as pressure waves. Thus, the *direct* excitation of g-modes by turbulent convection is not well tested observationally.

Main sequence stars more massive than the Sun have convective cores and relatively compact, predominantly radiative envelopes, through which g-modes propagate. This structure makes them potential hosts for observable, stochastically excited g-modes. The unprecedented micromagnitude precision of photometric monitoring campaigns like *Kepler* (Koch et al. 2010) and *CoRoT* (Convection, Rotation and planetary Transits; Auvergne et al. 2009) provides exciting prospects for detecting these stochastically excited g-modes and opening a new window into both the physics of convective boundaries and massive stellar interiors. Indeed, Samadi et al. (2010) studied the convective excitation of g-modes in main sequence stars with masses of 10, 15, and 20 $M_\odot$ and central hydrogen mass fraction of 0.5, finding that convectively excited g-modes in these stars may reach amplitudes near the threshold for detectability with *CoRoT*. In the following, we present a complementary approach and investigate g-mode amplitudes in a wider range of initial stellar masses, from 2 to 30 $M_\odot$, and evolutionary states along the main sequence.

We begin by describing our model for the spectrum of g-mode excitation in §3.2, followed by our method for calculating the observable signatures of convectively excited g-modes in §3.3, 3.4, and 3.5. In §3.6, we present the results of our calculations for the surface flux and velocity perturbations of g-modes in massive main sequence stars. We conclude with a discussion of remaining uncertainties, including the effects of rotation and stellar evolution modeling, and the current and ongoing observations which might shed light on

these predictions (§3.7).

3.2 Convective excitation of gravity modes

Convection efficiently excites gravity modes in an adjacent stably stratified medium, as both convective and g-mode perturbations are roughly incompressible (Goldreich & Kumar 1990, see § 1.3.3;). The power spectrum of g-modes excited by stellar convection at and above the characteristic convective turnover frequency, ω_c, has been calculated using both heuristic physical arguments (setting the wave pressure in the stable layer equal to the convective ram pressure; Press 1981; Garcia Lopez & Spruit 1991) and by solving the inhomogeneous wave equation with convective source terms (Press 1981; Goldreich & Kumar 1990; Kumar et al. 1999; Belkacem et al. 2009a). These approaches are reviewed and extended to more realistic radiative-convective boundaries in Lecoanet & Quataert (2013); we summarize here the key results for our application.

The low frequency g-modes that carry most of the wave power are strongly damped by radiative diffusion (see §3.4). As a result only g-modes with frequencies significantly larger than the characteristic convective turnover frequency (i.e., $\omega \gg \omega_c$) can set up global standing waves potentially detectable at the stellar surface – this is true for both solar-type stars with envelope convection zones and massive stars with core convection zones. High frequency g-modes have characteristic radial wavelengths in the radiative zone that are large compared to the thickness of the radiative-convective boundary. In this limit, it is reasonable to approximate the radiative-convective boundary as a discontinuity in the Brunt-Väisälä frequency (as in Goldreich & Kumar 1990). For g-modes excited by a core convection zone (or its overshoot region), which is relatively unstratified, the excitation occurs at a roughly fixed position at the edge of the convection zone. The power spectrum of energy supplied to g-modes is then given by

$$\frac{d\dot{E}_g}{d\ln\omega\, d\ell} \sim \mathcal{M}_{\rm conv}\, \mathrm{L}_{\rm conv} \left(\frac{\omega}{\omega_c}\right)^{-a} \ell^b \left(\frac{H}{r}\right)^{b+1} \left(1+\ell\frac{H}{r}\right) \exp\left[-\left(\frac{\ell}{\ell_{\rm max}}\right)^2\right] \tag{3.1}$$

over the range

$$\omega \geq \omega_c \equiv v_{\rm conv}/H, \quad \ell \geq 1, \tag{3.2}$$

where $\ell_{\rm max} \equiv (r/H)\,(\omega/\omega_c)^{3/2}$, r and H are evaluated at the edge of the convective core (where their ratio is ~ 1), and the remaining variables are defined in Table 1.1. The power-law exponents a and b are given by $a = 13/2$ and $b = 2$.[1]

[1]Because excitation of g-modes by Reynold's stresses dominate excitation by entropy fluctuations (Goldreich & Kumar 1990), the convective luminosity in eqn. 3.1 is technically that associated with the kinetic energy, rather than enthalpy. In mixing length theory, these two contributions to the convective luminosity are comparable. For the purposes of our calculation, we thus take $\mathrm{L}_{\rm conv}$ to be the total convective luminosity in the stellar model and absorb uncertainties in the relative contribution of kinetic and enthalpy fluxes into the uncertain normalization of eqn 3.1.

Note that integrating over frequency and ℓ, equation 3.1 implies that convection excites a total g-mode luminosity of (Goldreich & Kumar 1990)

$$\dot{E}_g \sim \mathcal{M}_{\rm conv}\, \mathrm{L}_{\rm conv}. \tag{3.3}$$

In fact, the efficiency of g-mode excitation can exceed equation 3.3 depending on the nature of the convective-radiative transition (Press 1981; Lecoanet & Quataert 2013). Equation 3.1 is, however, appropriate for the high frequency g-modes of interest in this paper. In our numerical work, we choose the uncertain dimensionless constant in equation 3.1 so that the integrated wave power is exactly $\dot{E}_g = \mathcal{M}_{\rm conv}\, \mathrm{L}_{\rm conv}$.

One of the primary uncertainties in the prediction of g-mode excitation is whether the excitation occurs primarily in the bulk of the convection zone or in a thin "overshoot" region near the radiative-convective boundary. We parameterize this uncertainty by taking the local scale-height in the excitation region to be ηH, where H is the true pressure scale height near the radiative-convective boundary. This amounts to taking $H \to \eta H$ in equation 3.1 when calculating the wave excitation. The parameter η can take on values in the range $(0, 1]$, such that $\eta = 1$ corresponds to excitation dominated by eddies of size $\sim H$ in the convection zone and $\eta < 1$ to excitation dominated by a thin overshoot region hosting eddies of size $\sim \eta H$. Excitation dominated by a thin overshoot region will have a higher characteristic frequency ω_c/η since the length scale of the convective motions is reduced by η. This serves to shift the g-mode power input to higher frequency and shorter spatial scales (higher ω and ℓ). Note, in particular, that for low ℓ modes having $\omega \gg \omega_c$, $\dot{E}_g \propto H^{-7/2}$. Thus excitation in a thin overshoot layer significantly increases the power supplied to the high frequency modes that are the most observable.

In their numerical simulations of the solar radiative-convective transition, Rogers & Glatzmaier (2006) found that the power into g-modes is roughly constant for $\omega \sim 1 - 10\,\omega_c$ and then decreases significantly for $\omega \gtrsim 10\,\omega_c$ (see their figs. 1 & 2). This increase in the characteristic frequency of the excited g-modes is reasonably consistent with excitation in the overshoot layer given the width of the overshoot layer of ~ 0.05 H found in the same simulations (see Rogers et al. 2006). The smaller scales in the overshoot region would also naturally produce power at higher ℓ, as also found by Rogers & Glatzmaier (2006).[2]

Fig. 3.1 shows the logarithmic excitation spectrum for our 2 $\mathrm{M}_\odot$ model, for $\eta = 1$ (left panel) and 0.1 (right panel). This shows that most of the wave energy is in the lowest frequency modes convection can excite. In addition, since the wavelength and frequency of convective eddies are correlated, energy input at higher mode frequencies is predominantly in modes of higher ℓ.

[2]Note that the simulations of Rogers & Glatzmaier (2006) use an artificially high convective luminosity relative to the solar value. It is unclear whether this changes the functional form of the g-mode power vs. frequency; this needs to be studied in more detail.

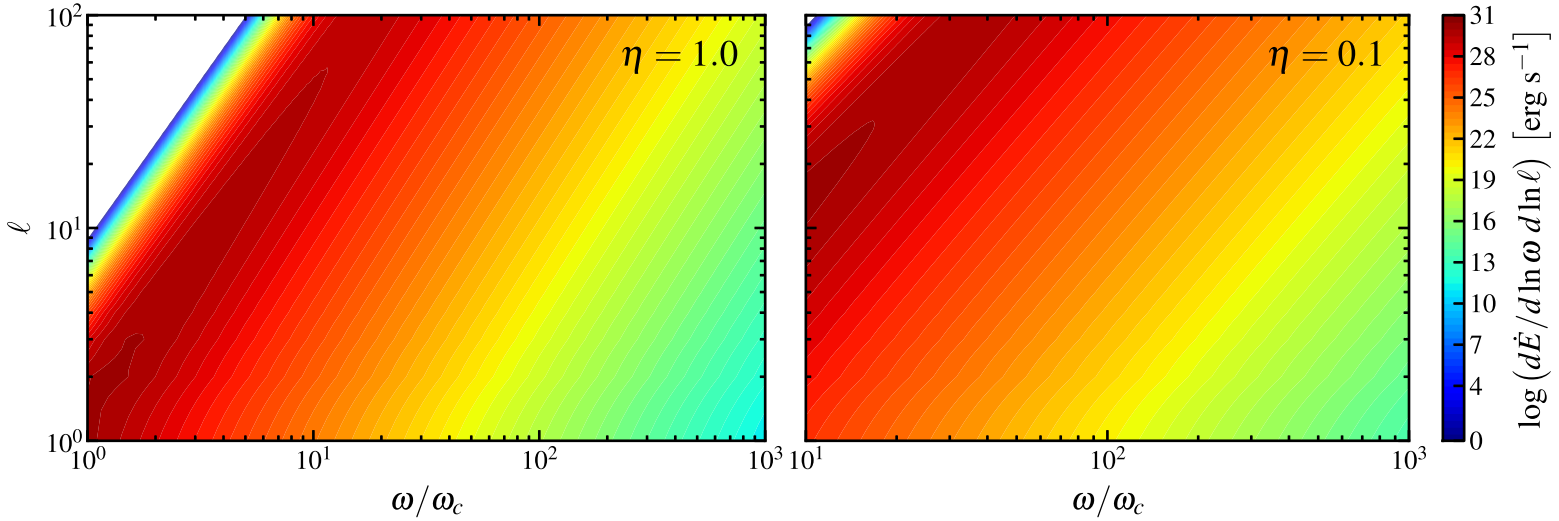

Figure 3.1: Convective excitation spectrum vs. ω/ω_c (abscissa) and ℓ (ordinate), for g-modes in our 2 $M_\odot$ model. The spectrum shown in the left panel is for excitation by the convection zone, $\eta = 1$, and the right for excitation dominated by an overshoot region having a width of 10 per cent of a pressure scale height, $\eta = 0.1$. Note the different scales on the abscissa in the two panels, since our parametrization of the power spectrum applies only above $10\,\omega_c$ for $\eta = 0.1$ (see eqn. 3.2). Also note values for $\log d\dot{E}_g/(d\ln\omega\, d\ln\ell) < 0$ are represented as white. The spectra for models with $M \gtrsim 10$ $M_\odot$ peak at higher ℓ values since $r/H \gtrsim 2$ at the edges of their convective cores; otherwise, spectra for different masses are qualitatively similar, with the overall energy injection rate scaled according to the value of $\mathcal{M}_{\rm conv}\, L_{\rm conv}$ (see Table 3.3).

3.3 Stellar models

We have constructed main sequence models from zero-age main sequence (ZAMS) to the terminal-age main sequence (TAMS), at a central hydrogen mass fraction of 0.01, for a range of initial masses from 2 to 30 $M_\odot$ using the MESA stellar evolution code (version 4298; Paxton et al. 2011)[3]. All models are non-rotating and solar metallicity (which we take to be $Z = 0.02$) with the Grevesse & Sauval (1998) chemical mixture. Following the results of Brott et al. (2011), we determine convective boundaries using the Ledoux criterion with 30 per cent of a pressure scale height of overshoot,[4] and a mixing length parameter $\alpha_{\rm MLT} = 1.5$. We also use semiconvection with a dimensionless efficiency parameter, $\alpha_{sc} = 0.1$, though this is largely irrelevant due to the overshoot. Finally, we assume the theoretical mass loss rates of Vink, de Koter, & Lamers (2001) (or de Jager et al. 1988 when $T_{\rm eff} < 10^4$ K) scaled down by a factor of 0.8.

We tested for numerical convergence by varying the number of mesh points and timesteps taken during the evolution, finding good agreement at the level of refinement used for the models presented.[5] We have also tested a range of other model parameters, including the mixing length, boundary definitions and rotation, to test their effects on our results (see §3.7.1). Fig. 3.2 shows the evolutionary tracks in the H-R diagram for the models described above from ZAMS to TAMS. Along the sequence, crosses appear every 1/10th of the main sequence lifetime, and symbols mark the locations where we have calculated the convective excitation of g-modes: ZAMS ($X_{ctr} = 0.68$), midMS ($X_{ctr} = 0.33$), and TAMS ($X_{ctr} = 0.01$).

Table 3.3 gives parameters for the convective cores of our ZAMS models, including the outer scale convective turnover frequency ($\nu_c \equiv \omega_c/(2\pi)$), the core luminosity ($L_{\rm conv}$, which is roughly equivalent to the emergent stellar luminosity) and the convective mach number ($\mathcal{M}_{\rm conv}$). Over the range of masses represented, $\mathcal{M}_{\rm conv}$ increases with luminosity (and mass), but only as $\sim {L_{\rm conv}}^{0.2}$. The yet weaker dependence of the convective turnover frequency on mass reflects the increase in convective core radius with mass, since energy-bearing eddies span roughly the core radius.

Fig. 3.3 shows propagation diagrams for our 2 and 10 $M_\odot$ ZAMS models (upper and lower panels, respectively). Each panel shows the Brunt-Väisälä frequency, N, in the radiatively stable envelope (blue, solid line), the Lamb frequency ($S_\ell^2 \equiv \ell\,(\ell+1)\,c_s^2/r^2$) for $\ell = 1, 10$ (green, solid line), and the outer convective turnover frequency in the core (red, dashed line). Note the ordinate units are linear frequency, ν. These diagrams highlight where g-modes and sound waves may propagate in the stellar interior, with g-modes propagating wherever $\omega < N, S_\ell$ and sound waves where $\omega > N, S_\ell$ (Aerts et al. 2010; Unno et al. 1989). The convective turnover frequency for all models is ~ 3 orders-of-magnitude less than the Brunt-Väisälä frequency in the radiative zone. Thus, modes with $\omega \gtrsim \omega_c$ propagate as high-order (short-wavelength) g-modes in the radiative zone. Lastly, the contrast between

[3] http://mesa.sourceforge.net/

[4] We use a step function overshoot prescription, in which the convection zone is extended a distance of 30 per cent of a pressure scale height above the Ledoux boundary, with a constant diffusion coefficient.

[5] `mesh_delta_coeff` = 0.25 and `varcontrol_target` = 10^{-4}

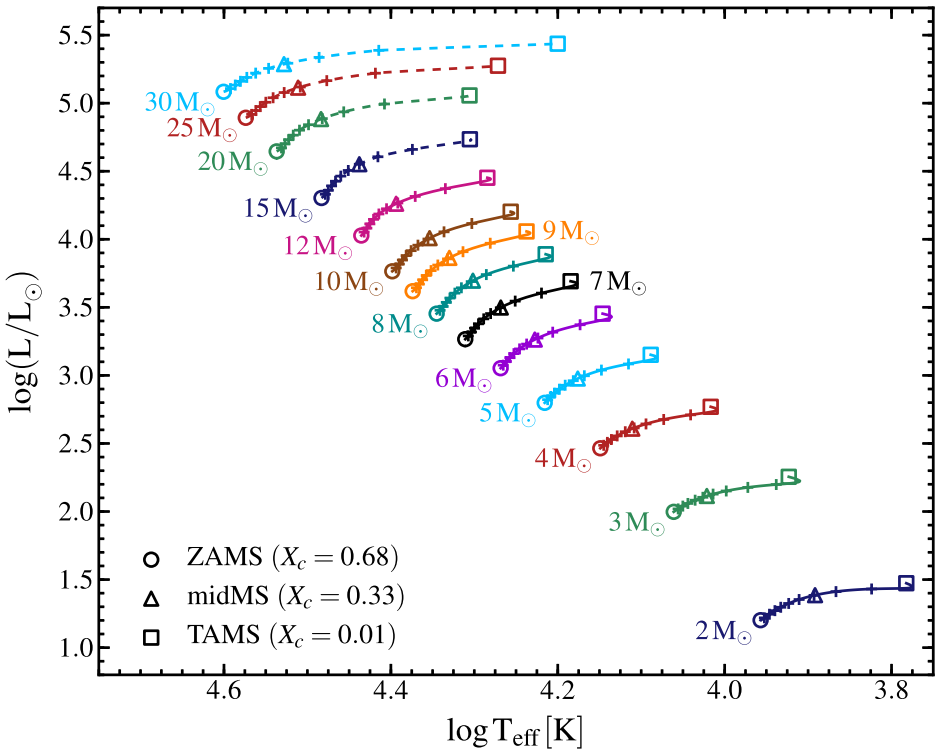

Figure 3.2: H-R Diagram showing the evolutionary tracks of our 2 to 30 $M_\odot$ model sequences spanning ZAMS to TAMS ($X_{ctr} = 0.01$). The circles, triangles and squares mark the locations of models for which we have calculated convectively excited modes, and are in the evolutionary states given in the legend. Crosses mark every 1/10th of the main sequence lifetime (i.e., the model age at TAMS).

Table 3.1: Core Convection Parameters

Mass[a]	L_{conv}[b]	$\mathcal{M}_{conv}$[c]	ν_c[d]	ν_{min} [μHz][e]	
[$M_\odot$]	[$L_\odot$]		[μHz]	ZAMS	TAMS
2	14	4.37×10^{-5}	0.05	5.81	1.58
3	75	6.67×10^{-5}	0.07	5.91	1.74
4	228	8.75×10^{-5}	0.08	5.54	1.71
5	579	1.23×10^{-4}	0.10	4.73	1.65
6	1.07×10^3	1.40×10^{-4}	0.10	4.63	1.68
7	1.79×10^3	1.57×10^{-4}	0.11	4.57	1.63
8	2.79×10^3	1.73×10^{-4}	0.11	4.12	1.59
9	4.09×10^3	1.88×10^{-4}	0.12	4.22	1.54
10	5.86×10^3	2.07×10^{-4}	0.12	4.19	1.50
12	1.03×10^4	2.32×10^{-4}	0.13	4.29	1.43
15	1.98×10^4	2.59×10^{-4}	0.14	4.43	1.31
20	4.46×10^4	3.00×10^{-4}	0.15	4.35	1.15
25	7.97×10^4	3.28×10^{-4}	0.15	4.32	0.99
30	1.23×10^5	3.46×10^{-4}	0.15	4.36	0.93

[a]Initial stellar mass

[b]Convective luminosity on ZAMS

[c]Convective mach number on ZAMS

[d]Convective turnover frequency on ZAMS

[e]Minimum frequency for $\ell = 1$ standing waves

panels shows the growth of the convective core in fractional radius (and mass) with increasing stellar mass and the structural similarity among main sequence models with core convection zones.

3.4 Gravity wave physics

To identify potentially observable g-modes in massive stars, we must first determine whether waves excited at the convective-radiative boundary reach the stellar surface. Waves excited at the boundary travel through the radiative zone, where they are subject to damping by radiative diffusion. The radiative damping rate for a traveling g-mode is given by

$$\gamma_{\rm rad}(\omega, \ell, {\rm r}) = {\rm K_{rad}(r)\, k_r^2}, \tag{3.4}$$

$$K_{\rm rad}(r) = \frac{16\,\sigma\,T(r)^3}{3\,\rho(r)^2 \kappa(r)\,c_p(r)}, \tag{3.5}$$

$$k_r \approx \frac{\Lambda}{r}\frac{N}{\omega}. \tag{3.6}$$

where $\Lambda^2 \equiv \ell\,(\ell+1)$ and k_r is the radial wavenumber. The last approximation (eqn. 3.6) relies on the WKB dispersion relation for g-modes, which have $\omega \ll N, S_\ell$.

We write a wave "optical depth" (as in Kumar & Quataert 1997)

$$\tau_w(\omega, \ell, r) = \int_{\rm r_{conv}}^{r} dr'\, \frac{\gamma_{\rm rad}(\omega, \ell, r')}{v_{\rm group}(\omega, \ell, r')}, \tag{3.7}$$

where

$$v_{\rm group} \approx \frac{\omega}{k_r} \approx \frac{\omega^2\, r'}{\Lambda\, N}. \tag{3.8}$$

Waves of a given frequency and degree deposit most of their energy at the radius where $\tau_w \sim 1$. As $\gamma_{\rm rad}$ is inversely proportional to frequency, low frequency waves damp well inside the star while high frequency waves propagate to the surface. The *minimum* frequency for standing g-modes satisfies the condition $\tau_w(\omega, \ell, r_{outer}) \lesssim 1$, where r_{outer} is the radius of the wave's outer turning point where $\omega = \min\,(N, S_\ell)$.

Fig. 3.4 shows the location where a wave of frequency ν has an optical depth, $\tau_w \sim 1$, for g-modes with $\nu \geq \nu_c$ in our 2 and 10 $\rm M_\odot$ models. The horizontal dashed lines show the minimum frequency for standing g-modes, separating the low frequency waves that damp in the radiative envelope from those that reach their outer turning point and set up standing oscillations. Also shown are the characteristic turnover frequency in the convective core (ν_c, filled circles), and the outer turning points of g-modes with $\tau_w(\omega, \ell, r_{outer}) < 1$ (filled diamonds). At high frequencies, the outer turning point moves inward with increasing frequency since it is defined by where $\omega = S_\ell$ (see Fig. 3.3).

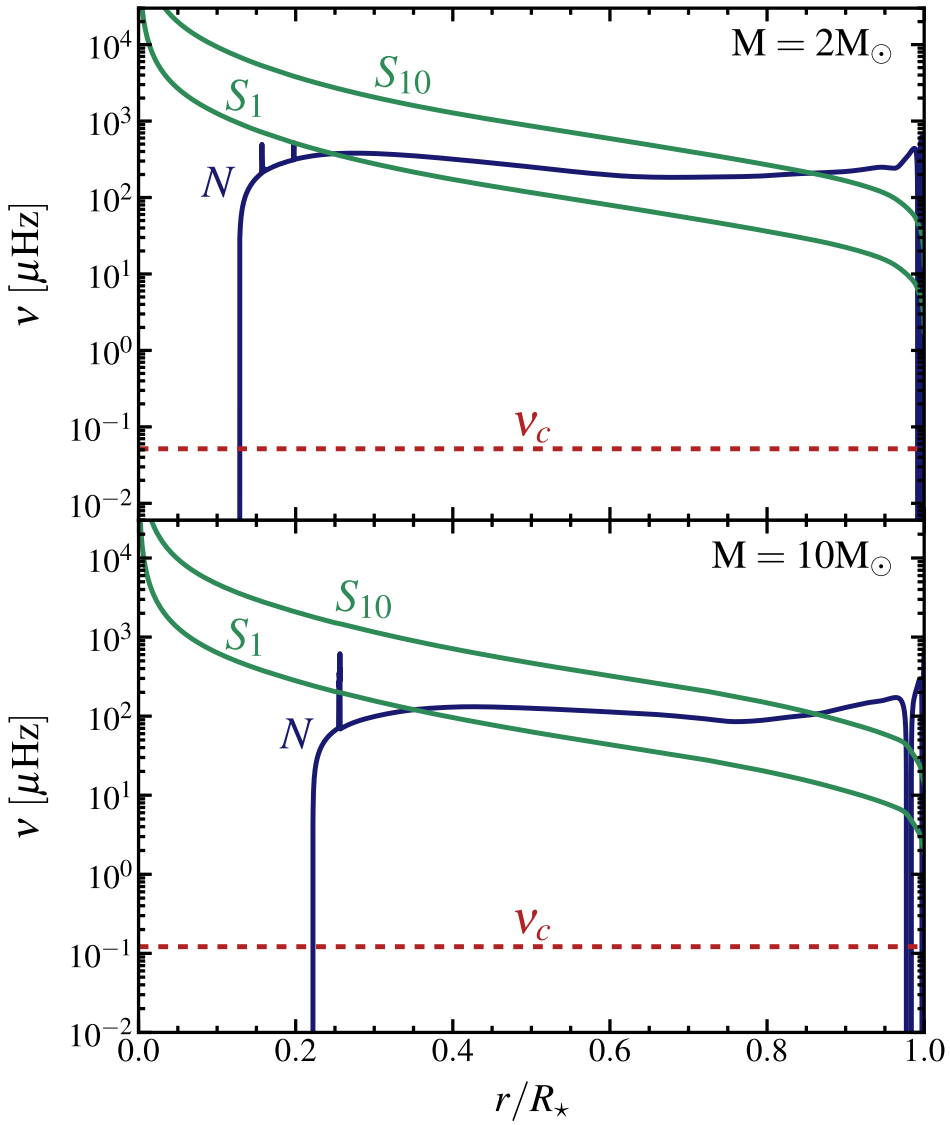

Figure 3.3: Propagation diagrams for 2 $M_\odot$ (upper panel) and 10 $M_\odot$ (lower panel) ZAMS models. The solid blue line shows the Brunt-Väisälä frequency (N), the solid green lines the $\ell = 1, 10$ Lamb frequency (S_ℓ), and the dashed red line shows the convective turnover frequency in the core (ν_c).

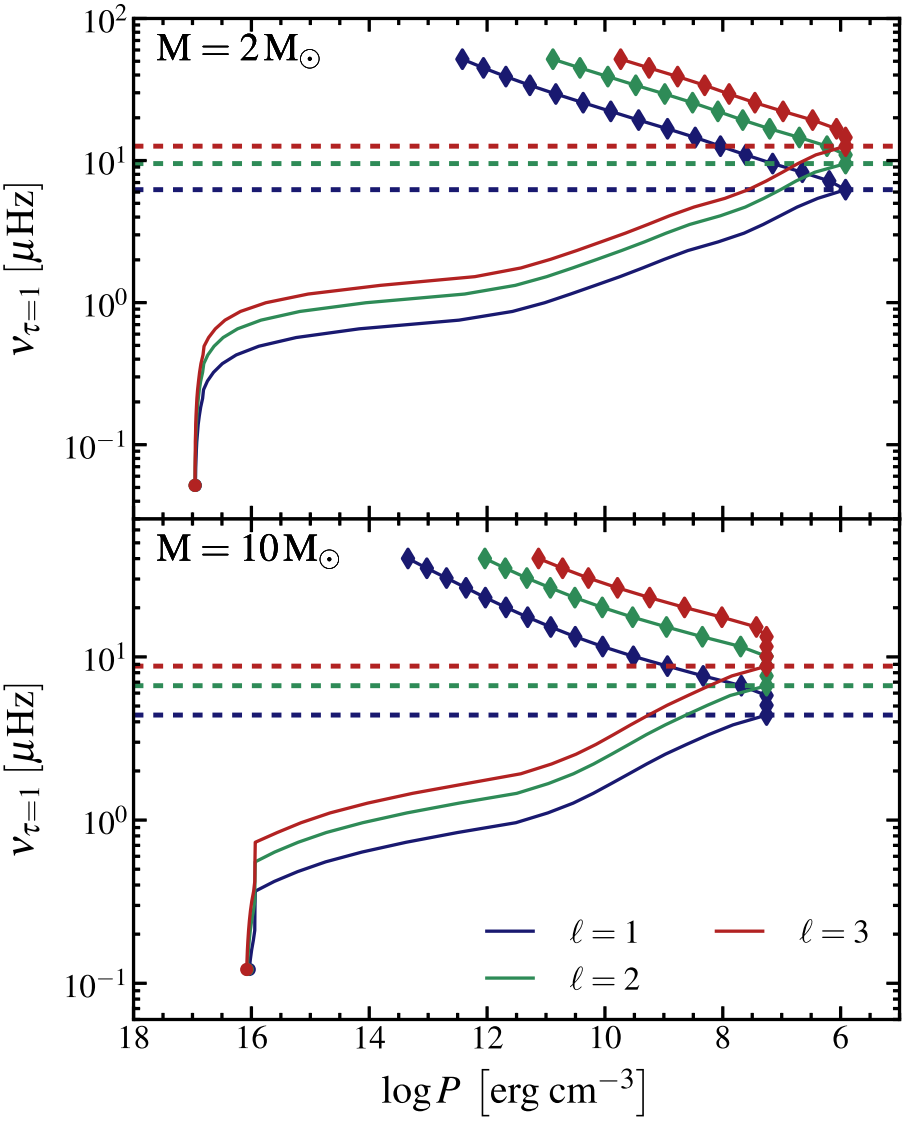

Figure 3.4: Location, in log pressure units, where an g-mode of frequency ν reaches unity optical depth due to radiative damping (see eqn. 3.7) or its outer turning point, for 2 $M_\odot$ (upper panel) and 10 $M_\odot$ (lower panel) ZAMS models. Filled circles show the characteristic convective frequency in the convective core, diamonds mark frequencies with $\tau_w < 1$ at the outer turning point (where they reflect and can set up standing waves), and the horizontal dashed lines give the minimum standing wave frequency for each ℓ. Note that the outer turning point moves inward at high frequency as it is defined by where $\omega = S_\ell$. Colors in each panel correspond to ℓ, as described in the legend in the lower panel.

3.5 Quasi-adiabatic stellar oscillations

For each model, we use prescription described in §1.3 to calculate stellar oscillation eigenfunctions and quasi-adiabatic flux perturbations and growth/damping rates for g-modes above the minimum frequency for standing waves.

Our quasi-adiabatic calculations are only valid in the regime where the thermal time of the overlying layers is greater than the mode period. Thus, we approximate surface perturbations by their value in the vicinity of the adiabatic cutoff, R_{ad}, where the thermal time in the overlying layer is equal to the mode period.[6] Comparison with non-adiabatic growth/damping rates and eigenfunctions (Townsend & Teitler *in prep*) shows that our quasi-adiabatic calculations provide a good approximation for damping rates and surface amplitudes to within factors of a few.

The short wavelength g-modes predominantly excited by convection are subject to large radiative damping. Those able to set up global standing waves are still linearly damped with lifetimes of $\sim 1 - 10^5$ yr (with the exception of some linearly driven modes). Damping rates are fit reasonably well by power laws in mode frequency, with indices of -3 to -8, where flatter power laws apply for more evolved models. Deviations from the power-law arise primarily from opacity effects in the stellar envelope, whose relative importance depends on mode frequency.

The convective excitation rate and mode lifetime together set the equilibrium mode energy

$$\mathrm{E}_{\mathrm{mode}}(\omega,\ell) = \frac{1}{2}\frac{d\dot{E}_g}{d\ln\omega\, d\ell}\mathrm{N}_{\mathrm{m}}(\omega,\ell)^{-1}\gamma^{-1}, \tag{3.9}$$

where $\mathrm{E}_{\mathrm{mode}} \equiv \omega^2/2 \int_0^{M_{ad}} [\xi_r^2 + \Lambda^2\xi_h^2]\, dm$, $\mathrm{N}_{\mathrm{m}}(\omega,\ell)$ is the number of modes in a logarithmic bin in ω (at fixed ℓ), and γ is the damping rate of the mode as determined by all non-adiabatic effects (radiative diffusion, nuclear driving, and any convective viscosity). For g-modes with $\omega \ll N$, $\mathrm{N}_{\mathrm{m}}(\omega,\ell) \approx (n + \ell/2)(2\,\ell + 1)$, where n is the number of radial nodes in the mode eigenfunction (Unno et al. 1989).

In linear adiabatic stellar oscillation theory, the amplitude of the temperature and density perturbations, and the magnitude of the fluid displacement, are arbitrary. We convert the linear theory results into realistic predictions by normalizing the g-mode eigenfunctions using the estimate of the mode energy in equation 3.9. We then use these properly normalized eigenfunctions to calculate the disk integrated perturbations as follows.

3.5.1 Surface perturbations

For modes with $\ell \geq 1$, disk-averaging effects reduce the observable amplitude of oscillations as neighboring surface elements oscillate out of phase with one another. For each

[6] In detail, we take the median value of the perturbation in the range where this ratio is between 0.1 and 10. In our 10 $\mathrm{M}_\odot$ ZAMS model, the cutoff occurs at $\log P = 8.64, 8.46, 8.18, 7.73$ erg cm^{-3} for our $n = -16, -10, -5, -1$ g-modes at frequencies of $\nu = 4.38, 6.73, 12.79, 39.85\,\mu$Hz.

mode, we calculate the disk-integrated, limb-darkened, quasi-adiabatic perturbation to the bolometric magnitude and surface radial velocity for each stellar model (as in Dziembowski 1977):

$$|\delta m| = 1.087 \left[b_\ell \frac{\delta F}{F_0} + (2b_\ell - c_\ell) \frac{\xi_r}{R} \right]_{r \approx R_{ad}}, \tag{3.10}$$

$$|\delta v_{\rm disk}| = \left[u_\ell \, \xi_r \, \omega + v_\ell \, \xi_h \, \omega \right]_{r \approx R_{ad}}, \tag{3.11}$$

where b_ℓ, c_ℓ, u_ℓ, and v_ℓ are coefficients related to the effect of limb-darkening on the visibility of modes of a given ℓ, $\xi_{r,h}$ are the radial and horizontal displacement eigenfunctions, and $\delta F/F_0$ is the fractional perturbation to the radiative flux due to the oscillation. We assume Eddington limb-darkening for simplicity, and thus use the b_ℓ, c_ℓ, u_ℓ, and v_ℓ coefficients tabulated in Dziembowski (1977).

We primarily use $\delta v_{\rm disk}$ to compare our calculations with previous estimates and observational constraints on solar g-modes (see §3.6.3). For the more massive stellar models, which we show produce a much smaller velocity signal, we also consider a simpler estimate of the non-disk-averaged total velocity perturbation

$$|\delta v_{\rm tot}| = \frac{1}{2} \left[|\xi_r \omega|^2 + |\xi_h \omega|^2 \right]^{1/2}_{r \approx R_{ad}}, \tag{3.12}$$

which might be connected to the non-thermal velocities needed to fit spectral line profiles in hot, massive stars: microturbulence and macroturbulence.

As a general rule, the procedure described above results in a ratio of flux-to-velocity-perturbations of order $\delta m / \delta v_{\rm disk} \sim 1 \, \mu{\rm mag}/\,{\rm cm\ s^{-1}}$ for $\ell = 1$ modes. We find that this ratio varies between $0.1 - 10 \, \mu{\rm mag}/\,{\rm cm\ s^{-1}}$, with a trend towards larger values at lower frequencies. There is no clear trend with mass or stellar evolutionary state.

3.6 Results

3.6.1 Brightness perturbations

We find that, unless the excitation is dominated by an overshoot region $\lesssim 10$ per cent of a pressure scale height thick, corresponding to a peak excitation frequency of $\gtrsim 10 \, \omega_c$, individual oscillation modes excited by convection produce brightness fluctuations of $\delta m \lesssim 10 \, \mu$mag (except at the TAMS, see §3.6.1).

We thus focus on the effect of an ensemble of stochastically excited modes on the intrinsic variability of the star. This RMS magnitude perturbation is an incoherent sum over all modes in a given logarithmic bin in frequency:

$$\delta m_{\rm rms} = \left[\sum_{\Delta \ln \omega, \text{ all } \ell} \sum_{m=-\ell}^{\ell} \left[\delta m(\ell, m, \omega) \right]^2 \right]^{1/2}, \tag{3.13}$$

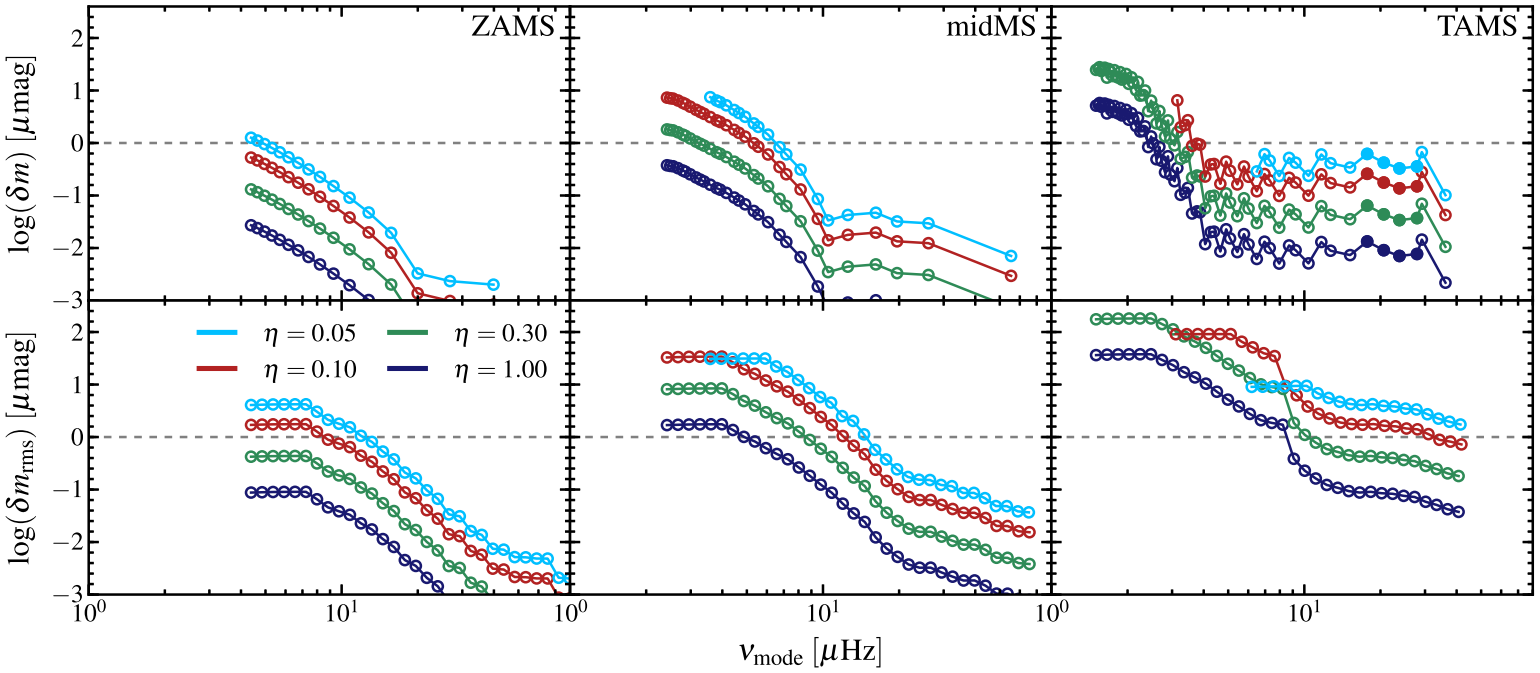

Figure 3.5: Individual $\ell = 1$ g-mode (top panels) and RMS (lower panels; see eqn. 3.13) surface brightness fluctuations as a function of frequency for convectively excited g-modes in our 10 $M_\odot$ model at the ZAMS (left panels), midMS (middle panels), and TAMS (right panels). Individual $\ell = 2$ modes have similar amplitudes to those shown in the top panels for all phases, and $\ell = 3$ modes approach parity at the TAMS. Open circles in the top panels mark individual mode frequencies, while in the bottom panels they show frequencies at which we have calculated $\delta m_{\rm rms}$. Note the decrease in the minimum standing wave frequency (i.e., the low frequency cutoff of the spectrum), and corresponding increase in the magnitude of the maximum brightness perturbation, with evolution. In our evolved models, the low frequency cutoff of the spectrum for $\eta \lesssim 0.3$ is set by the minimum excitation frequency for which our model is valid, ν_c/η, since this is larger than the minimum frequency for standing waves. There is likely to be convectively excited power at these frequencies (see, e.g., Rogers & Glatzmaier 2006), but it is not accounted for here.

where the sum is over a logarithmic bin in ω and all ℓ (though practically only $\ell \lesssim 5$ contribute).

The left panels of Fig. 3.5 show the predicted δm perturbations due to individual $\ell = 1$ modes (top) and the total $\delta m_{\rm rms}$ (bottom) as a function of frequency for our 10 $M_\odot$ ZAMS models. The open circles in the upper left panel (for δm) correspond to individual g-mode frequencies, while the circles in the bottom left panel are frequencies where $\delta m_{\rm rms}$ has been calculated from the individual modes. The flatter spectrum of the RMS magnitude perturbations, relative to that of the individual $\ell = 1$ g-modes, results from summing the contributions from all modes in a given logarithmic frequency bin, including those of higher ℓ (which are not plotted in the upper left panel; see equation 3.13).

For ZAMS models, the combination of the convective excitation spectrum and that of radiative damping combine to produce a nearly flat spectrum of mode energies for the standing g-modes excited by convection, since $\dot{E} \propto \nu^{-13/2}$ and $\gamma \propto \nu^{-6}$. However, there is a strong decrease in surface amplitude with increasing frequency at fixed mode energy, which is well fit by $\delta m \propto \nu^{-4}$, due primarily to the outer turning point moving inward. This latter trend dominates the δm spectra shown in the top panels of Fig. 3.5. The spectra of flux perturbations is qualitatively similar to that shown in Fig. 3.5 for the range of stellar masses we investigated.

The top panel of Fig. 3.6 shows the maximum $\delta m_{\rm rms}$ in ZAMS models at each mass, with color corresponding to overshoot thickness and symbol size denoting the frequency of the peak flux perturbation. In more massive stars, the closer match between standing g-mode frequencies and the characteristic excitation frequency, and the overall larger luminosity and mach number, lead to larger brightness perturbations. However, the frequency of peak brightness, $\approx 5\,\mu$Hz ($\sim 0.4\,{\rm d}^{-1}$), is roughly constant with increasing mass.

Effect of stellar evolution

Both the mach number in the core and the stellar luminosity increase during main sequence sequence evolution, leading to increased power input to g-modes and a larger characteristic convective frequency, ν_c. In addition, the minimum frequency for standing waves decreases along the main sequence as the thermal time at the mode outer turning point increases. Together these imply an increase in g-mode surface amplitudes with evolution, as well as the appearance of ever lower frequency modes.

The top and bottom panels of Fig. 3.5 show the evolution along the main sequence of the power spectrum for individual modes and $\delta m_{\rm rms}$, respectively, in our 10 $M_\odot$ model. The RMS flux perturbation (lower panels) *at fixed frequency* increases with evolution, and the appearance of lower frequency modes at the surface leads to larger signals at lower frequencies than appeared on the ZAMS.

The chemical composition gradient left behind by the receding convective core during the main sequence evolution produces an extended bump in the Brunt-Väisälä profile; this results in enhanced trapping behavior near the end of the main sequence as modes separate

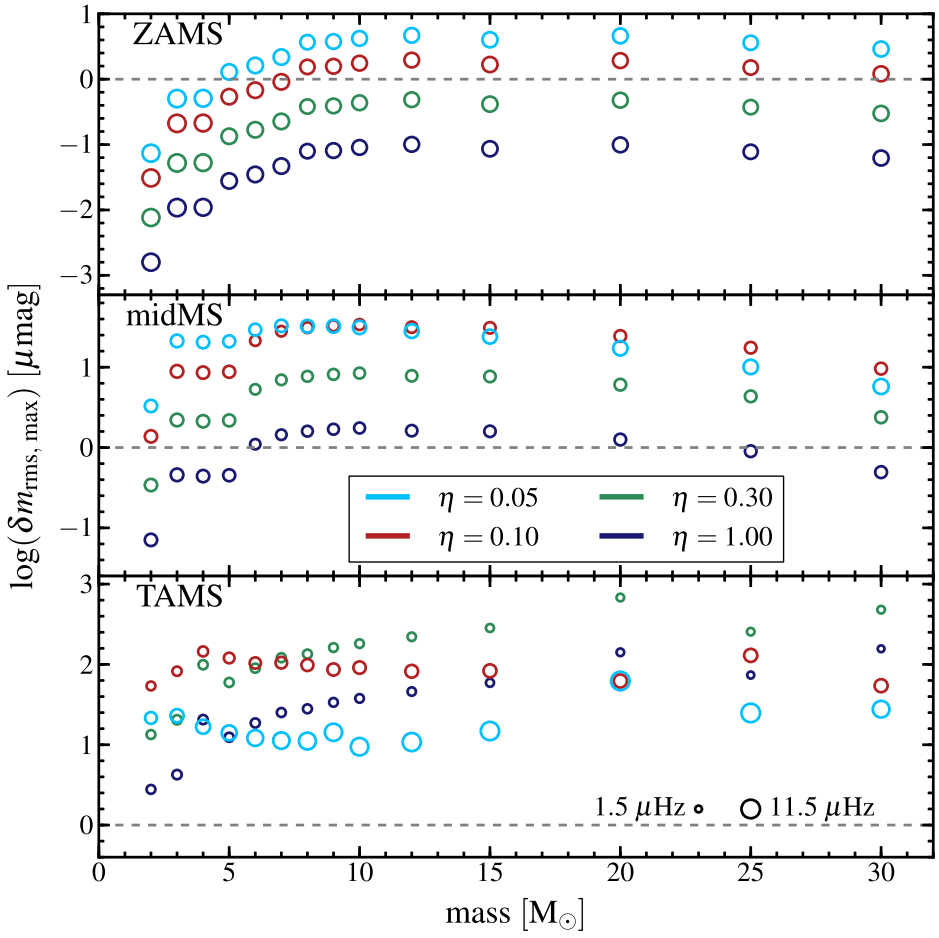

Figure 3.6: Peak RMS surface brightness fluctuations $\delta m_{\rm rms}$ for convectively excited g-modes, calculated according to eqn. 3.13, as a function of mass. Color corresponds to the value of η and size to mode frequency, as described in legend. Panels show results for models at their labeled evolutionary states. In the evolved models, the minimum frequency for excitation at small η (ν_c/η) is larger than the minimum frequency for standing waves ($\nu_{\rm min}$; Table 1), leading to a suppression in the total flux perturbation for the smallest values of η.

into those with most of their energy in that composition-gradient region and those primarily in the radiative zone. This effect leads to the differences in the surface amplitudes of adjacent modes seen in the upper right panel of Fig. 3.5.

As shown in Figs. 3.5 and 3.6, we predict g-mode power peaked at near $5\,\mu$Hz on the ZAMS, but this peak approaches $\sim 1\,\mu$Hz at the end of the main sequence. However, in our evolved models, the minimum frequency for standing g-modes can be less than the minimum frequency for which our excitation model applies, ω_c/η, when the overshoot region is $\lesssim 30$ per cent of a pressure scale height. This is shown clearly in the low-frequency cutoff of the spectra in Fig. 3.5, and in the lower panels of Fig. 3.6, where the magnitude of the maximum perturbation for $\eta = 0.05, 0.1$ is smaller than that for larger η and appears at a higher frequency. There is likely convective excitation power at these low frequencies, but it is not accounted for in our model (see, e.g., Rogers & Glatzmaier 2006).

If we assume the energy flux into modes below ν_c/η is constant, as appears to be the case in the Rogers & Glatzmaier (2006) simulations, the equilibrium energy in modes below this cutoff scales as $\sim \nu^4$. However, a strong scaling of surface amplitude at fixed mode energy, as we find in the case of our 10 $M_\odot$ TAMS model, can lead to an increase in the maximum $\delta m_{\rm rms}$ by a factor of a few and a shift of the peak to slightly lower frequencies than appear in the lower panels of Figs. 3.5 and 3.6. At yet lower frequencies, however, approaching the minimum for standing waves, ν_{min}, the predicted flux perturbations decrease.

For *Kepler* and *CoRoT* observations with micromagnitude precision photometry, *the RMS brightness fluctuations contributed by convectively excited g-modes should be detectable during the main sequence for all stars considered*, if the driving is dominated by a convective overshoot region with width $\lesssim 30$ per cent of a pressure scale height at the top of the core. The expected amplitudes reach ~ 100s of μmag around $\nu \sim 1 - 10\,\mu$Hz $(0.08 - 0.8\,{\rm d}^{-1})$.

3.6.2 Velocity perturbations

In addition to brightness perturbations, non-radial modes produce velocity perturbations which may be observed either in the disk-integrated radial velocity signature or via the motions they generate where spectral lines are formed ("microturbulence"; e.g., Cantiello et al. 2009, and references therein). In massive main sequence stars, we are interested in the latter case; moreover, we are concerned with the aggregate effect of many modes, as discussed above for the brightness perturbations.

In Fig. 3.7, we show the maximum predicted RMS velocity fluctuations as a function of initial stellar mass and evolutionary phase. For g-modes excited by the convective core, we predict surface velocity fluctuations that are always $\ll 1\,{\rm km\ s^{-1}}$, whereas the observed non-thermal surface velocities in massive main sequence stars are $\gtrsim 1 - 10\,{\rm km\ s^{-1}}$. Even in our most optimistic scenario for excitation, with $\eta = 0.05$, g-modes excited by core convection do not produce sufficiently large velocities to explain the observed microturbulence.

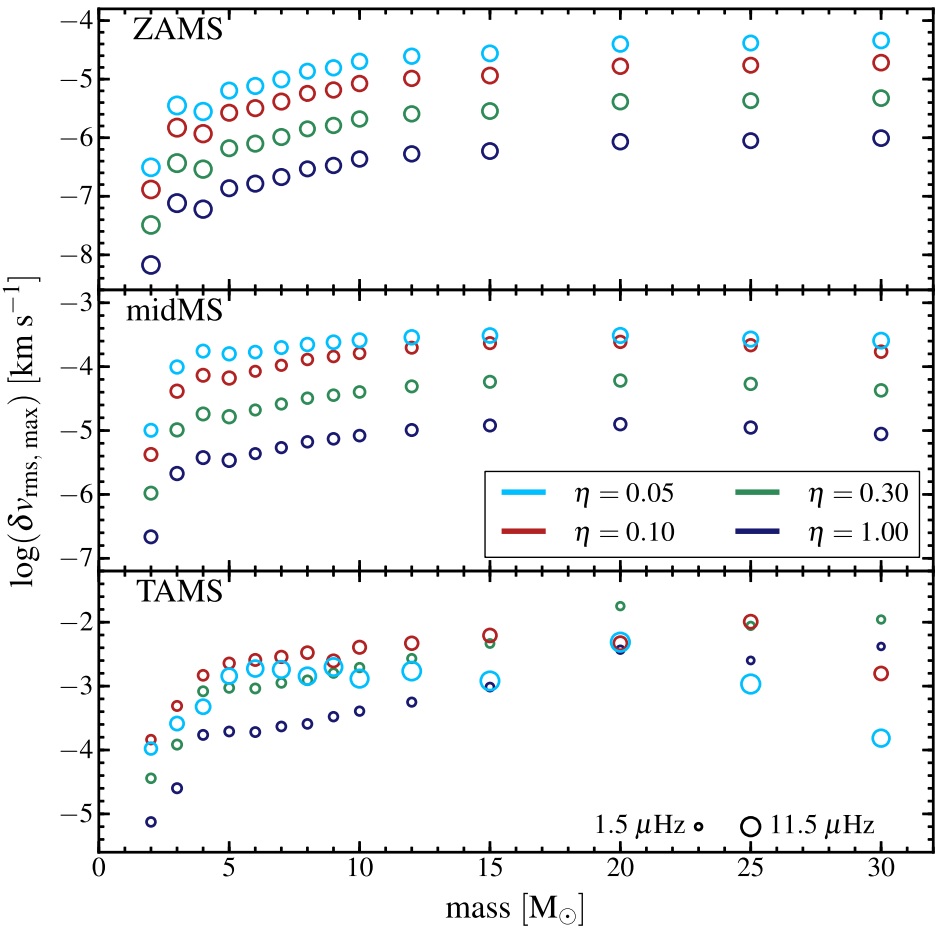

Figure 3.7: Peak RMS surface velocity fluctuations convectively excited g-modes as a function of mass. Symbols and colors are as in Fig. 3.6.

3.6.3 Observability of solar g-modes

We have also computed a solar model according to modern asteroseismology constraints, in order to determine the surface velocities of solar g-modes implied by our excitation model. If the excitation is dominated by the highly-stratified solar convection zone, g-modes of a given frequency ω are primarily excited at the place in the convection zone where $\omega \sim \omega_c(r)$ (Kumar et al. 1999). Thus high frequency g-modes are predominantly excited near the solar surface, while low frequency g-modes are excited near the radiative-convective boundary in the interior. Assuming the convection zone behaves like a polytrope with index $n \approx 1.5$, equation 3.1 still applies, but with $\ell_{\rm max} = r/H\,(\omega/\omega_c)^{2/3}$, where r and H are evaluated at the interior radiative-convective boundary where g-modes begin to propagate, $a = 7/2$, $b = 2$, and $\eta = 1$.

However, if the excitation is instead predominantly due to a thin overshoot region of width ηH at the base of the convection zone, then we assume the excitation spectrum at fixed position ($a = 13/2$), with $\eta < 1$. In Fig. 3.8, we show the disk-integrated g-mode velocity amplitudes that result from using the convection-zone-dominated and overshoot-dominated excitation spectra. In the overshoot case, we choose values $\eta = 0.05, 0.3$ that span the range suggested by helioseismic investigations and numerical simulations of solar convection (e.g., Christensen-Dalsgaard et al. 2011; Rogers & Glatzmaier 2005, 2006).

In all reasonable excitation scenarios, we find amplitudes of $\delta v_{\rm disk} \lesssim 0.3\,{\rm mm\ s^{-1}}$, which are consistent with those derived by Kumar et al. (1996). Our results are also consistent with the observational upper limits that place $\delta v_{\rm disk} \lesssim 10\,{\rm mm\ s^{-1}}$ at $\sim 100\,\mu$Hz (Appourchaux et al. 2010).

The intensity-to-velocity ratio we find for these high frequency solar g-modes is $\delta m/\delta v \lesssim 1\,\mu{\rm mag/\ cm\ s^{-1}}$, so that typical intensity perturbations are $\lesssim 10^{-2}\,\mu$mag. This is also well below the published upper limits from Appourchaux et al. (2000) of $\sim 0.5\,\mu$mag.

3.7 Discussion

Using a simple parametrization for the convective excitation of gravity modes, we predict that the convective cores of stars with masses $\gtrsim 2$ M$_\odot$ will excite observable surface brightness fluctuations while on the main sequence. If the excitation is dominated by an overshoot region having a width of $\lesssim 30$ per cent of the pressure scale height at the top of the convective core, these stars will exhibit intrinsic photometric variability with amplitudes up to 10s of micromagnitudes at frequencies of $5 - 10\ \mu$Hz ($0.4 - 0.8\,{\rm d^{-1}}$) on, or just red of the solar metallicity ZAMS. These flux variations are largest for massive stars with $M \gtrsim 5$ M$_\odot$ (Fig. 3.6).

As the stars evolve along the main sequence, we predict a strong increase in the flux variability, reaching 100s of micromagnitudes at frequencies $\lesssim 10\,\mu$Hz, along with the appearance of power at ever lower frequencies, down to $\sim 1\,\mu$Hz ($0.08\,{\rm d^{-1}}$) at the TAMS. We predict no observable accompanying velocity signal.

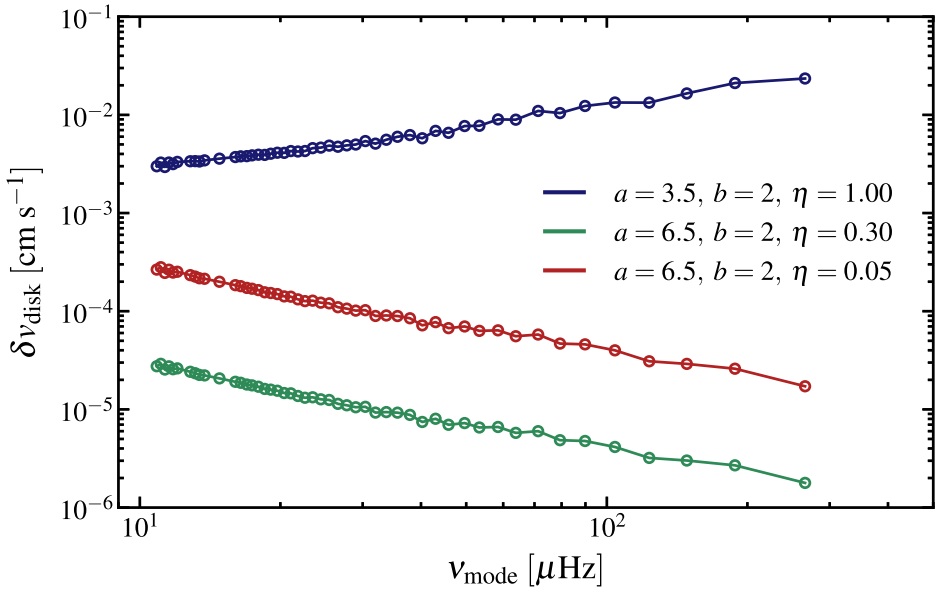

Figure 3.8: Disk-integrated velocity perturbations for $\ell = 1$ solar g-modes. For comparison, $\ell = 2, 3$ modes have smaller velocity perturbations by factors of ~ 3 and 10, respectively. The blue points show the amplitudes of modes assuming that the highly-stratified solar convection zone dominates the exciation, as compared to the green and red points which give the result of excitation by an overshoot region of 30 or 5 per cent of a pressure scale height, respectively.

Given the relatively low amplitudes of individual g-modes, we have framed our predictions in terms of the RMS flux variations at a given frequency, rather than the amplitudes of individual stellar normal modes. The latter are smaller by factors of $\sim 3 - 30$ at these frequencies (with larger corrections at lower frequencies), making it challenging to detect individual normal modes. However, as the duration of observation for *Kepler* and *CoRoT* stars increases, it may become possible to detect individual normal modes in a periodogram analysis, since the long lifetimes of these modes ensures that they will become more prominent in longer duration observations (e.g. Dupret et al. 2009).

Our excitation model agrees with previous predictions that the surface amplitudes of solar g-modes are $\lesssim 0.3\,\mathrm{mm\ s^{-1}}$ (Fig. 3.8), thus implying that *photometry of massive main sequence stars provides the best potential window into the convective excitation of g-modes.*

3.7.1 Theoretical uncertainties

Overshoot excitation

Detailed asteroseismic modeling provides a best fit width for the solar overshoot region ("tachocline") of between 5 and 40 per cent of a pressure scale height at the base of the convection zone, depending on the overshoot prescription used (Christensen-Dalsgaard et al. 2011, and references therein). Numerical simulations by Rogers & Glatzmaier (2005, 2006) imply an overshoot thickness at the small end of this range $\sim 0.05H$. However, asteroseismic results from other solar-like stars suggest that the thickness of the overshoot layer may not be universal even among similar stellar types (e.g., Lebreton & Goupil 2012).

For main sequence stars with core convection zones, numerical simulations by Browning, Brun, & Toomre (2004) find that the overshoot region has, in our terms, $\eta \lesssim 0.2$. Results from asteroseismic modeling of massive main sequence pulsators are broadly consistent with overshoot of a few tenths of a pressure scale height, but show a range of best fit parameters from consistent with zero (e.g., Aerts et al. 2011) to more than 40 per cent of a pressure scale height (e.g., Briquet et al. 2007); further corroboration is found in isochrone fitting of open clusters (Brott et al. 2011, and references therein). This broad base of observational results, in combination with arguments presented here, suggest that g-mode excitation by convective overshoot could produce observable surface brightness perturbations in massive main sequence stars.

Effects of rotation on g-modes

Using typical observed surface velocities for massive stars (e.g., Wolff et al. 2006), the corresponding rotation frequencies are given by

$$\Omega \approx 3.5\,\mu\mathrm{Hz}\,\left(\frac{v}{150\,\mathrm{km\ s^{-1}}}\right)\left(\frac{R}{\mathrm{R}_\odot}\right)^{-1}, \tag{3.14}$$

i.e., $\Omega \simeq 3\,(1)\ \mu$Hz for $M = 2\,(10)M_\odot$.

The effect of the Coriolis force on g-mode propagation can be seen in the WKB dispersion relation (as in e.g., Kumar et al. 1999, eqn. 21):

$$\omega^2 \approx 4\frac{\left(\mathbf{k}\cdot\mathbf{\Omega}\right)^2}{k^2} + N^2\frac{\left(\mathbf{k}\cdot\hat{\mathbf{g}}\right)^2}{k^2}, \tag{3.15}$$

Thus, g-modes only propagate where $\omega > 2\left(\Omega\cdot\hat{k}\right)$, and modes with frequencies $\omega \lesssim \Omega$ are confined to the equator.

As discussed in §3.6, much of the convectively excited power is in modes with frequencies of $\sim 1-5\,\mu$Hz, comparable to the median rotation frequencies of massive main sequence stars. Thus we expect that rotation will have a non-negligible effect on the surface manifestation of convectively excited g-modes (it may also change the excitation of g-modes since rapidly rotating convection has different statistical properties than non-rotating convection). This is particularly true as the star evolves to the TAMS. Given the potential importance of rotation, it would be particularly interesting to compare high precision photometry of slowly vs. rapidly rotating main sequence A-O stars.

Additionally, if the surface of the star is rotating more rapidly than the core, the star may possess critical layers that significantly increase the radiative damping of outgoing g-modes and preclude the establishment of standing waves. Such critical layers may in fact be set up by the angular momentum carried by the g-modes themselves (see e.g., Rogers, Lin, & Lau 2012).

Effects of stellar model parameters

To assess the effects of stellar modeling parameters on our predictions, we evolved a 10 $M_\odot$ star with variable mixing parameters and rotation. We tested mixing length parameters $\alpha_{\rm MLT} = 1, 1.5, 2$; boundaries determined by the Schwarzschild and Ledoux criteria without overshoot; and the Schwarzschild criterion with 30 per cent overshoot and initial surface rotation velocities of $50, 100, 200\,\mathrm{km\ s^{-1}}$ (with and without the chemical mixing induced by Taylor-Spruit magnetic fields).

We find that the uncertainty in our predicted mode amplitudes at fixed central hydrogen mass fraction due to stellar evolutionary parameters may be up to a factor of ~ 5, with the models presented in our figures roughly corresponding to the median of the distribution. Changing $\alpha_{\rm MLT}$ produces the largest effect, as larger $\alpha_{\rm MLT}$ corresponds to smaller ω_c and larger $\mathcal{M}_{\rm conv}$; the overall normalization of the convective excitation spectrum scales as $\alpha_{\rm MLT}^{-2}$ for $a = 13/2$ (see eqn. 3.1). Convective boundary definitions can also change the ratio of $\omega_{\rm min}/\omega_c$ by up to a few percent on the ZAMS, changing the fraction of the convectively excited g-mode power that reaches the stellar surface by $\lesssim 25$ per cent. By the end of the main sequnce these effects can amount to an order of magnitude dispersion among models, as the determination of convective boundaries affects the progression of stellar evolution.

Turbulent power spectrum

In their study of the detectability of solar g-modes, Belkacem et al. (2009a) employ a Lorentzian eddy-time-correlation function for coupling the turbulent convective motions to g-mode excitation. They find that this results in a 30-fold increase in solar g-mode amplitudes, as compared to the assumptions used in our analysis (and previous work; e.g., Kumar et al. 1996). Samadi et al. (2010) also employed this formalism to study convectively excited g-modes in 10, 15, and 20 $M_\odot$ main sequence models having $X_{ctr} = 0.5$. They find amplitudes of $\sim 10\,\mu$mag for individual $\ell = 1$ g-modes in these stars, also ~ 30 times larger than the amplitudes in our $\eta = 1$ case (see our Fig. 3.5 and their fig. 2).

Near-surface convection zones

Massive main sequence stars of near solar metallicity have vigorous near-surface convection zones due to the iron opacity bump (Cantiello et al. 2009). These convection zones are another potentially important source of g-modes near the stellar surface, having mach numbers of $\gtrsim 0.01$. Near-surface convection zones have characteristic frequencies of 10s to 100s of μHz, but the small scale-heights near the stellar surface imply that nearly all of the convective power is at larger characteristic $\ell \gtrsim 30$. These high ℓ g-modes are unlikely to produce any significant surface brightness perturbations, but, as suggested by Cantiello et al. (2009), the velocity field associated with these waves might account for the micro/macro-turbulent velocity fields inferred via spectroscopic modeling. We leave a detailed investigation of the excitation and propagation of these modes to future work.

3.7.2 Observational prospects

Distinguishing stochastically excited modes

Some of the stars we have investigated lie in the SPB instability strip, where stars are observed to pulsate in low-degree g-modes with frequencies of $0.6 - 3\,\mathrm{d}^{-1}$. These linearly excited modes have frequencies very near the peak of the stochastically excited modes. It is thus important to determine how to observationally distinguish between linearly and stochastically excited modes.

Unlike p-modes stochastically excited by envelope convection zones (i.e., solar-like oscillations), the convectively excited modes explored in this work have linear damping timescales (primarily due to radiative diffusion) of years or longer, much longer than a typical observation timescale. Thus the spectral broadening and time-frequency diagram characteristics that distinguish stochastically-driven modes in the former case cannot be leveraged here (e.g., Bedding 2011; Belkacem et al. 2009b). We must instead rely on the fact that convectively excited g-modes should be observable in stars outside the linear instability strips and at frequencies that should otherwise be damped in linear analyses.

Have convectively excited g-modes already been detected?

Aerts et al. (2009) have shown that the "macroturbulent" velocity fields observed in spectra of blue supergiants can be explained by the collective effect of an ensemble of excited g-modes, which span a similar frequency range to that presented here. More recent ongoing work by Simón-Díaz et al. (2011), has shown that macroturbulence is present in O and B dwarf stars as well, suggesting that perhaps the same low-frequency pulsations are present on the main sequence. We have shown however, that if individual mode amplitudes are set by the competition between convective excitation by the core and radiative damping in the envelope (see eqn. 3.9), the aggregate effect is too small to explain the observed macroturbulence (see Fig. 3.7). The source of these turbulent motions could instead be g-modes excited by near-surface convection zones, as discussed in §3.7.1 above and Cantiello et al. (2009). Another interesting possible source is the photon bubble instabilities that occur in the atmospheres of massive stars (Turner et al. 2004).

There is tantalizing evidence for convectively excited g-modes in recent observations of A, B and O stars with *Kepler* (Balona et al. 2011; Uytterhoeven et al. 2011; Blomme et al. 2011). In their study of B-star pulsators, Balona et al. (2011) find evidence for theoretically unexpected, low frequency pulsations in SPB stars and SPB/β Cep hybrid pulsators. Some of these stars lie outside the classical instability strips for low-order modes, potentially implying that a previously unexplored driving mechanism is at work in these stars.

In studies of O-stars, Blomme et al. (2011) have found an unexpected "red-noise" component to the stellar photometric power spectrum, even after instrumental corrections have been applied. This noise appears at the frequencies and amplitudes that agree with our predictions; however, the inferred mode lifetimes of hours to days for the "red-noise" modes are incommensurate with those of the g-modes explored here, which have lifetimes of years to Myrs.

As a general comment, we note that many studies remove or disregard power at low-frequencies below 0.5 or $0.2\,\mathrm{d}^{-1}$, depending on the study. They appeal to instrumental effects both known and un-characterised. However, we urge caution: the complete removal of this low frequency power may take with it the signatures of convectively excited g-modes.

Acknowledgments

We acknowledge a stimulating workshop at Sky House where these ideas germinated. We would like to thank Bill Paxton for invaluable support with MESA, Rich Townsend for providing non-adiabatic oscillation modes for comparison with our quasi-adiabatic calculations, and Conny Aerts and Neal Turner for helpful feedback that improved this work. JS would also like to thank the American Museum of Natural History for providing office space and support during the completion of this work. This work was partially supported by a Simons Investigator award from the Simons Foundation to EQ, the David and Lucile Packard Foundation, and the Thomas and Alison Schneider Chair in Physics at UC Berkeley.

Additional support was provided by the National Science Foundation under grants PHY 11-25915 and AST 11-09174, and by NASA Headquarters under the Earth and Space Science Fellowship Program - Grant 10-Astro10F-0030.

Chapter 4

Setting the Stage for Interacting Supernovae I: Theory of Wave-Driven Mass Loss

An earlier version of this chapter was previously published as Quataert, E., & Shiode, J. 2012, MNRAS, 423, L92.

Abstract

During the late stages of stellar evolution in massive stars (C fusion and later), the fusion luminosity in the core of the star exceeds the star's Eddington luminosity. This can drive vigorous convective motions which in turn excite internal gravity waves. The local wave energy flux excited by convection is itself well above Eddington during the last few years in the life of the star. We suggest that an interesting fraction of the energy in gravity waves can, in some cases, convert into sound waves as the gravity waves propagate (tunnel) towards the stellar surface. The subsequent dissipation of the sound waves can unbind up to several $M_\odot$ of the stellar envelope. This wave-driven mass loss can explain the existence of extremely large stellar mass loss rates just prior to core-collapse, which are inferred via circumstellar interaction in some core-collapse supernovae (e.g., SNe 2006gy and PTF 09uj, and even Type IIn supernovae more generally). An outstanding question is understanding what stellar parameters (mass, rotation, metallicity, age) are the most susceptible to wave-driven mass loss. This depends on the precise internal structure of massive stars and the power-spectrum of internal gravity waves excited by stellar convection.

4.1 Introduction

Many massive stars appear to lose a significant fraction of their mass in episodic outbursts rather than continuous line-driven winds (e.g., Bouret et al. 2005; Smith & Owocki 2006). There is strong evidence from observations of luminous supernovae (SNe) that the most extreme version of this phenomena is the ejection of $\sim 1 - 10 M_{\odot}$ of the stellar envelope in the last year to decade of massive stellar evolution (in a very small fraction of massive stars). In particular, the interaction between an outgoing supernova shock and such ejecta can explain some of the most optically luminous SNe yet detected (e.g., Smith & McCray 2007), including, e.g., SN 2006gy (Smith et al. 2007; Ofek et al. 2007) and perhaps the emerging class of hydrogen-poor ultraluminous SNe (Quimby et al. 2011; Chomiuk et al. 2011). In several cases, the late-time light curve disfavors one alternative explanation, that the luminosity is powered by unusually large amounts of radioactive Ni and Co (e.g., Miller et al. 2010; Chomiuk et al. 2011).

Related evidence for prodigious mass loss in the last few years of stellar evolution comes from SNe like PTF 09uj, which was interpreted as shock-breakout from an extremely dense circumstellar wind (Ofek et al. 2010), and those like SN 2006jc (Pastorello et al. 2007; Foley et al. 2007) and 2010mc (Ofek et al. 2013) which had directly observed luminous outbursts within a few years of core collapse. Even more typical Type IIn SNe (i.e., those displaying narrow emission lines indicative of circumstellar interaction) appear to require progenitor mass loss rates exceeding $\sim 10^{-2}\,\mathrm{M}_{\odot}\,\mathrm{yr}^{-1}$ (Kiewe et al. 2012; Fox et al. 2013), far larger than can be explained by continuous mass loss processes operating in massive stars.

One of the central puzzles posed by the circumstellar interaction scenario for luminous and Type IIn SNe and the observations of pre-SN outbursts is why a massive star should experience highly enhanced mass loss, and lose a significant fraction of its mass in some cases, in only $\lesssim 10^{-4}$ of its lifetime. In the case of luminous interacting SNe, prodigious mass loss is required even later, in the final $\sim 10^{-6.5}$ of the star's lifetime, in order for the supernova shock to encounter the stellar ejecta at radii ~ 100 AU where the shock is particularly radiatively efficient.

The most important change that occurs in the late stages of massive stellar evolution is the onset of prodigious neutrino cooling in the core of the star, associated with the high temperatures required for carbon fusion and beyond (see, e.g., Woosley et al. 2002 for a review). The fusion luminosities exceed Eddington for C fusion and later and become particularly large during the last year in the life of the star. The rapid fusion and neutrino cooling in turn accelerate the nuclear burning so that the characteristic nuclear timescale $\mathrm{t}_{\mathrm{nuc}}$ (analogous to the main sequence timescale for H-burning) decreases to a $\sim$ yr for Ne and O fusion and a $\sim$ day for Si fusion (with the exact values depending on stellar mass, metallicity, and rotation). Because neutrino cooling and fusion have different temperature sensitivities, it is in general not possible for neutrino cooling to balance nuclear heating everywhere in the core of the star, although in a volume averaged sense the two balance. This local difference between heating and cooling drives convection which carries a significant

convective luminosity $\sim 10s\,\%$ of the fusion luminosity.

In this Chapter, we argue that wave excitation by vigorous convection in the late stages of stellar evolution is capable of driving the strong mass loss suggested by circumstellar interaction in luminous core-collapse SNe. Such wave excitation has been explicitly seen in numerical simulations of carbon and oxygen shell fusion by Arnett and collaborators (e.g., Meakin & Arnett 2006); there is also closely related numerical work in the context of solar convection (e.g., Rogers & Glatzmaier 2005, 2006). Here we provide analytic estimates of wave excitation in evolved massive stars and discuss the resulting implications for mass loss in the last $\sim$ year of stellar evolution. We begin by summarizing some of the key properties of convection during carbon fusion and later and the excitation of internal gravity waves by such convection (§4.2). We then calculate the conditions under which a super-Eddington flux of waves excited in the core of the star can tunnel through to the stellar envelope (§4.3). Finally, in §4.4 we discuss the implications of our results and directions for future work.

Because there are significant uncertainties in the interior structure of massive stars during the evolutionary phases of interest, we focus on elucidating the general conditions required for efficient wave-driven mass loss. We defer to future work the problem of finding stellar progenitors that have all of the requisite properties. SNe with evidence for circumstellar interaction represent $\sim 10\%$ of all core-collapse events (Smith 2011); ultraluminous SNe are much rarer still (e.g., Quimby et al. 2011). This suggests that rather special stellar parameters are required to generate $\sim M_\odot$ of ejecta in the last $\sim$ year of stellar evolution.

4.2 Convection and wave excitation in late stages of stellar evolution

Table 4.2 summarizes some of the key properties of core fusion and convection during the late stages of stellar evolution (based on Woosley et al. 2002 and Kippenhahn & Weigert 1990).

For a stellar core with a mass $\sim M_\odot$, a convective luminosity $\mathrm{L_{conv}} \sim L_{\rm fusion}$ corresponds to a typical convective velocity $v_{\rm conv} \sim 10\,(\mathrm{L_{conv}}/10^9 L_\odot)^{1/3}\,(\rho_c/10^7\ \mathrm{g\ cm^{-3}})^{-1/9}\ \mathrm{km\ s^{-1}}$, where ρ_c is the central density. The corresponding convective Mach numbers are given in Table 4.2, and are $\gtrsim 0.01$ for Ne fusion and later. Although the parameters given in Table 1 are motivated by the core properties of evolved massive stars, similarly vigorous convection occurs during late stage shell burning. For example, Arnett & Meakin (2011) find convective luminosities and Mach numbers comparable to those given in Table 4.2 for shell O fusion during the hour prior to core collapse.

Figure 4.1 shows a mode propagation diagram for a 40 $M_\odot$, $Z = 10^{-4}$ metallicity model during core O fusion (at which point $R_\star \simeq 1700\,R_\odot$, $T_{\rm eff} \simeq 4000$ K, and $L_{\rm photon} \simeq 10^{5.8}\,L_\odot$). The model was evolved using the `MESA` 1D stellar evolution code (Paxton et al. 2011) with no mass loss. Convective boundaries are determined by the Schwarzschild criterion, and hydrogen- and non-burning convection zones have overshooting of 1% of the local pressure

Table 4.1: Late Stages of Massive Stellar Evolution

Stage	Duration (t_{nuc})	L_{fusion} ($L_\odot$)	Mach ($\mathcal{M}_{conv}$)	τ_c (s)
Carbon	$\sim 10^3$ yr	$\sim 10^6$	~ 0.003	$\sim 10^{4.5}$
Neon	~ 1 yr	$\sim 10^9$	~ 0.01	$\sim 10^3$
Oxygen	~ 1 yr	$\sim 10^{10}$	~ 0.02	$\sim 10^3$
Silicon	~ 1 day	$\sim 10^{12}$	~ 0.05	$\sim 10^2$

Note. — Fusion luminosities, durations, convective Mach numbers, and convective turnover times for core fusion during the late stages of stellar evolution of a $\sim 25 M_\odot$ star (based on Woosley et al. 2002). Precise values depend somewhat on stellar mass, metallicity, and rotation. Convective Mach number is an order of magnitude estimate assuming that a significant fraction of the fusion luminosity is locally carried by convection; depending on the stellar parameters, core carbon fusion may not be convectively unstable. Shell fusion of C, O, Ne, etc. can produce similarly vigorous convection.

scale height. This progenitor choice is somewhat arbitrary and thus unlikely to actually be the optimal progenitor for wave-driven mass loss. We include this model to provide a quantitative example of the propagation diagram and likely mode properties during very late stages of stellar evolution. For this particular stellar model, the core convection has a Mach number $\mathcal{M}_{conv} \sim 0.01$ and locally carries a luminosity $L_{conv} \sim 0.1\, L_{fusion} \sim 10^{9.5}\, L_\odot$, with a comparable convective luminosity in the shell C fusion present at $r \sim 0.03 R_\odot$.

Vigorous convection transfers some fraction of the turbulent kinetic energy into waves, both sound waves and internal gravity waves. For the specific stellar model in Fig. 4.1, the core convective region is bordered by a convectively stable region into which the internal gravity waves excited by convection can propagate. This is important because the roughly incompressible convective motions are much more efficient at directly exciting internal gravity waves than acoustic waves (Goldreich & Kumar 1990). Quantitatively, convection carrying a luminosity L_{conv} with a Mach number $\mathcal{M}_{conv}$ excites a total internal gravity wave luminosity of (Lecoanet & Quataert 2013)

$$L_{wave} \sim \mathcal{M}_{conv}^{5/8} L_{conv} \sim 10^8 \left(\frac{L_{conv}}{10^{10} L_\odot}\right) \left(\frac{\mathcal{M}_{conv}}{10^{-3}}\right)^{5/8} L_\odot. \tag{4.1}$$

This analytic estimate of the fraction of the convective energy transferred to internal gravity waves is consistent (at the order of magnitude level) with simulations of internal gravity wave excitation by solar convection (Rogers & Glatzmaier 2005, 2006).

The frequencies and wavelengths of the internal gravity waves are somewhat more

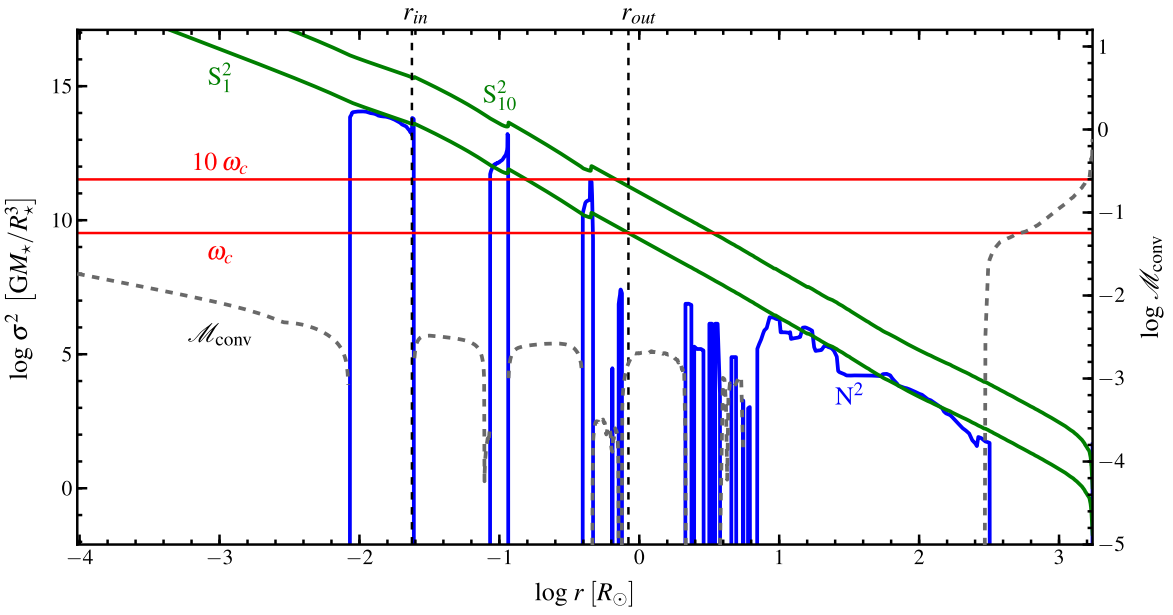

Figure 4.1: Propagation diagram for a 40 $M_\odot$ star with $Z = 10^{-4}$ during core O fusion, showing the Brunt-Väisälä frequency N (blue, solid line) and the Lamb frequency S_ℓ (for $\ell = 1$ and 10; green, solid) on the left ordinate, plotted as a function of radius. The convective mach number $\mathcal{M}_{\rm conv}$ (gray, dashed) is also shown on the right ordinate. The thin red lines show the convective turnover frequency in the core, and ten times that frequency, to demonstrate the range of internal gravity wave frequencies the core convection is likely to excite. The inner and outer radius of the tunneling cavity (r_{in} and r_{out}) for an $\ell = 1$ mode of frequency ω_c are marked on the top abcissa.

uncertain than the total wave luminosity given in equation 4.1. If the excitation is dominated by motions in the convection zone itself, the characteristic frequency associated with most of the wave power is the convective turnover frequency, $\omega \sim \omega_c \equiv \tau_c^{-1}$. Likewise, the horizontal spatial scale is set by the size of the convective eddies, so that the characteristic angular degree of the excited modes is $\ell \sim r/H$, where H is the size of the convective eddies and r is the radius where the excitation occurs (e.g., Kumar et al. 1999). For the core (and 'thick' shell) convection relevant here, this would correspond to modes having $\ell \sim$ few.

The uncertainty in these estimates is that much of the excitation may instead occur in a convective overshoot layer (Garcia Lopez & Spruit 1991; Rogers & Glatzmaier 2005, 2006). This increases both the frequency and angular degree ℓ of the excited waves because the length-scale over which the excitation happens is the thickness of the overshoot layer. For evolved massive stellar models the thickness of the overshoot layer is particularly uncertain because the vigorous convection itself generates significant mixing and may substantially modify the structure of the star relative to that predicted by 1D models (Meakin & Arnett 2006; Arnett & Meakin 2011). It is likely that the convective overshoot layer is significantly thicker in this circumstance than in the sun (where it is $\lesssim 0.05H$ at the interior convective-radiative transition; e.g., Christensen-Dalsgaard et al. 2011). This favors the excitation of lower ℓ waves with $\omega \sim \omega_c$. For our analytic estimates we will use

$$\omega \equiv f\,\omega_c = f\,\mathcal{M}_{\rm conv}\,\frac{c_s}{H} \sim f\,\mathcal{M}_{\rm conv}\,S_1 \tag{4.2}$$

where $f \sim 1 - 10$ is a dimensionless number that encapsulates the uncertainty associated with the wave excitation and S_1 is the $\ell = 1$ Lamb frequency. The characteristic wave frequencies $\omega = \omega_c$ and $\omega = 10\,\omega_c$ are shown with the thin red lines in Fig. 4.1.

4.3 Tunneling, trapping, and damping

4.3.1 Internal gravity waves

Depending on their frequency and angular degree, the energy supplied to internal gravity waves can either remain trapped in the central part of the star or tunnel out to the stellar envelope in the form of propagating sound waves.

We now estimate the conditions under which the latter occurs.

For internal gravity waves that become evanescent at a radius $r_{\rm in}$ and tunnel to a radius $r_{\rm out}$, the effective damping rate of the otherwise trapped mode due to leakage to large radii is given by (Unno et al. 1989)

$$\gamma_{\rm leak} \sim \frac{\mathrm{v_{group}}}{\mathrm{r_{in}}}\left(\frac{\mathrm{r_{in}}}{\mathrm{r_{out}}}\right)^{2\Lambda} \sim \omega\,\frac{\omega}{\Lambda\langle \mathrm{N}\rangle}\left(\frac{\mathrm{r_{in}}}{\mathrm{r_{out}}}\right)^{2\Lambda}, \tag{4.3}$$

where $\Lambda^2 = \ell\,(\ell+1)$ and $\langle N\rangle$ is the average Brunt-Väisälä frequency in the propagating region. The radii $r_{\rm in}$ and $r_{\rm out}$ are labeled in Fig. 4.1 for $\ell = 1$ modes with $\omega = \omega_c$. Physically,

the timescale for energy to leak out implied by equation 4.3 ($\sim \gamma_{\rm leak}^{-1}$) is given by the group travel time across the propagating region ($r_{in}/v_{\rm group}$) divided by the tunneling probability, i.e., the fraction of the mode energy that tunnels through the barrier in a given group travel time.

In addition to the tunneling captured by equation 4.3, the outgoing gravity waves can also be partially reflected by the rapid changes in composition at shell boundaries (see the spikes in N^2 in Fig. 4.1); this occurs if the wavelength of the waves is larger than the thickness of the region over which the composition changes. The latter is set by convective overshoot at the base of the shell convection zones and is probably a few percent of a scale height. Given this, we estimate that lower frequency gravity waves with $\omega \sim \omega_c$ are reasonably in the WKB limit in which equation 4.3 applies, but for higher frequency waves with $\omega \sim 10\omega_c$, the tunneling may be suppressed by an additional factor of ~ 10 due to the compositional boundaries.

Internal gravity waves of frequency ω (given by eq. 4.2) and degree ℓ excited at the outer edge of the core convection zone at radius $\sim r_{\rm prop}$ begin to tunnel at a radius $r_{\rm in} \sim 3r_{\rm prop}$ (based on the width of the convectively stable region at $\sim 0.01 R_\odot$ in Fig. 4.1). The radius where the tunneling ceases ($r_{\rm out}$) is determined by where $\omega > S_\ell$, so that the waves become propagating sound waves. For massive stellar models at radii $\sim 10^{-2} - 10\, R_\odot$, we find that the Lamb frequency can be reasonably approximated as a power-law in radius $S_\ell \propto r^{-b}$, with $b \sim 1.2 - 1.5$. Using equation 4.2 for the characteristic wave frequency, this implies $r_{\rm out}/r_{\rm in} \simeq 0.3\,(f\mathcal{M}_{\rm conv})^{-1/b}\Lambda^{1/b}$ and thus

$$\gamma_{\rm leak} \sim \left(\frac{r_{\rm in}}{r_{\rm prop}}\right)^{2\Lambda} \left(f\mathcal{M}_{\rm conv}\Lambda^{-1}\right)^{2[\Lambda/b]+1} \omega, \tag{4.4}$$

$$\gamma_{\rm leak} \sim 3^{2\Lambda} \left(f\mathcal{M}_{\rm conv}\Lambda^{-1}\right)^{2[\Lambda/b]+1} f\omega_c, \tag{4.5}$$

The dominant damping mechanisms for the gravity wave energy trapped in the core of the star are nonlinear damping and neutrino damping. The neutrino damping rate is

$$\gamma_\nu \sim 10 {\rm t}_{\rm therm}^{-1} \sim 100\, {\rm t}_{\rm nuc}^{-1} \tag{4.6}$$

where $t_{\rm therm}$ is the thermal (Kelvin-Helmholz) time and the factor of 10 in front of $t_{\rm therm}^{-1}$ is due to the strong temperature dependence of the neutrino reactions (so that a given perturbation in temperature gives rise to a yet stronger perturbation in neutrino cooling). The last expression in equation 4.6 is a consequence of the fact that the duration of nuclear burning ($\rm t_{nuc}$ in Table 4.2) in the late stages of massive stellar evolution is only a factor of ~ 10 longer than the thermal time. For some of the g-modes of interest it is possible that driving due to fusion may be stronger than the neutrino damping (see, e.g., Murphy et al. 2004). The interaction between convective excitation and such driving could be very interesting, but to be conservative, we do not explicitly include this driving in our estimates.

During O and Ne fusion, equation 4.6 implies that $\gamma_\nu \sim 3 \times 10^{-6}\,{\rm Hz} \sim 10^{-3}\,\omega_{\rm c}$, for $\omega_c \sim 3 \times 10^{-3}$ as shown in Fig. 4.1. Thus, neutrino damping is rather effective for modes of

frequency $\sim \omega_c$. For comparison, taking $\mathcal{M}_{\rm conv} \sim 0.01$, we find that $\gamma_{\rm leak} \gtrsim \gamma_\nu$ for modes with $\ell = 1$, if $f \gtrsim 3$. For $\ell = 2$, the condition is more prohibitive: high frequency modes having $f \gtrsim 10$ are required for leakage to dominate neutrino damping. This demonstrates that only the power in the lowest degree modes with $\ell \simeq 1-2$ is capable of efficiently leaking out into the stellar envelope. These low ℓ modes are, however, those that are expected to be excited by the large-scale convection in late stages of stellar evolution.

The nonlinear damping of internal gravity waves is somewhat more difficult to quantify. A useful measure of the nonlinearity in the propagating region is the dimensionless parameter $k_r\xi_r$ (the radial displacement relative to the radial wavelength): when $k_r\xi_r \gtrsim 1$, the waves can locally overturn the stratification leading to efficient nonlinear damping. Using conservation of energy flux, $k_r\xi_r$ for a traveling internal gravity wave of frequency ω can be rewritten as

$$k_r\xi_r \sim \Lambda^{3/2} \left(\frac{N}{\omega}\right)^{3/2} \left(\frac{\mathrm{F}_{\rm wave}}{\rho r^3 \omega^3}\right)^{1/2} \tag{4.7}$$

where $\mathrm{F}_{\rm wave} = \mathrm{L}_{\rm wave}/4\pi r^2$ is the local wave energy flux. Quantitatively, using the stellar progenitor shown in Fig. 4.1, and assuming $\mathrm{L}_{\rm wave} \sim 10^8 L_\odot$, we find that $k_r\xi_r \gtrsim 1$ for radii $\lesssim 0.015\, R_\odot$ for $\omega \sim \omega_c$, while $k_r\xi_r \lesssim 0.01$ at all radii of interest for $\omega \sim 10\omega_c$. Wave breaking is thus unlikely to significantly limit the energies attained by higher frequency internal gravity waves, which also tunnel the most effectively (this corresponds to larger f in eq. 4.4). However, wave breaking may be important for waves with frequencies $\sim \omega_c$. Indeed, Meakin & Arnett (2006) see some evidence for mixing induced by g-modes breaking in the convectively stable region separating O and C-burning shells in their simulations of late-stage burning in massive stars.

4.3.2 Sound waves

The outward energy flux in sound waves created as described in §4.3.1 dissipates well before reaching the stellar surface. In particular, we find that the dominant dissipation of the sound waves is via radiative diffusion. The sound waves damp when the radiative diffusion time $\sim 1/(k^2 K_{\rm rad})$ (where $K_{\rm rad}$ is the radiative conductivity) is shorter than the group travel time of the modes across a given scale-height of the star $\sim H/c_s$. This condition can be rewritten as

$$L_{\rm rad} \gtrsim L_{\rm damp} \equiv \frac{4\pi r^2 \rho c_s^3}{(kH)^2}, \tag{4.8}$$

where we have assumed that gas pressure is not much smaller than radiation pressure (which is reasonable for the conditions of interest). Fig. 4.2 shows $L_{\rm rad}$ (which is $\sim \mathrm{L}_{\rm Edd}$ even though the envelope is convective) and $L_{\rm damp}$ as a function of radius for modes with $\omega \sim 3\,\omega_c$ in the 40 $M_\odot$, $Z = 10^{-4}$ progenitor used in Fig. 4.1. The sound waves damp by radiative diffusion in the envelope at $r \sim 30 - 100\, R_\odot$.

The dissipation of the outgoing sound waves will drive convection in the outer stellar envelope. However, the convection ceases to be efficient when the wave luminosity is larger

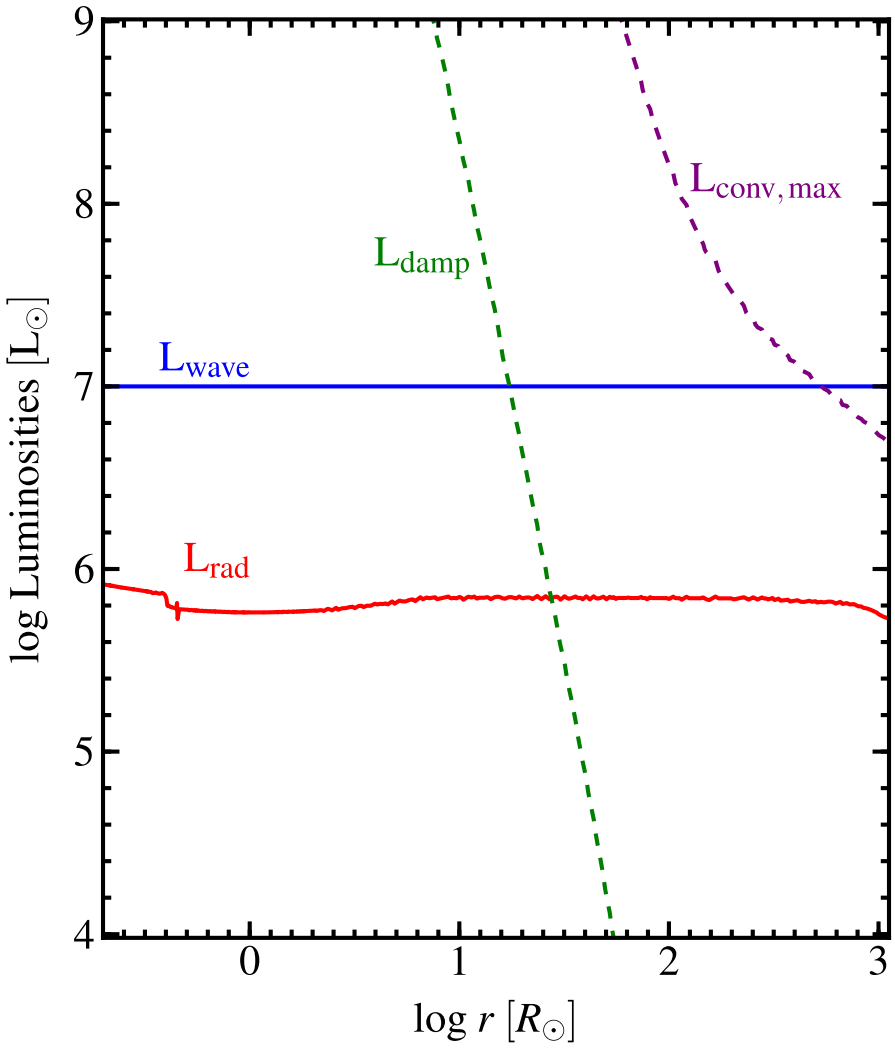

Figure 4.2: Critical luminosities that determine the dissipation of the outgoing wave power $L_{\rm wave}$ and the ability of convection to carry the thermalized energy. All quantities are for the $40M_\odot$, $Z = 10^{-4}$ stellar model from Fig. 4.1. Outgoing acoustic waves damp by radiative diffusion when the background radiative flux in the stellar model $L_{\rm rad}$ exceeds the critical luminosity $L_{\rm damp}$ (see eq. 4.8; $\omega = 3\,\omega_c$ for $L_{\rm damp}$ in this example). Subsonic convection cannot carry the thermalized wave power ($L_{\rm wave} = 10^7 L_\odot$ here) when $L_{\rm wave} \gtrsim L_{\rm conv,max} = 4\pi r^2 \rho c_s^3$. Taken together, these results imply that the super-Eddington wave power cannot be carried by either convection or radiative diffusion in the stellar envelope at $r \gtrsim 500 R_\odot$, leading to strong mass loss. There is $\sim 5M_\odot$ exterior to this radius in this example.

than the maximum energy that subsonic convection can carry $L_{\rm max,\,conv} = 4\pi r^2 \rho\, c_s^3$. So long as $L_{\rm wave} \gtrsim L_{\rm Edd}$, this will always occur inside the photosphere. For the specific model shown in Fig. 4.2, $L_{\rm wave} > L_{\rm max,\,conv}$ outside $\sim 500 R_\odot$. There is $\sim 5 M_\odot$ of mass exterior to this radius. The inability of convection or radiative diffusion to carry the outgoing wave energy implies that the wave power will inevitably drive a strong outflow. In particular, the mass outflow rate induced is likely to be $\dot{M} \sim 4\pi r^2 \rho c_s$ (evaluated where $L_{\rm wave} \sim L_{\rm conv,max}$, so that convection cannot carry the energy; this corresponds to the sonic point of the outflow). For the stellar model used in Figures 4.1 and 4.2, we find $\dot{M} \sim 10\,{\rm M}_\odot\,{\rm yr}^{-1}$ and $L_{\rm wave} \gtrsim \dot{M} v_{\rm esc}^2$ (for $L_{\rm wave} \gtrsim 10^7\, L_\odot$), so that the wave power is capable of driving a sustained outflow.

4.4 Discussion

The total energy released during Ne and O fusion in the last year of massive stellar evolution is $\sim 10^{51}$ ergs. We have shown that a significant fraction of this energy $\sim 10^{48-49}$ ergs – i.e., $L_{\rm wave} \sim 10^{41-42}$ erg s^{-1} – is converted into internal gravity waves via the Mach $\gtrsim 0.01$ convection that accompanies the enormous nuclear and neutrino luminosities in the cores of massive stars. We have further argued that a large fraction of the power in low angular degree ($\ell \sim$ few) modes can tunnel through to the stellar envelope and become outgoing acoustic waves.

If the low degree modes carry a significant fraction of the total wave power, the outgoing energy flux in acoustic waves will be significantly super-Eddington. The dissipation of the acoustic waves in the stellar envelope then drives convection that attempts to carry a super-Eddington power $\sim 10^{40-41}\,{\rm erg\ s}^{-1} \sim 10 - 100\,L_{\rm Edd}$. Such convection becomes inefficient inside the stellar photosphere (Fig. 4.2) and thus the end result of this wave energy deposition is almost certainly substantial mass loss. Assuming that the outgoing wave power can be maintained for a reasonable fraction of the duration of Ne and O core fusion, up to 10^{47-48} ergs is deposited in the stellar envelope. If the unbound material moves at $\sim 100 - 1000\,{\rm km\ s}^{-1}$, the wave power can unbind $\sim 10^{-2} - 10\,M_\odot$ of material.

Matter moving at $\sim 300\,{\rm km\ s}^{-1}$ ejected in the year prior to core-collapse will end up at ~ 100 AU when the star explodes. The mass-loss rates, ejecta mass, and the radial extent of the ejecta estimated here are consistent with the conditions required to explain SNe powered by circumstellar interaction between the SN shock and surrounding stellar ejecta. In particular, at the low end of our estimated mass loss rates ($\sim 10^{-3} - 10^{-2}\,{\rm M}_\odot\,{\rm yr}^{-1}$), circumstellar interaction can produce typical Type IIn supernovae (Kiewe et al. 2012). More extreme cases with ejecta masses approaching $\sim 0.1 - 1 M_\odot$ in the last year are comparable to what is needed to power the most luminous SNe ever detected (e.g., SN 2006gy, Smith et al. 2007; and the ultraluminous Ics, Quimby et al. 2011) as well as SNe powered by shock breakout in a dense circumstellar wind (e.g., Ofek et al. 2010). Moreover, our results provide an explanation for what is otherwise a fine tuning problem: why should the star happen to lose a non-negligible fraction of its mass in the last year of stellar evolution ($\sim 10^{-6.5}$ of its lifetime!)?

For red super-giant progenitors, the mechanism of mass loss proposed here operates primarily during core Ne and O fusion. During core C fusion, the energy flux in internal gravity waves is typically well below Eddington and so is unlikely to modify the stellar mass loss. During Si fusion, the wave luminosities are enormous, but the sound crossing time of a giant ($\sim$ few months) is much longer than the duration of the burning phase and so the star undergoes core-collapse before waves can reach the stellar surface. Nonetheless, the outgoing wave power created during Si fusion may substantially modify the structure of the progenitor star at radii $\lesssim 30 R_\odot$ (see Meakin & Arnett 2006). This could change how the supernova shock interacts with the surrounding star. In addition, in compact progenitors that have already lost their hydrogen envelopes, wave excitation during Si fusion could help drive substantial mass loss in the day prior to core-collapse. Such stripped envelope progenitors are of particular interest in the context of understanding whether circumstellar interaction powers hydrogen-poor ultra-luminous SNe (e.g., Quimby et al. 2011).

In the well-studied case of SN 2006gy – whose lightcurve is consistent with $\sim 10 M_\odot$ of ejecta in the 8 years prior to core-collapse (Smith et al. 2010) – there is also evidence for a comparable amount of ejecta $\sim 10^3$ years earlier (via an IR light echo; Miller et al. 2010). The wave-driven mass loss mechanism we have proposed cannot work in its present form for this earlier mass loss episode. Likewise, it is unlikely to be relevant to typical luminous-blue variable outbursts.

Our model for wave-driven mass loss requires that a reasonable fraction of the internal gravity wave power excited by convection reside in low ℓ modes with frequencies somewhat larger than the characteristic convective turnover frequency. The reason for the former condition is that high ℓ gravity waves cannot tunnel through to the stellar surface; their energy is instead trapped in the interior, where it is ultimately thermalized and radiated via neutrinos. The latter condition is required since lower frequency gravity waves will likely break locally within the g-mode propagating region and induce mixing (see eq. 4.7; such mixing could be very interesting in its own right: e.g., by bringing fresh fuel down to higher temperatures where it could in principle combust and power an eruption like those studied by Dessart et al. 2010). In their simulations of O shell fusion, Meakin & Arnett (2006) found significant wave power in $\ell = 4$ modes; since these simulations covered only a quadrant of the star, these were the lowest ℓ modes they could simulate. This is consistent with our hypothesis that the convection in the late stages of stellar evolution will be particularly large-scale and thus will excite low ℓ modes.

It is unclear whether core convection or shell convection is likely to be the most important source of waves for driving mass loss. Core convection tends to be more energetic and is likely larger scale, favoring the excitation of the low ℓ modes that tunnel most effectively. However, a countervailing consideration is that waves excited during shell convection have a smaller barrier to tunnel through. Further numerical work to calibrate the power-spectrum of wave excitation is clearly needed, particularly during core O and Ne fusion.

The basic energetics of core convection and wave excitation that we have highlighted apply to all massive stars. It is, however, clear on observational grounds that not all

massive stars undergo extreme mass loss in the year prior to core-collapse. Given that our mechanism requires that a significant fraction of the gravity wave power excited by convection is in relatively low ℓ modes and that the tunneling cavity not be too spatially extended, we suspect that the answer to this apparent tension is that only in certain progenitors (with particular mass, metallicity, and/or rotation) are these conditions satisfied. However, determining exactly which progenitors these are will require additional work. For example, as emphasized by Arnett & Meakin (2011), the structure of the core of the star itself depends on the mixing induced by the internal gravity waves and so standard one-dimensional models may not be sufficiently accurate to address these questions.

A second question that we have not addressed is how the star responds to the wave power deposited in the stellar envelope. It is possible that in some cases the stellar structure adjusts in such a way as to suppress the fraction of the wave power that can tunnel to large radii before much of the stellar envelope has been shed. This would limit the total amount of mass loss via wave energy deposition. This question will be explored in detail in future work.

Acknowledgments

We are grateful to Nathan Smith for many stimulating discussions that inspired us to think about this problem. We thank Bill Paxton for useful exchanges about `MESA` and Avishay Gal-Yam, Chris Kochanek, and the referee for useful comments. EQ was supported in part by the David and Lucile Packard Foundation. This work was also supported by NASA Headquarters under the NASA Earth and Space Science Fellowship Program Grant 10-Astro10F-0030.

Chapter 5

Setting the Stage for Interacting Supernovae II: Wave-Driven Mass Loss in Supernova Progenitors

A version of the following chapter will be submitted for publication in 2013.

Abstract

The broad class of interacting supernovae show evidence for intense mass loss during their final years leading up to core collapse. We have proposed one potential mechanism for producing these unexpected events, termed "wave-driven mass loss." Internal gravity waves, excited by convection in the stellar core, carry a super-Eddington flux into the stellar envelope and potentially unbind $\sim$ $M_\odot$ of material. The mechanism requires that convection preferentially excites long wavelength perturbations in a stellar interior with a relatively small separation between where gravity and pressure waves may propagate. In this Chapter, we explore the internal conditions of potential supernova progenitors using the 1-D stellar evolution code, `MESA star`, in search of those most susceptible to wave-driven mass loss. We find that $\sim$ 20 per cent of the supernova progenitors we survey excite $\sim 10^{46} - 10^{48}$ erg of energy in waves that can tunnel from the core to the envelope and potentially drive mass loss during at least one of the neon or oxygen burning phases (which occurs within a few months to a decade of core collapse). We argue that this energy can generate a powerful outflow and a massive circumstellar environment with $10^{-3} - 1\,M_\odot$ reaching $\lesssim 3 \times 10^{15}$ cm before explosion. During silicon burning, a $\lesssim 5$ day long phase for our progenitor models, the wave energy may inflate $\sim 10^{-3} - 1\,M_\odot$ of the stellar envelope to $\sim 10 - 100$s of solar radii in $\sim$ half of the progenitors examined. We thus argue that many compact, Wolf-Rayet-like, supernova progenitors will experience this wave-driven inflation during silicon burning and will thus have a significantly different supernova signature than traditionally assumed.

5.1 Introduction

There is a large and growing body of evidence demonstrating that many supernova (SN) progenitors experience episodes of intense mass loss as late as the weeks leading up to core collapse (e.g., Foley et al. 2007; Ofek et al. 2013; Mauerhan et al. 2013). These progenitors stand in stark contrast to the canonical picture of massive stars in their final $\sim 1000\,\mathrm{yr}$ prior to explosion, that of a "frozen" stellar envelope overlying a vigorously burning, neutrino-cooled core (e.g., Kippenhahn & Weigert 1990; Woosley et al. 2002). Direct observations of luminous outbursts that precede supernovae (SNe) like 2006jc (Foley et al. 2007; Pastorello et al. 2007), 2009ip (Mauerhan et al. 2013) and 2010mc (Ofek et al. 2013) and the unseen episodes of highly enhanced mass-loss inferred from observations of interacting SNe (Kiewe et al. 2012; Gal-Yam 2012; Ginzburg & Balberg 2012) point to dynamic conditions in the envelopes of SN progenitors as they approach explosion.

The mass-loss rates inferred, assuming SN emission powered by the interaction of the outgoing SN shock and the prior ejected mass, far exceed what is reproducible by line-driven winds, with derived rates of $\sim 10^{-3} - 1\,\mathrm{M}_{\odot}\,\mathrm{yr}^{-1}$ (e.g., Kiewe et al. 2012; Fox et al. 2013; Smith & McCray 2007). The total circumstellar masses inferred approach tens of solar masses in the most extreme cases (e.g., Ginzburg & Balberg 2012; Moriya & Tominaga 2012). Several candidate mechanisms capable of generating mass loss this prodigious have been proposed, including wave-driven mass loss (Quataert & Shiode 2012, hereafter QS12), common envelope interaction with a close companion (Chevalier 2012; Soker 2013), the pulsational pair instability (Rakavy et al. 1967), and local radiation-driven instabilities in the stellar envelope (Suárez-Madrigal et al. 2013). The first of these can best explain the apparent preponderance of episodic mass-loss in the final $\sim$ year leading up to core collapse (e.g. Ofek et al. 2013); we focus on it here.

In this Chapter, we will address two basic questions: How much energy is available in convectively excited waves during the final evolutionary phases of massive stars? And, in which evolutionary scenarios can this energy escape the core and generate a pre-SN outburst? To that end, we present an investigation of the interior conditions of a suite of core collapse SN progenitor models, spanning a decade in mass, metallicities from Population III to solar, and initial rotation velocities up to 80 per cent of critical (breakup).

This Chapter begins with a summary of the wave-driving mechanism laid out in Chapter 4 and QS12 (§5.2). We then continue with a description of the grid of 1-D stellar progenitors in §5.3. In §5.4, we present the results of our investigation of SN progenitor interiors and their susceptibility to wave-driven mass loss. The Chapter concludes with a brief discussion of the results (§5.5) and directions for future work (§5.6).

5.2 The wave driving mechanism

The wave-driven mass loss mechanism is discussed in detail in Chapter 4. In the following, we provide a brief summary of the key concepts, and update some of the relevant timescale

considerations.

5.2.1 Convective wave excitation

In the final stages of massive stellar evolution, i.e., carbon fusion and beyond, the core of the star is cooled predominantly by thermal neutrinos (e.g., Clayton 1984; Woosley et al. 2002). The nuclear luminosity is thus in equilibrium with the neutrino cooling, which may exceed the emergent stellar luminosity by many orders of magnitude. If each core burning phase releases $\sim 10^{51}$ erg by fusing $\sim$ $M_\odot$ of material, we expect characteristic fusion and neutrino luminosities of 10^7 $L_\odot$ for C-burning, 10^{10} $L_\odot$ for Ne and O-burning, and 10^{12} $L_\odot$ for Si-burning (based on burning timescales given in Table 5.1, and e.g., Woosley et al. 2002). In most models, the luminosities during C and Ne-fusion are in fact smaller by a factor of ~ 10 due to the small abundances of C and Ne left behind by the prior burning phases. The emergent radiative luminosity for these SN progenitors is roughly equal to the Eddington luminosity for electron scattering in the stellar envelope: characteristically, $\sim 10^5 - 10^6$ $L_\odot$ for core collapse SN progenitors.

Due to the different temperature dependences of the nuclear burning and neutrino emission rates, local regions within the core are convectively unstable, with convection carrying a significant fraction of the nuclear luminosity, $\lesssim 10$ per cent. Thus, convection may carry a luminosity that exceeds the envelope Eddington value during C-burning, and does so by many orders of magnitude during Ne burning and beyond. This convection has characteristic mach numbers of $\sim 10^{-3} - 0.03$ (see also Table 4.2).

At the interfaces between these convection zones and neighboring stable regions, a radius we call $r_{\rm prop}$, convection transfers a fraction of its luminosity to linear, propagating gravity modes (g-modes) in that layer (e.g., Press 1981; Goldreich & Kumar 1990; Lecoanet & Quataert 2013). The top panel of Fig. 5.1 shows an example propagation diagram (analogous to fig. 4.1) for a 40 $M_\odot$ 10^{-1} $Z_\odot$ progenitor during core oxygen burning; here $r_{\rm prop}$ is the innermost labeled radius, marking the boundary between the oxygen burning core convection zone and the neighboring stably stratified layer (where the $N^2 > 0$) where g-modes propagate.

In Chapter 4, we used the estimate from the earlier literature that the energy flux in internal gravity waves is $L_{\rm wave} \sim \mathcal{M}_{\rm conv} L_{\rm conv}$ (eqn. 4.1). This is, however, only appropriate for a model in which the transition between the convective and radiative zones is discontinuous (Lecoanet & Quataert 2013). High frequency internal gravity waves have longer wavelengths in the radiative zone and thus indeed see the transition as approximately discontinuous. This is not, however, the case for the gravity modes that carry most of the wave energy flux, those with frequencies comparable to the convective turnover frequency (which have shorter wavelengths in the radiative zone). The excitation of these energy-bearing waves depends on the structure of the radiative-convective transition and thus depends on details that are not well-modeled in 1-D stellar evolution calculations. Lecoanet & Quataert (2013) argued that a smooth transition is more physical and leads to a larger energy flux than given by

eqn. 4.1. For a particular analytically tractable smooth model of the radiative-convective transition, they found that the wave luminosity excited by convection is

$$\mathrm{L}_{\mathrm{wave}} \sim \mathcal{M}_{\mathrm{conv}}^{5/8}\, \mathrm{L}_{\mathrm{conv}} \sim 10^{8} \left(\frac{\mathrm{L}_{\mathrm{conv}}}{10^{10} L_{\odot}}\right) \left(\frac{\mathcal{M}_{\mathrm{conv}}}{10^{-3}}\right)^{5/8} L_{\odot}, \tag{5.1}$$

where there is a dimensionless pre-factor in front of eqn. 5.1 that depends on the properties of the radiative-convective transition. It is not possible to calculate this pre-factor with existing 1-D stellar evolution calculations. Thus we set this to 1 while noting that it could be smaller if the radiative-convective transition is very thin (i.e., closer to discontinuous).

The spectrum of waves excited by convection is also somewhat uncertain (though constraints may be forthcoming from precision observations of massive main sequence stars; see Chapter 3). In broad terms, the convection most efficiently excites waves with characteristics similar to the energy-bearing eddies (e.g. Press 1981; Lecoanet & Quataert 2013). Thus, the wave energy is likely concentrated in waves with frequencies near ω_c, where $\omega_c \approx v_{\mathrm{conv}}/\min(r, H)$ is the Brunt-Väisälä frequency in the convection zone; and with horizontal lengthscales corresponding to spherical harmonic degrees $\ell \sim r_{\mathrm{prop}}/H(r_{\mathrm{prop}})$. However, the lowest frequency waves, those with $\omega \approx \omega_c$, have non-linear amplitudes and break as soon as they reach the radiative zone.[1] Thus, in the following, we focus on the linear, propagating waves with frequencies $\omega \gtrsim 3\,\omega_c$.

5.2.2 The fate of gravity modes: tunneling vs. neutrino losses

Convectively excited g-modes in the cores of evolved massive stars damp through one of two main channels: locally via neutrino losses or by tunneling out of the g-mode propagation cavity (we will also refer to the latter as "leakage"). Due to the highly temperature sensitive neutrino emission rates, positive (negative) temperature perturbations associated with waves lose more (less) energy via neutrino emission than the background, damping the perturbations. Nuclear fusion in the core may provide driving via an analogous, but opposite in sign, process known as the ϵ-mechanism, but we ignore this small contribution for simplicity. Leakage arises because the envelope of the star can often host acoustic waves of the same frequencies as the g-modes propagating in the core. Convectively excited g-modes can couple to the acoustic propagation cavity if they can tunnel through the intervening forbidden region (barrier) and are above the envelope's acoustic cutoff frequency, $\omega_{ac} \approx c_{\mathrm{s}}/(2\,H)$ (see e.g., Unno et al. 1989).

Larger lengthscale (low ℓ) waves decay slower through the barrier and higher frequency waves see smaller barriers (see Chapter 4). Thus, g-modes with these characteristics have the highest probability of tunneling, rather than damping to neutrinos. Whether a progenitor can drive mass loss by convectively excited waves depends first on the capacity for advanced convective burning to excite sufficiently high frequency and low ℓ waves to high energy.

[1] Eqn. 5.1 gives the luminosity in linear g-modes and does not include the energy associated with these immediately non-linear waves.

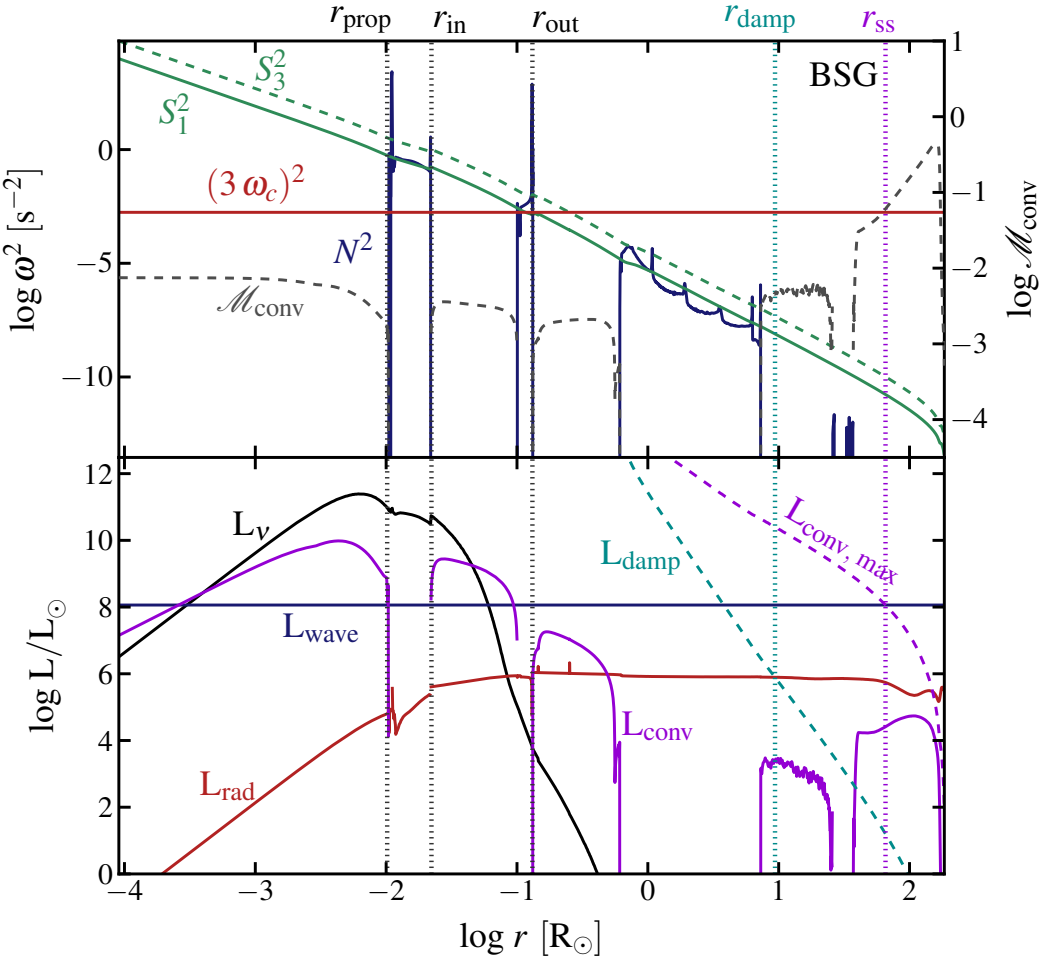

Figure 5.1: Propagation diagram (top panel) and luminosity plot (bottom panel) for a 40 $M_\odot$ 10^{-1} $Z_\odot$ blue supergiant progenitor at core oxygen burning. The propagation diagram shows the Brunt-Väisälä frequency (solid blue line), Lamb frequency for $\ell = 1, 3$ (solid and dashed green lines, respectively) and the propagating g-mode frequency excited by the core during this timestep (red solid line) against the left axis. The convective mach number is plotted as the dashed grey line against the right axes. The luminosity plot shows the relevant local luminosities in each shell of the model: the neutrino luminosity (L_ν) in solid black, radiative ($L_{\rm rad}$) in solid red, convective ($L_{\rm conv}$) in solid magenta, the radiative damping luminosity ($L_{\rm damp}$) in dashed teal (see eqn. 5.6), maximum convective luminosity ($L_{\rm max,\,conv}$) in dashed magenta (see eqn. 5.7), and the wave luminosity ($L_{\rm wave}$) excited during this timestep as the blue solid line. The radii relevant for wave-driven mass loss are marked by vertical dotted lines, and labeled at the top. The propagation radius, $r_{\rm prop}$, is shown in grey, as are the inner and outer radii of the tunneling region, $r_{\rm in}$ and $r_{\rm out}$, respectively. The damping radius, $r_{\rm damp}$, is shown in teal, where $L_{\rm rad} = L_{\rm damp}$, and $r_{\rm ss}$ in magenta, where $L_{\rm wave} = L_{\rm max,\,conv}$; $r_{\rm ss}$ is where the convection driven by wave energy deposition becomes supersonic and likely initiates an outflow.

We argued in Chapter 4 that g-modes damp primarily via tunneling if they leak faster than they damp to neutrinos:

$$t_{\rm leak} < t_\nu, \tag{5.2}$$

where the leakage time is given by the group travel time across the g-mode cavity, divided by the tunneling probability[2]:

$$t_{\rm leak} \approx t_{\rm g} \left(\frac{r_{\rm out}}{r_{\rm in}} \right)^{2\,\Lambda}, \tag{5.3}$$

and the group travel time is given by

$$t_{\rm g} = \int_{r_{\rm prop}}^{r_{\rm in}} \frac{dr}{v_{\rm group,\,r}}, \tag{5.4}$$

where $r_{\rm in}$ is the inner radius of the tunneling region (outer edge of the g-mode propagation cavity) and $r_{\rm out}$ is the outer radius of the tunneling region (inner edge of the p-mode propagation cavity; see Fig. 5.1 for the locations of these radii for an example mode). The neutrino damping time is set by the characteristic time for neutrino losses from the g-mode propagation cavity, enhanced by the temperature sensitivity of the neutrino losses:

$$t_\nu \approx \frac{\int_{r_{\rm prop}}^{r_{\rm in}} e_{\rm int}\, dm}{\left(\frac{d\ln \epsilon_\nu}{d\ln T}\right)_\rho \int_{r_{\rm prop}}^{r_{\rm in}} \epsilon_\nu(r)\, dm}, \tag{5.5}$$

where $e_{\rm int}$ is the internal energy per unit mass for the stellar material, $\epsilon_\nu(r)$ is the neutrino energy loss rate per unit mass, $dm \equiv 4\pi r^2 \rho\, dr$, and $(d\ln\epsilon_\nu / d\ln T)_\rho \sim 9$ for neutrino losses due to pair-annihilation.

The size of the g-mode propagation cavity, $r_{\rm prop}$ to $r_{\rm in}$, is roughly independent of frequency for the frequencies of convectively excited g-modes (see Fig. 5.1), fixing the approximate neutrino damping timescale given in eqn. 5.5. The leakage timescale, on the other hand, depends strongly on the width of the tunneling region, $r_{\rm out}/r_{\rm in}$ and the rate at which waves decay through the barrier. Both decline with decreasing ℓ, while the former also declines with increasing wave frequency.

Equation 5.3 was derived under the WKB assumption, wherein the waves are assumed to vary on lengthscales much shorter than the background. For many of the compact progenitor models we survey here (i.e. WR stars), this assumption is invalid in the envelope (acoustic propagation cavity) for the frequencies of convectively excited g-modes. Equivalently, these modes have frequencies below the acoustic cutoff for the stellar envelope and are likely reflected before reaching that cavity. In the following, we consider waves with $3\,\omega_c \lesssim \omega_{ac}$ as precluded from tunneling.

[2]In some cases, particularly compact progenitors, the most energetic, propagating g-modes have frequencies on the same order as ω_{ac} in the envelope; there is likely an additional inhibiting contribution to the tunneling probability in these cases because the outer turning point $r_{\rm out}$ is part of the thin stellar atmosphere. This correction is not accounted for here.

There may be a further inhibiting contribution to the tunneling probability due to the composition barriers present at the interfaces of convective and radiative zones, which may introduce variations on lengthscales shorter than the wavelength. The width and magnitude of these barriers depends sensitively on the treatment of mixing and convective boundaries. We do not attempt to account for it here, but acknowledge that it is an uncertainty in our calculation.

5.2.3 Acoustic waves and mass loss

Waves that satisfy eqn. 5.2 and have frequencies above the acoustic cutoff frequency in the envelope damp predominantly by tunneling out to the stellar envelope, where they may be carrying a significantly super-Eddington luminosity as acoustic waves. In the envelope, these waves damp either when the radiative damping timescale becomes comparable to the wave travel time or when the wave reaches non-linear amplitudes: $\xi_r\,\omega \sim c_\mathrm{s}$ (see Chapter 4). The former condition can be represented as

$$\mathrm{L_{rad}} \gtrsim \mathrm{L_{damp}} \equiv \frac{4\pi r^2 \rho\, c_\mathrm{s}^3}{(k\,H)^2}, \tag{5.6}$$

where k is the wavenumber of the propagating acoustic wave. The latter condition is equivalent to

$$\mathrm{L_{wave}} \gtrsim \mathrm{L_{max,\,conv}} \equiv 4\pi r^2 \rho\, c_\mathrm{s}^3. \tag{5.7}$$

In the following, we call r_damp the location where waves satisfy eqn. 5.6 and r_ss where they satisfy eqn. 5.7 (where the "ss" is meant to indicate "supersonic"). The bottom panel of Fig. 5.1 demonstrates the locations of these radii, based on eqns. 5.6 and 5.7, for an example mode.

Except in some compact progenitors, waves reach eqn. 5.6 first, deeper in the star, after traveling on the sound crossing time, t_sound, from r_out to r_damp. The sound crossing time is generally short enough to be unimportant. At r_damp, the wave energy damps by radiative diffusion and creates a local region with a significantly super-Eddington flux. In order to drive an outflow, the deposited wave energy must reach r_ss, where even $\mathcal{M}_\mathrm{conv} \gtrsim 1$ cannot carry the total luminosity. If r_damp is in the convection zone, energy moves quickly outward on a timescale

$$t_\mathrm{eddy} \approx \left.\frac{H}{v_\mathrm{conv}}\right|_{r_\mathrm{damp}} \approx H(r_\mathrm{damp}) \left(\frac{\mathrm{L_{wave}}}{4\pi r_\mathrm{damp}^2\, \rho(r_\mathrm{damp})}\right)^{-1/3}. \tag{5.8}$$

If, instead, $r_{\rm damp}$ is in a stably stratified radiative zone, the deposited energy must heat the local material enough to drive convection. This occurs on a (generally much longer) timescale

$$t_{\rm heat}(r) \approx \frac{\int_{r_{\rm damp}}^{r} e_{\rm int} dm}{\rm L_{wave}}, \tag{5.9}$$

where the terminal radius, $r = \min(r_{\rm ss}, r_{\rm env,\,cz})$, and $r_{\rm env,\,cz}$ is the base of a pre-existing envelope convection zone (if one exists). If there is a pre-existing convection zone, the wave energy need only heat enough material to extend the convection zone down to $r_{\rm damp}$. If there is not one, or $r_{\rm ss} < r_{\rm env,\,cz}$, the wave energy must heat all the material between $r_{\rm damp}$ and $r_{\rm ss}$ to potentially drive an outflow. This of course depends sensitively on the details of how the convection zone grows; it might in fact grow more quickly by entrainment (as described in e.g., Arnett et al. 2009). We use eqn. 5.9 in the following as it represents a conservative estimate of the timescale for energy to reach $r_{\rm ss}$ after damping at $r_{\rm damp}$.

Convection necessarily fails to carry the energy at $r_{\rm ss}$, where the total luminosity exceeds $\rm L_{max,\,conv}$. At this point, even $\mathcal{M}_{\rm conv} \gtrsim 1$ convection cannot carry the total luminosity. This can result in a strong pre-SN outflow, so long as $t_{\rm sound}$, $t_{\rm heat}$ and $t_{\rm eddy}$ are all shorter than the time to core collapse. In compact progenitors where convectively excited waves have frequencies above the envelope acoustic cutoff, waves reach eqn. 5.7 first, potentially driving a strong outflow on $\lesssim$ the sound travel time to the stellar surface.

For progenitors in which wave energy can reach $r_{\rm ss}$ prior to core collapse, we assume that this leads to an outflow and estimate the mass loss rates and total potential ejecta mass for the given burning phase as follows. At $r_{\rm ss}$, $\mathcal{M}_{\rm conv} \gtrsim 1$ convection is required to carry the outgoing flux; thus $r_{\rm ss}$ represents a sonic point in a potential outflow. The mass loss rate for this outflow will be

$$\dot{M} \approx 4\pi r_{\rm ss}^2 \, \rho \, c_{\rm s}(r_{\rm ss}). \tag{5.10}$$

Since $\rm L_{wave} = L_{max,\,conv}$ at $r_{\rm ss}$, the kinetic energy of the proposed outflow, $1/2\,\dot{M} v_{\rm esc}^2(r_{\rm ss})$, will exceed the wave luminosity so long as $c_{\rm s} < v_{\rm esc}$, which it must be for bound stellar material.

Thus, the outgoing wave luminosity cannot energetically sustain an outflow with the full $\dot{M}$ implied by the sonic point arguments; the star is in a regime analogous to the "photon-tired" wind discussed by Owocki et al. (2004). This could lead to inflation of the envelope to larger radii. However, we view this as unlikely because the total wave energy deposited at $r_{\rm ss}$ generally exceeds the binding energy of the star at $r > r_{\rm ss}$. Thus, we suspect an outflow with a smaller $\dot{M}$ than given in 5.10 is the most likely outcome. Owocki et al. (2004) also argue for the latter, positing the development of a porous atmosphere in the presence of super-Eddington luminosities. This provides low density channels out of which radiation can flow and drive a lower density wind. The true outcome of this super-Eddington energy deposition clearly depends on multi-dimensional effects, which will need to be examined using hydrodynamical models. These are, however, beyond the scope of this work.

In this "photon-tired" regime, we can estimate the ejecta mass, assuming the wind taps into the full wave luminosity via a lower $\dot{M}$ outflow:

$$\mathrm{M_{ej}} \lesssim \frac{2\,\mathrm{E_{wave}}}{v_{\mathrm{esc}}^2(r_{\mathrm{ss}})}. \tag{5.11}$$

In this case, we can estimate the mass loss rate as

$$\dot{M} \approx \frac{\mathrm{M_{ej}}}{t_{\mathrm{fusion}}}, \tag{5.12}$$

where t_{fusion} is the timescale for the relevant burning phase that generates $\mathrm{E_{wave}}$ used in eqn. 5.11.

5.3 Stellar Models

We use the `MESA star`[3] stellar evolution code (version **4789**; Paxton et al. 2011) to construct evolutionary sequences from the zero-age main sequence (ZAMS) to core collapse for supernova progenitors ranging in initial mass from 12 to 100 $\mathrm{M_\odot}$, metallicity from 0 (i.e., Population III) to solar, and initial angular velocities from 0 to 0.8 critical (see Appendix A for more details on the `MESA star` parameters we employ). Paxton et al. (2013) provides updated, detailed descriptions of the stellar evolution physics and numerical scheme employed by `MESA star`. Thus, we provide only a brief summary of the key aspects of our specific calculations, and refer the reader to that comprehensive work for details.

All models employ the Grevesse & Sauval (1998) chemical mixture, OPAL opacities (Rogers & Iglesias 1992), and updated nuclear reaction parameters for the $^{12}\mathrm{C}(\alpha,\gamma)^{16}\mathrm{O}$ (Kunz et al. 2002), $^{14}\mathrm{N}(\mathrm{p},\gamma)^{15}\mathrm{O}$ (Imbriani et al. 2005), and triple-alpha (Fynbo et al. 2005) reactions.

We determine convective boundaries using the Ledoux criterion, with a mixing length parameter $\alpha = 1.5$, semiconvection with a dimensionless efficiency parameter, $\alpha_{sc} = 0.1$, and thermohaline mixing with efficiency, $\alpha_{th} = 2.0$. On the main sequence, we use 33.5 per cent of a pressure scale height of overshoot above the convective core[4], following the results of Brott et al. (2011). Beyond the main sequence, we ignore overshoot for simplicity.

For the majority of our calculations, we assume the theoretical mass loss rates of Vink, de Koter, & Lamers (2001) when $T_{\mathrm{eff}} > 10^4\,\mathrm{K}$ and de Jager et al. (1988) when $T_{\mathrm{eff}} < 10^4\,\mathrm{K}$, each scaled down by a dimensionless efficiency factor of 0.8 for non-rotating models ("0.8 (v+dj)") and 0.6 for rotating models ("0.6 (v+dj)"). For rotating models, the mass-loss rate is allowed to increase above this prescription by up to a factor of ten, in order expel any surface layers whose rotation would be super-critical (see Paxton et al. 2013 for a more

[3] http://mesa.sourceforge.net/

[4] We use a step function overshoot prescription, in which the convection zone is extended a distance of 33.5 per cent of a pressure scale height above the Ledoux boundary, with a constant diffusion coefficient.

thorough description). In order to test the effect of the mass loss prescription on the results, we also include calculations for high mass, solar metallicity progenitors, where we use the Nieuwenhuijzen & de Jager (1990) rates for $T_{\rm eff} < 10^4\,{\rm K}$ and a dimensionless efficiency factor of 1.0 ("v+n"); this more closely matches the prescription described in Woosley et al. (2002).

For rotating progenitors, we employ compositional mixing and angular momentum transport via all magnetohydrodynamic (MHD) instabilities available in version 4789 of `MESA star`, except that we follow Paxton et al. (2013) and ignore the Solberg-Hoiland contribution to the convective instability criterion. The magnetic field is assumed to arise via the Spruit-Tayler dynamo (Spruit 2002). In detail, we do not believe the angular momentum transport processes in stellar interiors are well understood. We include the rotating progenitor models to give an order-of-magnitude indication of how different single star evolution outcomes can be when stellar rotation is included.

Table 5.1 summarizes the properties of our grid of evolutionary calculations for a total of 76 progenitor models. The table gives the initial values for mass, metallicity, and rotation, as well as the mass loss scheme, and shows how these map to final core masses, burning timescales, and our progenitor classifications. Progenitor classifications are based on the structure of the final model prior to core collapse. We define a red supergiant (RSG) as a star with a hydrogen envelope and $T_{\rm eff} < 10^4\,{\rm K}$, a blue supergiant (BSG) as a star with a hydrogen envelope and $T_{\rm eff} \geq 10^4\,{\rm K}$, and a Wolf-Rayet (WR) as a star that has lost its hydrogen envelope. These classifications correspond to stars with radii $300 - 10^3\,{\rm R}_\odot$ for RSGs, $3 - 300\,{\rm R}_\odot$ for BSGs and $0.4 - 1.6\,{\rm R}_\odot$ for WRs. Note that in our calculations, none of the progenitors lose their helium envelopes prior to core collapse. Broadly, the results in Table 5.1 show that our solar metallicity progenitors with $M_{\rm ZAMS} \gtrsim 30\,{\rm M}_\odot$ become WR stars, lower ZAMS mass solar metallicity stars generally produce RSGs, and low-metallicity stars produce BSGs. At fixed $M_{\rm ZAMS}$, moderate rotation produces bigger helium core masses through mixing, while the largest initial rotation values lead to smaller cores due to the rotational enhancement of the stellar wind.

Figures 5.2, 5.3 and 5.4 show examples of the convective history, plotted against $\log t_{\rm cc}$, where $t_{\rm cc}$ is time to core collapse, for each of our progenitor categories. Fig. 5.2 shows the history of a 12 $M_\odot$, solar metallicity, slowly rotating progenitor that becomes a RSG; Fig. 5.3 shows a 60 $M_\odot$, 0.1 $Z_\odot$, non-rotating progenitor that becomes a BSG; Fig. 5.4 shows a 40 $M_\odot$, solar metallicity, non-rotating progenitor that makes a WR. In these diagrams, stellar mass is plotted against the time to core collapse, in years, so that each plot shows the convective history from the ZAMS to ~ 30 seconds from core collapse ($\log t_{\rm cc} = -6$). The mass extent of each convection zone in the star is marked by the darker gray shaded regions, overshoot mixing (on the main sequence only) is shown in light gray, semiconvection in green, and thermohaline mixing in magenta. Also plotted are the mass boundaries of the He, C/O, O/Ne/Mg, and iron cores as a function of time to core collapse. For the He, C/O and O/Ne/Mg cores, these boundaries are determined by the first mass coordinate interior to the surface (or the previous mass boundary) where hydrogen, helium or carbon

Table 5.1: Stellar model properties

M_{ZAMS}	Z_{init}	Ω/Ω^*_{crit}	Mass Loss**	Class†	M_{He}‡	$M_{C/O}$	M_{iron}	$M_{env,H}$	$M_{env,He}$	Convective (radiative) core burning time***					
$[M_\odot]$	$[Z_\odot]$				$[M_\odot]$	$[M_\odot]$	$[M_\odot]$	$[M_\odot]$	$[M_\odot]$	H [Myr]	He [Myr]	C [yr]	Ne [yr]	O [yr]	Si [day]
12	0	0.00	0.8 (v+dj)	RSG	3.17	1.98	1.51	5.89	3.98	15.0	0.85	6600.0	6.300	5.800	4.90
12	10^{-2}	0.00	0.8 (v+dj)	RSG	4.39	2.14	1.49	5.31	4.14	19.0	1.10	3800.0	4.300	4.000	3.60
12	10^{-1}	0.00	0.8 (v+dj)	RSG	4.35	2.11	1.45	4.49	3.89	19.0	1.10	4900.0	3.600	4.300	4.40
12	1.0	0.00	0.8 (v+dj)	RSG	4.21	1.97	1.44	3.99	3.85	18.0	1.10	5600.0	4.600	5.000	5.50
12	1.0	0.20	0.6 (v+dj)	RSG	4.94	2.34	1.46	3.75	4.00	16.0	0.99	3100.0	3.700	2.800	3.60
12	1.0	0.50	0.6 (v+dj)	RSG	2.79	2.36	1.53	3.54	4.00	17.0	0.97	2900.0	6.100	3.400	3.70
12	1.0	0.80	0.6 (v+dj)	RSG	6.57	3.20	1.49	1.86	4.78	21.0	0.75	1300.0	0.780	3.100	2.80
15	0	0.00	0.8 (v+dj)	BSG	3.62	2.82	1.45	6.98	4.86	12.0	0.66	2300.0	0.960	4.100	4.70
15	10^{-2}	0.00	0.8 (v+dj)	RSG	5.84	2.93	1.49	6.26	5.12	14.0	0.80	1800.0	4.400	2.100	2.40
15	10^{-1}	0.00	0.8 (v+dj)	RSG	5.82	2.86	1.53	4.50	4.51	14.0	0.81	1900.0	3.200	2.100	2.20
15	1.0	0.00	0.8 (v+dj)	RSG	5.72	2.78	1.50	3.67	4.29	13.0	0.82	2100.0	4.300	2.200	2.80
15	1.0	0.50	0.6 (v+dj)	RSG	6.69	3.26	1.58	3.45	4.53	12.0	0.73	1200.0	3.500	2.300	2.10
15	1.0	0.80	0.6 (v+dj)	RSG	9.48	4.69	1.65	0.80	4.54	16.0	0.59	(230.0)	0.660	0.700	0.89
20	0	0.00	0.8 (v+dj)	BSG	5.24	4.45	1.46	8.44	6.55	8.7	0.50	650.0	0.520	1.600	3.50
20	10^{-2}	0.00	0.8 (v+dj)	RSG	7.78	4.40	1.59	6.99	6.45	9.9	0.55	560.0	0.290	0.420	1.10
20	10^{-1}	0.00	0.8 (v+dj)	RSG	8.49	4.26	1.53	3.21	5.06	9.9	0.58	540.0	0.910	1.600	2.30
20	1.0	0.00	0.8 (v+dj)	RSG	8.44	4.55	1.60	1.99	4.37	9.0	0.58	550.0	0.430	0.490	0.90
20	1.0	0.20	0.6 (v+dj)	RSG	7.70	5.12	1.64	2.71	5.04	8.5	0.55	(330.0)	0.640	1.300	1.60
20	1.0	0.50	0.6 (v+dj)	RSG	9.70	5.30	1.48	2.17	4.93	8.7	0.54	(340.0)	0.260	0.770	2.20
20	1.0	0.80	0.6 (v+dj)	WR	10.96	7.47	1.85	–	2.21	11.0	0.48	(150.0)	1.200	0.380	0.65
25	0	0.00	0.8 (v+dj)	BSG	9.41	6.73	1.57	9.84	7.86	7.0	0.43	(280.0)	0.140	0.360	1.30
25	10^{-2}	0.00	0.8 (v+dj)	RSG	11.05	6.65	1.83	2.67	6.18	7.8	0.46	(180.0)	0.910	0.300	0.55
25	10^{-1}	0.00	0.8 (v+dj)	RSG	11.34	6.43	1.64	1.38	5.49	7.8	0.46	(240.0)	0.110	0.230	0.95
25	1.0	0.00	0.8 (v+dj)	RSG	11.16	6.48	1.82	0.85	4.71	7.1	0.47	(210.0)	0.160	0.150	0.64
25	1.0	0.20	0.6 (v+dj)	RSG	12.39	7.39	1.63	0.97	5.04	6.8	0.47	82.0	0.620	0.670	0.82
25	1.0	0.50	0.6 (v+dj)	RSG	13.07	8.11	1.64	0.55	4.69	7.2	0.45	62.0	0.450	0.590	0.89
25	1.0	0.80	0.6 (v+dj)	WR	11.36	8.67	1.79	–	1.29	8.9	0.47	(110.0)	1.300	0.390	0.77
30	0	0.00	0.8 (v+dj)	BSG	11.90	8.50	1.68	11.10	9.83	6.0	0.37	(110.0)	0.360	0.530	0.74
30	10^{-2}	0.00	0.8 (v+dj)	RSG	13.98	9.11	1.53	1.18	6.24	6.6	0.41	(100.0)	0.490	0.660	1.90
30	10^{-1}	0.00	0.8 (v+dj)	RSG	14.28	8.81	1.55	0.85	6.31	6.6	0.40	(100.0)	0.320	0.490	1.00
30	1.0	0.00	0.8 (v+dj)	WR	13.86	8.07	1.64	–	4.24	6.0	0.41	(82.0)	0.300	0.490	1.10
30	1.0	0.20	0.6 (v+dj)	BSG	15.46	9.65	1.78	0.45	5.29	5.8	0.42	37.0	0.120	0.190	0.91
30	1.0	0.50	0.6 (v+dj)	BSG	16.33	10.49	1.86	0.35	5.16	6.1	0.41	(58.0)	(0.100)	0.160	0.76
30	1.0	0.80	0.6 (v+dj)	WR	12.65	9.67	1.52	–	0.96	7.4	0.44	60.0	0.750	0.870	2.50
40	0	0.00	0.8 (v+dj)	RSG	17.48	14.49	1.85	12.57	11.09	4.8	0.36	(26.0)	(0.079)	0.095	0.69
40	10^{-2}	0.00	0.8 (v+dj)	RSG	20.02	14.11	1.87	1.42	8.44	5.2	0.34	(24.0)	(0.078)	0.093	0.59
40	10^{-1}	0.00	0.8 (v+dj)	BSG	20.37	13.98	1.97	0.85	7.84	5.2	0.35	(34.0)	(0.072)	0.093	0.62
40	1.0	0.00	v+n	WR	10.04	7.63	1.73	–	0.31	4.8	0.43	(170.0)	0.240	0.180	0.73
40	1.0	0.00	0.8 (v+dj)	WR	13.10	10.24	1.51	–	0.32	4.8	0.39	(67.0)	0.410	0.490	1.50
40	1.0	0.20	0.6 (v+dj)	WR	20.41	14.77	1.67	–	3.81	4.7	0.36	(15.0)	(0.061)	0.067	1.50
40	1.0	0.50	0.6 (v+dj)	WR	20.01	15.61	2.10	–	2.55	4.9	0.36	9.8	(0.058)	0.068	1.10
40	1.0	0.80	0.6 (v+dj)	WR	13.77	11.22	1.58	–	0.21	5.7	0.41	(41.0)	0.380	0.360	1.50
50	0	0.00	0.8 (v+dj)	RSG	23.13	19.60	1.75	9.97	12.21	4.2	0.33	(11.0)	(0.040)	0.044	1.00
50	10^{-2}	0.00	0.8 (v+dj)	BSG	26.28	20.05	1.74	1.91	10.01	4.5	0.32	(13.0)	(0.041)	0.046	1.10
50	10^{-1}	0.00	0.8 (v+dj)	BSG	26.61	19.40	1.75	0.85	8.40	4.5	0.33	(17.0)	(0.042)	0.046	0.89
50	1.0	0.00	0.8 (v+dj)	WR	12.35	9.44	1.67	–	0.34	4.2	0.40	(78.0)	0.570	0.650	2.00
50	1.0	0.00	v+n	WR	10.42	7.99	1.83	–	0.30	4.2	0.41	(150.0)	1.100	0.330	0.63
50	1.0	0.20	0.6 (v+dj)	WR	24.19	20.15	1.76	–	2.17	4.1	0.34	(10.0)	(0.031)	0.038	0.86
50	1.0	0.50	0.6 (v+dj)	WR	22.33	16.34	1.74	–	0.44	4.2	0.34	(9.8)	(0.037)	0.044	1.00
50	1.0	0.80	0.6 (v+dj)	WR	14.36	11.65	1.59	–	0.25	4.9	0.40	(28.0)	(0.340)	0.220	1.30
60	0	0.00	0.8 (v+dj)	BSG	29.15	25.39	2.27	3.16	11.45	3.8	0.31	(9.6)	(0.024)	0.028	0.28
60	10^{-2}	0.00	0.8 (v+dj)	BSG	32.60	25.34	1.99	1.98	11.42	4.0	0.31	(7.0)	(0.026)	0.026	0.52

Continued on Next Page...

Table 5.1 — Continued

M_{ZAMS}	Z_{init}	Ω/Ω^*_{crit}	Mass Loss**	Class†	M_{He}‡	$M_{C/O}$	M_{iron}	$M_{env,H}$	$M_{env,He}$	Convective (radiative) core burning time***					
$[M_\odot]$	$[Z_\odot]$				$[M_\odot]$	$[M_\odot]$	$[M_\odot]$	$[M_\odot]$	$[M_\odot]$	H [Myr]	He [Myr]	C [yr]	Ne [yr]	O [yr]	Si [day]
60	10^{-1}	0.00	0.8 (v+dj)	BSG	32.75	24.84	2.20	0.13	7.18	4.1	0.31	(7.8)	(0.025)	0.024	0.31
60	1.0	0.00	v+n	WR	11.70	9.08	1.57	–	0.32	3.8	0.39	(81.0)	0.770	0.860	2.40
60	1.0	0.00	0.8 (v+dj)	WR	15.14	12.09	1.71	–	0.33	3.8	0.37	(38.0)	(0.200)	0.170	0.81
60	1.0	0.20	0.6 (v+dj)	WR	26.93	21.57	2.12	–	0.52	3.7	0.32	(4.9)	(0.020)	0.029	0.39
60	1.0	0.50	0.6 (v+dj)	WR	24.56	20.61	1.81	–	0.44	3.8	0.33	(7.9)	(0.033)	0.040	0.65
60	1.0	0.80	0.6 (v+dj)	WR	15.67	12.74	1.76	–	0.33	4.3	0.39	(24.0)	(0.220)	0.150	0.78
70	0	0.00	0.8 (v+dj)	BSG	34.99	30.95	2.63	3.60	13.42	3.5	0.30	(5.2)	(0.017)	0.019	0.24
70	10^{-2}	0.00	0.8 (v+dj)	BSG	38.95	31.00	2.54	2.35	13.18	3.7	0.29	(5.8)	(0.019)	0.017	0.25
70	10^{-1}	0.00	0.8 (v+dj)	BSG	38.97	30.89	2.58	0.05	7.77	3.7	0.29	(4.9)	(0.018)	0.018	0.24
70	1.0	0.00	v+n	WR	13.54	10.65	1.63	–	0.31	3.5	0.37	(57.0)	0.300	0.250	1.20
70	1.0	0.00	0.8 (v+dj)	WR	17.45	14.20	1.87	–	0.35	3.5	0.35	(22.0)	(0.100)	0.097	0.62
70	1.0	0.20	0.6 (v+dj)	WR	24.21	20.24	1.70	–	0.41	3.4	0.33	(4.9)	(0.035)	0.043	0.94
70	1.0	0.50	0.6 (v+dj)	WR	25.68	18.53	1.97	–	0.41	3.5	0.33	(4.3)	(0.028)	0.039	0.38
70	1.0	0.80	0.6 (v+dj)	WR	16.43	13.36	1.78	–	0.38	3.9	0.38	(21.0)	(0.180)	0.130	0.88
80	1.0	0.00	0.8 (v+dj)	WR	18.89	15.23	2.01	–	0.31	3.3	0.34	(19.0)	(0.074)	0.075	0.93
80	1.0	0.00	v+n	WR	8.45	6.22	1.51	–	0.32	3.3	0.44	290.0	1.500	1.800	2.20
80	1.0	0.20	0.6 (v+dj)	WR	19.83	16.31	2.13	–	0.40	3.3	0.36	(9.1)	(0.080)	0.075	0.78
80	1.0	0.50	0.6 (v+dj)	WR	18.61	15.11	2.08	–	0.40	3.3	0.36	(14.0)	(0.098)	0.086	0.64
80	1.0	0.80	0.6 (v+dj)	WR	17.54	14.26	2.04	–	0.39	3.6	0.37	(16.0)	(0.130)	0.110	0.72
100	1.0	0.00	0.8 (v+dj)	WR	9.81	7.45	1.66	–	0.34	3.0	0.43	(170.0)	0.130	0.200	0.96
100	1.0	0.00	v+n	WR	6.34	4.49	1.57	–	0.34	3.1	0.52	850.0	0.740	0.690	1.40
100	1.0	0.20	0.6 (v+dj)	WR	19.01	13.14	2.08	–	0.40	3.0	0.36	(11.0)	(0.100)	0.089	0.65
100	1.0	0.50	0.6 (v+dj)	WR	18.06	14.73	2.04	–	0.40	3.3	0.37	(10.0)	(0.130)	0.100	0.60
100	1.0	0.80	0.6 (v+dj)	WR	17.47	14.25	1.95	–	0.40	3.5	0.37	(22.0)	(0.140)	0.110	0.79

*$\Omega^2_{crit} \equiv (1 - L/L_{Edd})GM_\star/R^3_\star$.

*ast Here, "vdj" is shorthand for the Vink et al. (2001) and de Jager et al. (1988) mass loss prescription combination and the dimensionless efficiency factor is shown as a prefactor; "v+n" denotes the Vink et al. (2001) and Nieuwenhuijzen & de Jager (1990) mass loss prescription combination.

† We define "RSG" as a progenitor that retains its hydrogen envelope and has $T_{eff} < 10^4$ K at core collapse, "BSG" as progenitor with a hydrogen envelope and $T_{eff} \geq 10^4$ K, and a "WR" as a progenitor without hydrogen.

‡ Helium core mass at core infall; same as the "He core mass" plotted on the abcissa of figs. 5.8, 5.10, and 5.11.

*** Burning lifetimes are determined based on the time it takes for burning to reduce the central abundance of the main fuel below 10^{-5}. Except for Ne, which does not fully deplete before core oxygen burning, for which we estimate the lifetime based on the start of Ne burning to the start of O burning. Note that the lifetime of the central convection zone, when one exists, may be shorter than the lifetime of the burning phase given here (integrated energies relevant for excited waves span only the convective lifetime).

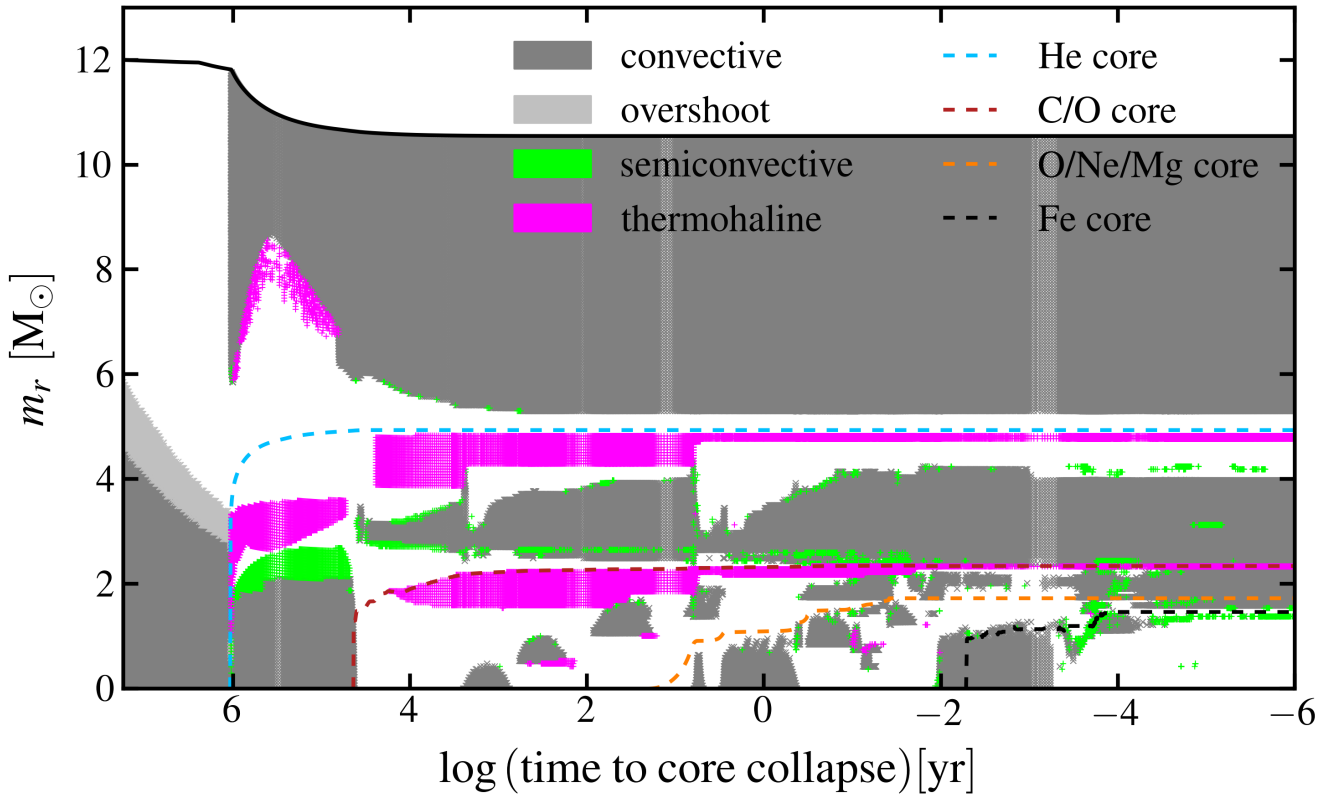

Figure 5.2: The convective history of a 12 $M_\odot$, solar metallicity star initially rotating at 20 per cent of the critical rotation velocity, plotted against log time to core collapse, in years. This star becomes a red supergiant SN progenitor with a 4.94 $M_\odot$ helium core and a 5.61 $M_\odot$ hydrogen envelope. For each timestep, the dark grey represents mass coordinates that are convective, light grey those that have overshoot, green those with semiconvection, and magenta those with thermohaline mixing. For example, for $\log t_{\rm cc} \gtrsim 6$ (far left), the star is on the main sequence and has a convective core burning hydrogen that recedes in mass with time from $m_r \sim 4.5 - 3\,M_\odot$, with a $\sim 1.5\,M_\odot$ overshoot region above it. The dashed lines show the mass boundaries of the various cores, light blue shows the boundary of the helium (i.e., hydrogen-depleted) core, red the C/O (i.e., H and He-depleted) core, orange the O/Ne/Mg core, and black the iron core. The O/Ne/Mg core, for example, moves out in mass with time as carbon is depleted by burning in the core and shells.

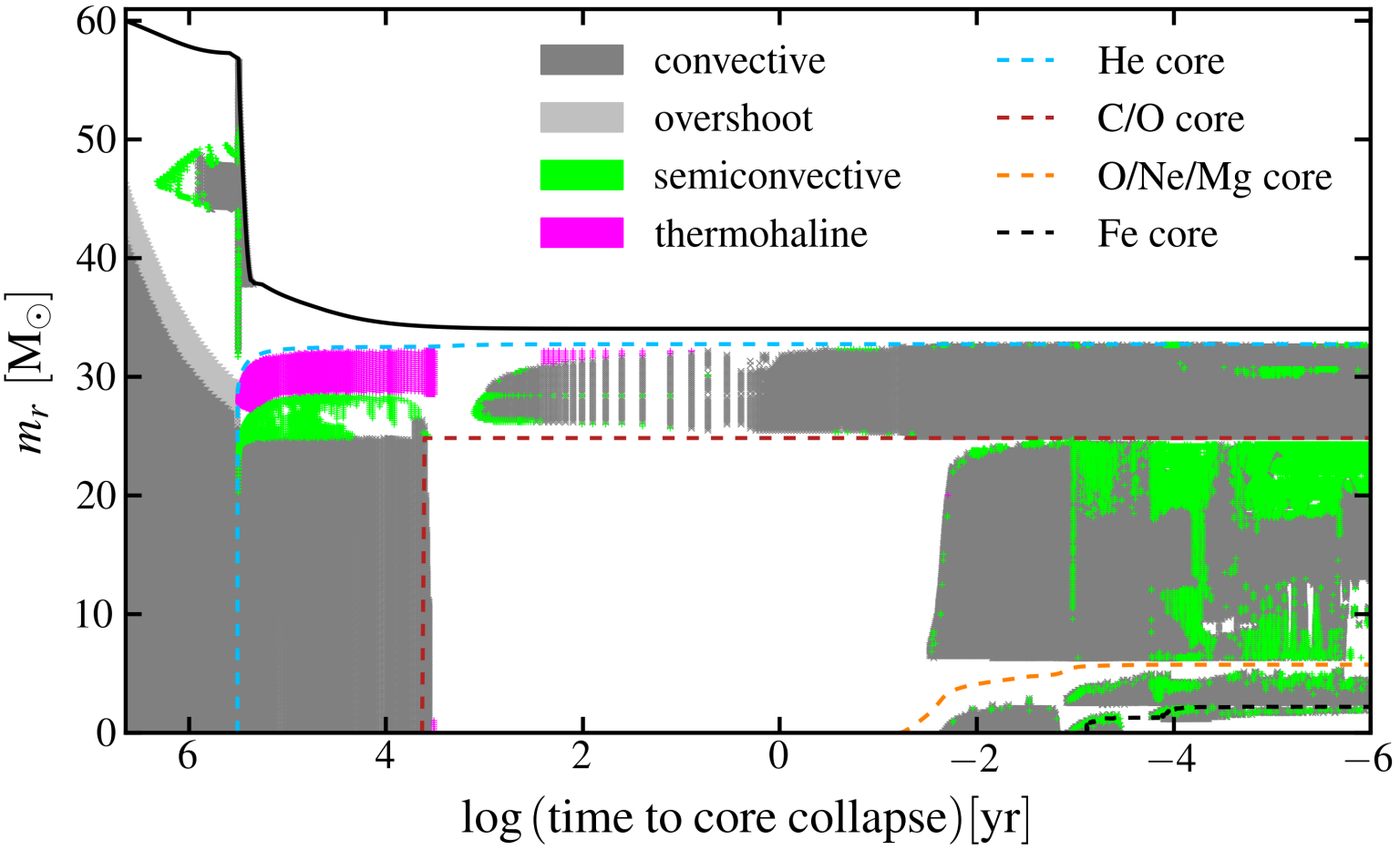

Figure 5.3: The convective history of a 60 M$_\odot$, one-tenth solar metallicity non-rotating star, plotted against log time to core collapse, in years. This star becomes a blue supergiant SN progenitor with a 32.75 M$_\odot$ helium core and a 1.3 M$_\odot$ radiative hydrogen envelope. Colors and lines have the meanings described in fig. 5.2.

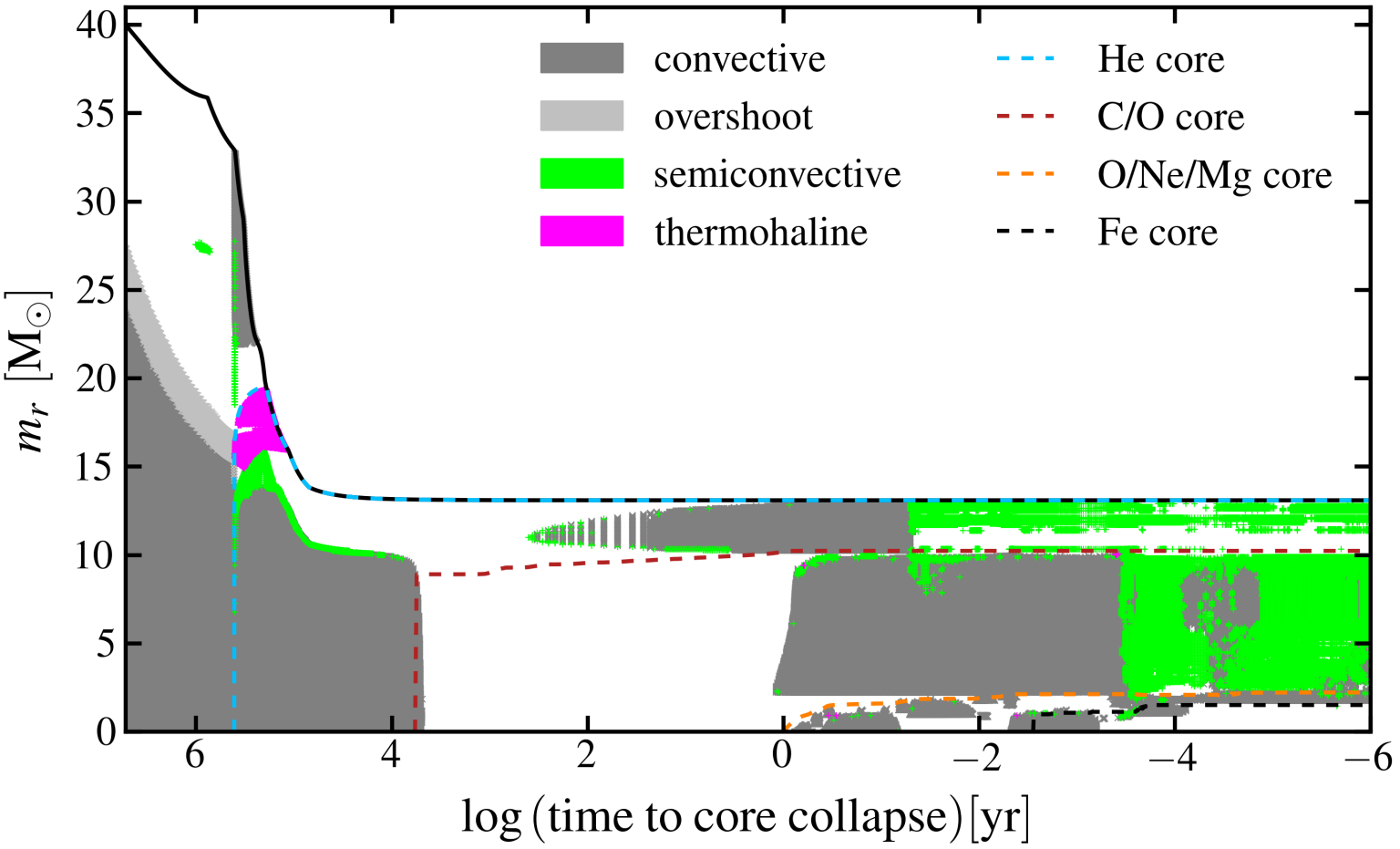

Figure 5.4: The convective history of a 40 M$_\odot$, solar metallicity, non-rotating star, plotted against log time to core collapse, in years. This star becomes a Wolf-Rayet SN progenitor with a 13.1 M$_\odot$ helium core. Colors and lines have the meanings described in fig. 5.2.

drops below a mass fraction of 10^{-4}. For the iron core, the boundary is determined by the first mass coordinate inward from the boundary of the O/Ne/Mg core where the total mass fraction of iron-group elements rises above 0.5.

5.3.1 Effect of opacity enhancements

In massive stellar envelopes, radiation pressure provides a significant fraction of the pressure support even when the opacity is set by electron-scattering (Kippenhahn & Weigert 1990). Significant opacity enhancements due to transitions of iron at $\log T \sim 5.2$ and the recombination of HeII ($\log T \sim 4.7$) and H ($\log T \sim 4$) lead to regions of the stellar envelope where the Eddington luminosity is greatly exceeded locally and gas pressure and density inversions can result (Paxton et al. 2013). In order to evolve through these computationally difficult stages of evolution, we employ the "enhanced mixing length theory" described in Paxton et al. (2013), which may crudely account for an energy transport mechanism not present in our 1-D models, such as the development of porosity (Shaviv 2001; Owocki et al. 2004). We thus sacrifice accuracy in the surface evolution in favor of completing the core evolution all the way to core collapse. This implies, however, that our progenitor classifications (RSG, BSG, and WR) have significant uncertainties.

5.4 Results

We present the results of our calculations by core burning phase: carbon, neon, oxygen, and silicon burning. Since burning timescales can vary by more than an order of magnitude, decreasing for increasing core mass, this does not uniformly map onto time to core collapse for all progenitors (see §5.5).

In order for convectively excited waves to drive mass-loss in a SN progenitor at any given time, they must satisfy the following conditions:

$$\mathrm{L_{wave}} > \mathrm{L_{Edd}}; \qquad \text{(super-Eddington)}$$
$$t_{\mathrm{leak}} < t_\nu, t_{\mathrm{cc}}; \qquad \text{(leakage)}$$
$$t_{\mathrm{sound}},\, t_{\mathrm{heat}},\, t_{\mathrm{eddy}} < t_{\mathrm{cc}}. \qquad \text{(outflow)}$$

Since the spectrum of wave excitation declines steeply above $\sim 3\,\omega_c$ (Lecoanet & Quataert 2013), we focus on examining the above conditions for waves with $\omega = 3\,\omega_c$ throughout each burning phase. For each of the core burning phases, the characteristic $\ell \sim r_{\mathrm{prop}}/H \lesssim 2$, so we focus on waves with $\ell \sim 1$ since these likely carry much of the excited wave luminosity and are the most likely to satisfy the leakage condition (see eqn. 5.3).

Each of the following subsections presents the results of our calculations as follows. We begin by considering each of the super-Eddington, leakage, and outflow conditions in turn. If the most efficiently excited waves in a given progenitor fail either of the first two conditions, there is unlikely to be any significant energy transported from the core to the stellar envelope

(i.e., the excited wave energy damps to neutrinos in the core). However, if the progenitor hosts waves that satisfy the super-Eddington and leakage conditions but fail the outflow conditions, there is still a possibility that the energy carried out to the envelope could affect the envelope structure prior to core collapse by e.g., inflating or partially unbinding it.

For progenitors where at least the super-Eddington and leakage conditions are met, we examine the total wave energy reservoir excited during each phase. This is given by the integral of the wave luminosity over the phase of interest:

$$\mathrm{E_{wave}} = \int \mathrm{L_{wave}}\, dt. \tag{5.13}$$

While we use the above form for our calculations, it is useful to look at an approximate form of eqn. 5.13 that highlights the important contributions:

$$\mathrm{E_{wave}} \sim \mathrm{E_{nuc}} \left(\frac{\mathrm{L_{conv}}}{\mathrm{L_{nuc}}} \right) \mathcal{M}_{\mathrm{conv}}^{5/8}, \tag{5.14}$$

where $\mathrm{L_{nuc}}$ is the nuclear luminosity for a given burning phase, and $\mathrm{E_{nuc}}$ the total energy released through fusion during the burning phase.

We regard the determination of the wave energy reservoir as the most definitive conclusion of our work. Our arguments regarding mass loss rates and ejecta masses rely heavily on assumptions about how outflows develop in super-Eddington atmospheres (see §5.2.3), which are as yet not satisfactorily understood. However, the necessary testing, likely involving multi-dimensional hydrodynamic simulations, is beyond the scope of this work.

Finally, for progenitors where all conditions for wave-driven mass loss are met, we estimate the potential unbound mass, $\mathrm{M_{ej}}$, using eqn. 5.11. This represents an upper limit in the sense that we assume that the outflow taps into the full reservoir of wave energy to produce an outflow (it is not strictly an upper limit because of uncertainties in calculating e.g., $\mathrm{E_{wave}}$ and v_{esc}). We also calculate the radius, $\mathrm{R_{ej}}$, unbound material can reach by core collapse, given simply by $\mathrm{R_{ej}} \approx v_{\mathrm{esc}}\, t_{\mathrm{cc}}$.

Our calculations of the relevant timescales for tunneling and sound-crossing in the envelope rely on accurate determinations of the Brunt-Väisälä frequency to determine the relevant radii ($r_{\mathrm{prop}}, r_{\mathrm{in}}, r_{\mathrm{out}}$; see Fig. 5.1) and the group travel time for the excited g-modes. As the Brunt-Väisälä frequency requires numerical differentiation and depends on the implementation of mixing in the stellar interior (in that composition gradients enter into the Brunt-Väisälä frequency), our results are affected by numerical noise. Over the course of each burning phase, we evaluate the timescales given in the leakage and outflow conditions for at least ~ 100 timesteps for each progenitor. We consider any progenitor in which at least 50 per cent of the wave energy excited during a given phase satisfies the super-Eddington, leakage, and outflow conditions as capable of generating wave-driven mass loss throughout that phase. On the other hand, progenitors that fail this 50 per cent criterion are considered incapable of wave-driven mass loss for the given phase.

In the following, we organize our results by helium core mass (not ZAMS mass), as this is the best indicator for the time and energy-scales of the late burning phases (cf. Woosley et al. 2002).

A summary of all of our wave-driven mass loss calculations is given in Table 5.2. We present a detailed discussion of each of the advanced burning phases in the sections that follow.

5.4.1 Carbon-burning

Carbon burning is the least interesting of the advanced burning phases from the perspective of wave excitation and subsequent wave-driven mass loss. The nuclear luminosity is generally only slightly larger than the Eddington luminosity and the characteristic mach numbers are the smallest of the post-He burning phases. Furthermore, only progenitors that produce the smallest helium cores (which includes some of the high ZAMS mass progenitors simulated with high mass loss rates) experience convective core carbon burning. The exact helium core mass cutoff depends on the physics implemented in the stellar evolution code, especially the choice of $^{12}\mathrm{C}(\alpha,\gamma)^{16}\mathrm{O}$ reaction rate and the mixing parameters. For large helium core masses, the carbon abundance after helium burning is not large enough for the carbon burning luminosity to exceed the neutrino losses in the core, and carbon is burned radiatively (see e.g., Woosley et al. 2002).

For our `MESA star` calculations, employing the Kunz et al. (2002) $^{12}\mathrm{C}(\alpha,\gamma)^{16}\mathrm{O}$ rate, convective core carbon burning occurs only for He-core masses below about 9 $\mathrm{M}_\odot$ for non-rotating progenitors. A few of the rotating progenitors with larger helium cores experience convective core carbon burning due to the combination of rotationally enhanced mixing and mass loss; a detailed exploration of this is beyond the scope of this work. Independent of mass, carbon does burn convectively in a shell after being exhausted in the core; lower core mass progenitors have multiple distinct shell burning phases separated in time (see e.g., Fig. 5.2).

While core carbon burning excites $\lesssim 10^{46}$ erg of wave energy over the course of the burning phase, none of the progenitors produce a super-Eddington wave luminosity during this phase of evolution. Fig. 5.5 shows propagation diagrams and luminosity plots for three core carbon-burning models, one of each of our progenitor classes. For each set of plots, from left to right, the upper and lower panels are analogous to figs. 4.1 and 4.2 from Chapter 4, respectively. The top panel shows the Brunt-Väisälä frequency (solid blue line), Lamb frequencies for $\ell = 1$ and 3 (green, solid and dashed lines, respectively) and the range of propagating g-mode frequencies (given by $\sim 3\,\omega_c$) predominantly excited during the core carbon-burning phase (red, shaded span) plotted against the left axis; the convective mach number is plotted against the right axis as the dashed grey line. A range of g-mode frequencies is shown to capture variation during the burning phase.

The bottom panels show the local luminosities important in the physics of wave excitation and damping: the radiative luminosity ($\mathrm{L_{rad}}$) is shown as the solid red line; the neutrino

luminosity (L_ν) in solid black; convective luminosity (L_{conv}) in solid magenta; the maximum possible convective luminosity ($L_{max,\,conv}$) in dashed magenta; the damping luminosity for radiation (L_{damp}) in dashed teal; and the range of L_{wave} excited during this phase as the blue, shaded span. All progenitors that undergo convective core carbon burning are qualitatively similar, in that $L_{wave} < L_{Edd}$ throughout the phase. Thus, wave-driven mass loss is unlikely to arise from core carbon burning.

5.4.2 Neon burning

As for core carbon burning, only lower mass models (helium core masses $\lesssim 16\,M_\odot$ in this case) have a distinct convective core neon burning phase. This is shown in Fig. 5.2 as the short core convection phase just after the growth of the carbon depleted core ($\log t_{cc} \sim 0.75$) and similarly in Fig. 5.4 ($\log t_{cc} \sim 0$). Also similar to core carbon burning, the mass fraction in Ne left behind by the prior phase decreases with core mass, so that the net nuclear luminosity, and thus the wave luminosity, decreases with increasing core mass. Thus, only 43 of our 76 progenitors have distinct core neon burning phases.

All neon burning RSG and BSG progenitors excite gravity waves that meet the leakage condition, but only models with helium core masses $\lesssim 14\,M_\odot$ generate a super-Eddington wave luminosity during core neon burning. For the compact WR progenitors, core-Ne burning predominantly excites waves with frequencies $\lesssim \omega_{ac}$ in the stellar envelope, which are thus unlikely to tunnel out of the stellar core. This leaves 27 of the 43 core neon burning progenitors where waves are likely to transport energy out of the core and into the stellar envelope.

Figure 5.6 shows the propagation diagrams and luminosity plots as in Fig. 5.5, but with $\log P$ on the abscissa rather than $\log r$, in order to show the envelope behavior. The top right panel showing the propagation diagram for the WR progenitor also shows the acoustic cutoff frequency, ω_{ac}, in the envelope (dashed, cyan line) to demonstrate its magnitude in comparison to the excited g-mode frequencies. That $\omega \lesssim \omega_{ac}$ is also reflected in the bottom right panel where $L_{damp} < L_{max,\,conv}$ at all radii; this is equivalent to $kH < 1$ (see eqns. 5.6 and 5.7). This representative example demonstrates that convectively excited waves in WR progenitors during core neon burning are likely reflected before reaching the envelope. For the giant progenitors, $\omega_{ac} \ll \omega$ for the excited g-modes and roughly follows the Lamb frequency (so it is not shown). In giants that satisfy the super-Eddington and leakage conditions, waves likely tunnel out of the core and deposit their energy at r_{damp}.

The upper panels of Fig. 5.7 show the total energy released in waves during core neon burning for all progenitors that satisfy the super-Eddington and leakage conditions. In the upper left panel, the integral in eqn. 5.13, evaluated from the start of the burning phase to a given t_{cc}, is plotted every $\log t_{cc} \sim 0.05$. The total (cumulative) energy liberated over the whole burning phase for each model is shown as a horizontal line in the upper right panel. The colors represent the helium core mass, according to the colorbar at the far right of the plot, and the symbols represent the progenitor type, with circles representing RSGs, squares

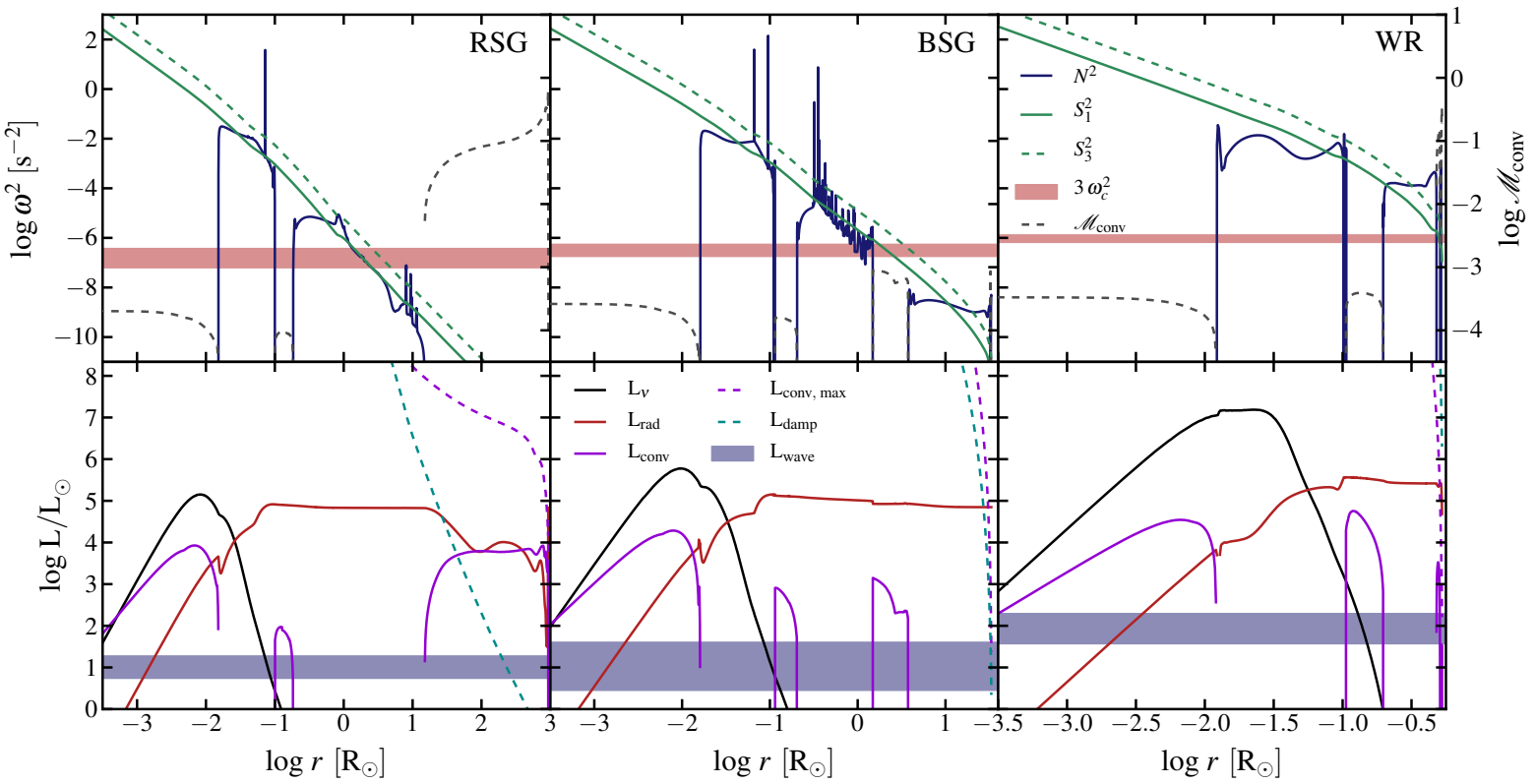

Figure 5.5: Propagation diagrams and luminosity plots for example core carbon burning models from each progenitor class. Top panels show propagation diagrams, where the colors and dashes are as described for fig. 5.1 but with the range of propagating g-mode frequencies excited during the whole burning phase shown by the red span. The lower panels show the relevant local luminosities as in the bottom panel of fig. 5.1 but with the range of wave luminosities excited throughout the burning phase shown as the blue span. These lower panels demonstrate that $L_{\rm wave} < L_{\rm rad} \sim L_{\rm Edd}$ during core carbon burning. The red supergiant shown is a 12 $M_\odot$ solar metallicity model, the blue supergiant a 15 $M_\odot$ zero metallicity model, and the Wolf-Rayet a 80 $M_\odot$ solar metallicity model with high mass loss.

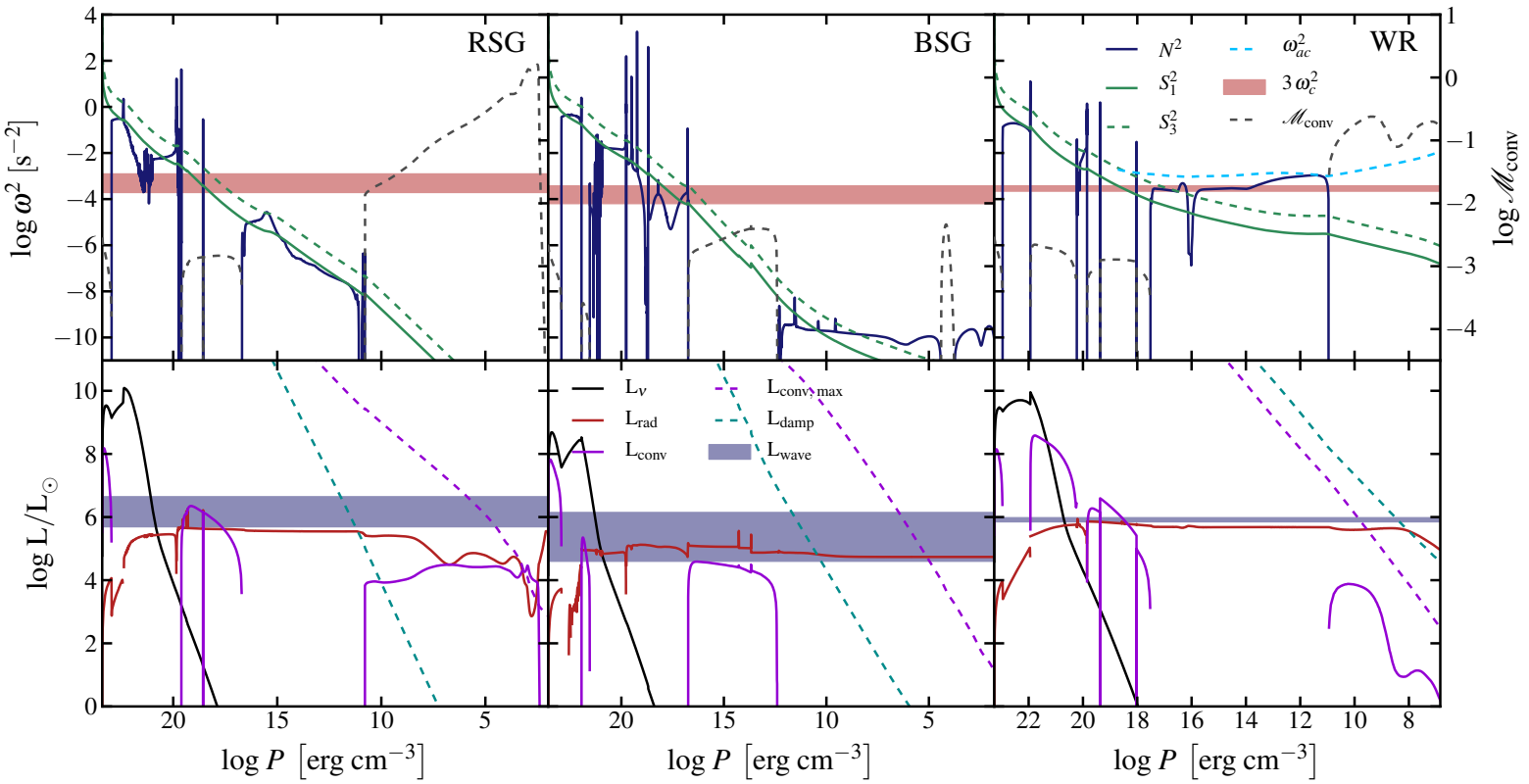

Figure 5.6: Propagation diagrams and luminosity plots for example core neon burning models from each progenitor class. The colors and dashes are as described for fig. 5.5, with the addition of the acoustic cutoff frequency (ω_{ac}) in the envelope shown as the dashed cyan line in the top right panel for the Wolf-Rayet progenitor. This is plotted to show that the g-mode frequencies are below the acoustic cutoff for this representative compact progenitor, and thus waves are likely reflected before reaching the envelope. For the red/blue supergiant progenitors, ω_{ac} roughly follows the Lamb frequency and is never larger than the g-mode frequencies. The red supergiant shown is a 25 $M_\odot$ solar metallicity model, the blue supergiant a 15 $M_\odot$ zero metallicity model, and the Wolf-Rayet a 40 $M_\odot$ solar metallicity model.

BSGs, and triangles WRs. There are no strong trends in E_{wave} during core neon burning.

For all progenitors that satisfy the super-Eddington and leakage conditions (giants), waves reach r_{damp} interior to r_{ss}, on a timescale $t_{sound} \sim 10^4\,s \ll t_{cc}$ (since $r_{damp} \ll R_\star$). For three of the RSGs and one BSG, r_{damp} is within one scale height of the envelope convection zone; we consider the timescale for driving an outflow from these few progenitors to be $t_{eddy} \ll t_{cc}$. However, the majority, 23, reach r_{damp} in the radiative zone ~ 10 scale heights from the outer convection zone and must heat the stellar material to drive convection and eventually an outflow. Calculating t_{heat} over the region from r_{damp} to the base of the envelope convection zone $r_{env,\,cz}$, we find 12 of the remaining 23 have $t_{heat} < t_{cc}$, leading to the conclusion that wave-driven mass loss is plausible in these 12 progenitors. The remaining 11 likely reach collapse with $\sim 10^{46}$ erg of wave energy still attempting to work its way through the envelope.

The upper panel of Fig. 5.8 shows our estimate of M_{ej} (see eqn. 5.11) for the 16 progenitors (out of 43 core-Ne burning and 76 total progenitors) where wave-driven mass loss is likely during core neon burning. Our RSG progenitors, having the most weakly bound envelopes, are capable of producing the largest wave-driven mass loss events, with $M_{ej} \sim 0.1 - 1\,M_\odot$. BSGs can produce $M_{ej} \lesssim 0.04\,M_\odot$ and WRs $\lesssim 0.01\,M_\odot$. If launched during core-Ne fusion, traveling at the escape velocity at r_{damp}, $\sim 100\,s\,km\,s^{-1}$, this ejecta can reach distances of $\lesssim 300\,AU$ prior to core collapse. Lower mass progenitors, with their smaller helium cores, longer burning timescales, and tendency to form giants, are capable of producing the most massive and extended wave-driven circumstellar environments.

5.4.3 Oxygen burning

Core oxygen burning is convective for all progenitors, but occurs over a range of timescales (see Table 5.1, and Woosley et al. 2002); the burning timescale depends primarily on helium core mass, with the smallest cores ($\sim 3\,M_\odot$) having core oxygen burning for $\sim 6\,yr$ and the largest ($\sim 40\,M_\odot$) for $\sim 10\,day$. For all the progenitors considered here, the burning produces a super-Eddington wave luminosity during the majority of the core oxygen burning phase.

In all but five of the 42 RSG and BSG progenitors, convectively excited waves can transport energy from the core to the envelope. As expected from eqn. 5.3, those that fail are biased towards larger values of r_{out}/r_{in}. For the WRs, only three out of 34 compact progenitors have waves with frequencies above the envelope acoustic cutoff during core oxygen burning. This leaves a total of 40 (37 giants and 3 WRs), a little more than half of the progenitors, capable of transporting wave energy from the core to the envelope during core oxygen burning.

The middle panel of Fig. 5.7 shows the wave energy reservoir during core oxygen burning for these 40 progenitors, while the bottom panel shows the wave energy from shell oxygen burning. There is a factor of 50 increase in the wave energy reservoir from core oxygen burning as the helium core mass increases from $\sim 3.2 - 39\,M_\odot$. This increase arises partially

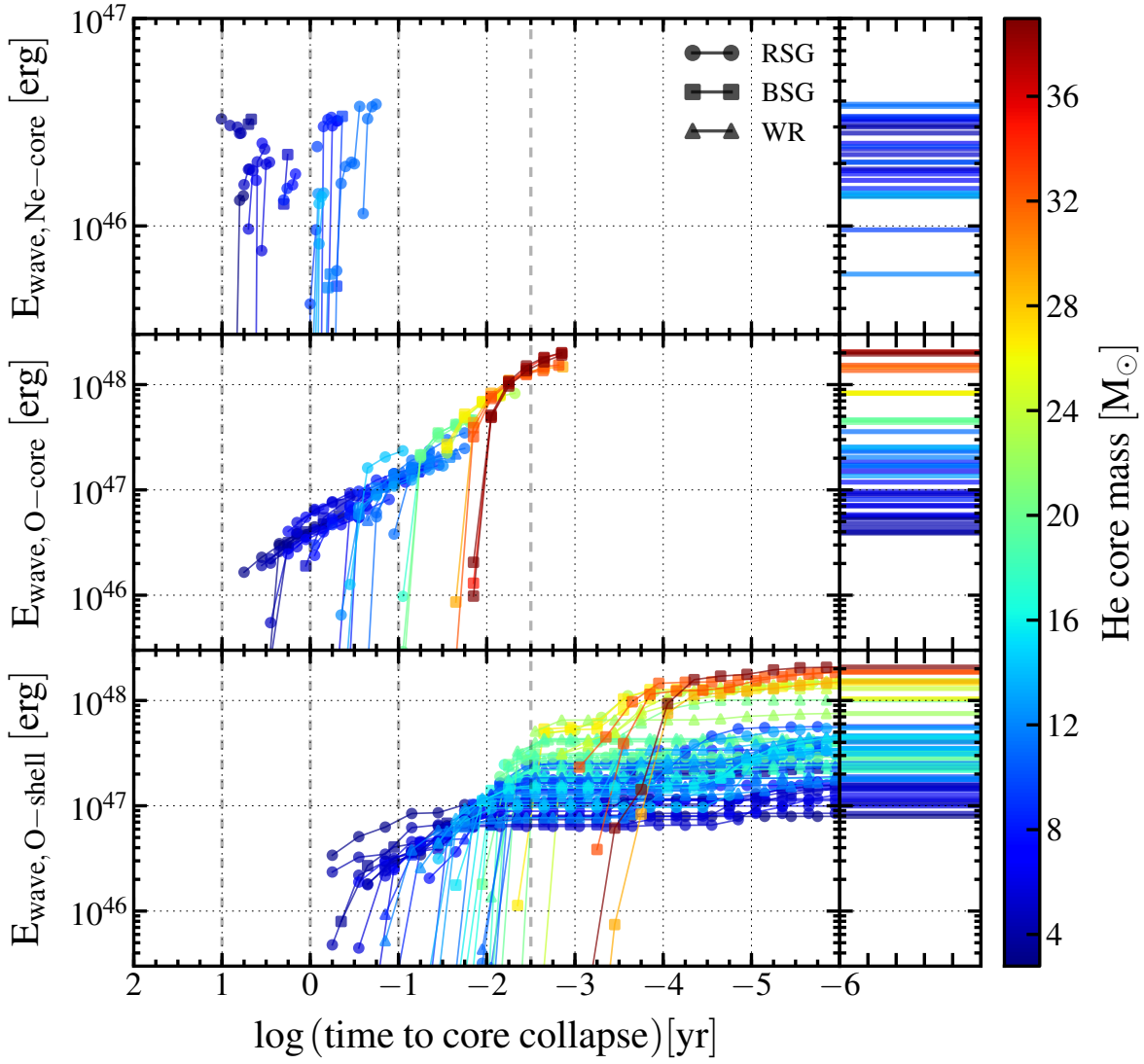

Figure 5.7: Wave energy excited (see eqn. 5.14) during core-Ne and O burning (top and middle left panels, respectively) and shell-O burning (bottom left panel) for each of the progenitors that satisfies the super-Eddington and leakage conditions, plotted against time to core collapse. Colors correspond to helium core mass, as given by the color bar at right. The integrated energy, from the beginning of the burning phase up to a given t_{cc}, is plotted every 0.05 dex in $\log t_{cc}$ in the top panel, 0.2 dex in the middle panel, and 0.3 dex in the bottom panel. The top right panels give the total (cumulative) wave energy excited over the entirety of each core burning phase. The bottom right gives the total energy excited over the shell burning phase (or the total at $\log t_{cc} \sim -6$, whichever occurs first). The shape of the points correspond to progenitor type as noted in the legend in the top panel. These plots demonstrate the near one-to-one correspondence between helium core mass and available wave energy, as explained further in the text.

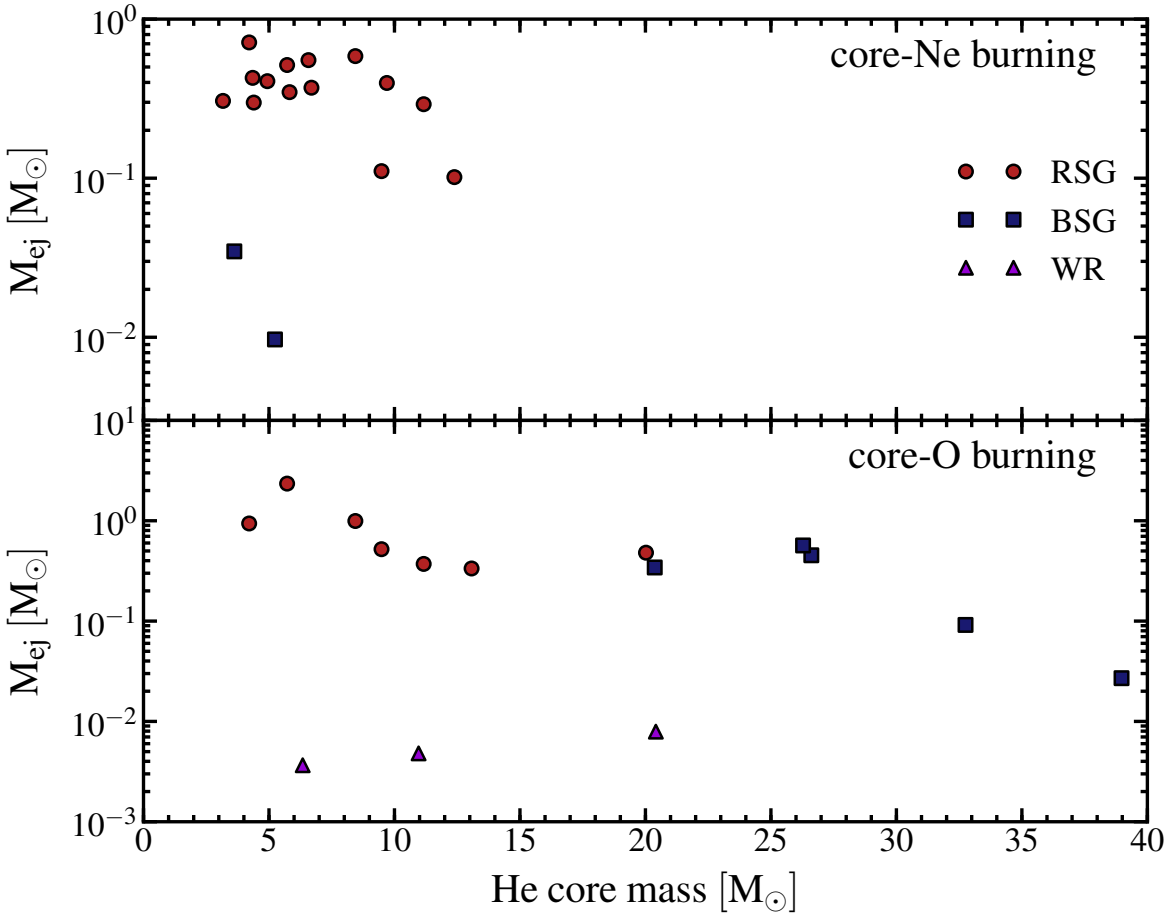

Figure 5.8: Potential mass unbound by waves generated during core neon (upper panel) and oxygen burning (lower panel), estimated using eqn. 5.11. The colors and symbols represent progenitor types as noted in the legend. Note the clear delineation of M_{ej} between giants and Wolf-Rayets, due to differences in the envelope binding energy (hydrogen for the giants and helium for the Wolf-Rayets).

from each of the contributions outlined in eqn. 5.14. As core mass increases, the time averaged mach number during the oxygen core burning increases by a factor of ~ 20, the total nuclear energy liberated varies by a factor of ~ 5, and the ratio of the convective to nuclear luminosities varies by a factor of ~ 2. While the ratio L_{conv}/L_{nuc} varies only slightly, the ratio L_{wave}/L_{Edd} varies from $\sim 1 - 10^3$ due to the change in burning timescale and thus L_{nuc}.

During the short core oxygen burning phase, fewer progenitors host waves capable of heating the stellar envelope on a timescale shorter than the time to core collapse. Only four of the 40 progenitors with waves capable of transporting a super-Eddington luminosity to the envelope have $t_{heat} < t_{cc}$ and can drive outflows via radiatively damped waves. Another four excite waves that reach $r_{ss} < r_{damp}$, but have $kH > 1$, so that they can drive an outflow on $\sim$ the sound crossing time at r_{ss}, which is characteristically on the order of minutes. Finally, seven giants have waves with r_{damp} less than one scale height from the envelope convection zone; for these, we assume the deposited wave energy can immediately drive convection into the envelope zone and drive an outflow on a timescale $t_{eddy} \lesssim$ day $< t_{cc}$. In total, 15 of our 76 progenitors are capable of generating wave-driven mass loss during the core oxygen burning phase; these 15 span all three progenitor categories.

The lower panel of Fig. 5.8 shows our estimate of M_{ej} for the 15 progenitors capable of wave-driven mass loss during core oxygen burning, as described above for Ne-burning. As during core-Ne burning, the weakly bound envelopes of the giant progenitors are most susceptible to large mass-loss events. During core-O burning, RSGs may produce $M_{ej} \sim 0.3 - 3\,M_\odot$, BSGs may liberate $M_{ej} \lesssim 1\,M_\odot$, and WRs $\lesssim 0.01\,M_\odot$. Given the similar timescales and assumed envelope structures for oxygen and neon fusion, the outflow velocities and the radii reached by the ejecta during core-O burning are similar to those during Ne burning, with ejecta reaching $\lesssim 300$ AU at speeds of 100s km s^{-1}. For the more massive giants with both core-Ne and O convective burning phases, the energy liberated during core oxygen fusion may be an order of magnitude larger, but it is unable to escape the star due to the shorter time to core collapse.

5.4.4 Silicon burning

The silicon burning phase is the most uncertain of those considered here. During this late stage, burning and convective timescales become comparable, likely invalidating the treatment used in most stellar evolution codes, including `MESA star` (e.g., Woosley et al. 2002). Furthermore, the reaction network uses many pseudo-reactions to simulate the actual high-dimensional nucleosynthetic network (though development is underway to improve upon this; Paxton, *private communication*). These uncertainties may affect the luminosities and stellar structure during silicon burning, so we regard the following results as tentative.

In our `MESA star` models, silicon burns convectively in the core for all progenitors, over timescales of $\lesssim 5$ day for the smallest cores down to ~ 6 hr for the largest. The most luminous burning phase, core silicon burning produces a significantly super-Eddington

wave luminosity in all progenitors, $L_{wave} \sim 10^2 - 10^4 L_{Edd}$. The characteristic excitation frequency, $\sim 3\,\omega_c$, increases from $\sim 10^{-3}$ Hz during carbon burning to ~ 0.1 Hz during this last phase. At these high frequencies, convectively excited waves now exceed the acoustic cutoff frequency in all compact progenitors.

With the compact progenitors exciting waves above the acoustic cutoff frequency, many more progenitors transport energy from the core to the surface during core silicon burning than during the previous phases: 70 of 76. Figure 5.9 shows the wave energy reservoir for these 70 progenitors during core silicon burning. There is a roughly monotonic relationship between E_{wave} and helium core mass, as in the case of core oxygen burning, but the range in E_{wave} is smaller at a factor of ~ 8.

Thirty-seven of the seventy progenitors that satisfy the super-Eddington and leakage conditions also satisfy the outflow conditions. Of these, the majority, 29, are WR progenitors which now host convectively excited waves with frequencies above the acoustic cutoff, as described above. In these, waves reach r_{ss} before r_{damp}, likely generating outflows on the sound crossing time at r_{ss}, which is $\lesssim$ minute. Only one of the RSG progenitors has waves that damp in the envelope convection zone, while the remaining seven have $t_{heat}, t_{eddy} < t_{cc}$. This latter group arises due to the several order of magnitude increase in L_{wave}, which brings the sonic point, r_{ss}, deeper into the envelope in addition to simply increasing the energy deposition rate.

Figure 5.10 shows the mass, M_{ej}, that can be unbound by waves excited during core-Si burning. As during previous phases, there is a clear delineation in M_{ej} between giants and WRs due to differences in the envelope binding energy. While several of the RSGs are capable of heating the stellar material and potentially driving an outflow prior to core collapse, there is not enough time for any unbound mass to travel beyond the progenitor photosphere, which is already $\gtrsim 100\,R_\odot$. However, for the WR progenitors, wave energy driven to the envelope during Si burning has the potential to inflate these compact progenitors to giants extending out to $100s\,R_\odot$, in the $\sim$ day leading up to collapse. This may have important implications for the appearance of a subsequent supernovae.

5.5 Discussion and conclusions

In this Chapter, we have surveyed supernova progenitors covering a decade in initial mass, metallicities from 0 (Population III) to solar and rotation up to 80 per cent of breakup in search of those susceptible to the wave-driven mass loss mechanism we proposed in Chapter 4 and QS12. We believe this grid of evolutionary sequences provides a good sample of the range of possible helium core masses and mass loss histories for single star core collapse SN progenitors. For the majority of progenitors, waves excited by vigorous core convection after core carbon exhaustion can carry a super-Eddington luminosity out to stellar envelope and deposit $10^{46} - 10^{48}$ erg. Depending on the uncertain physics of super-Eddington stellar envelopes, this may lead to strong wave-driven mass loss in about 20 per cent of the progenitors surveyed. While a detailed comparison to supernova rates

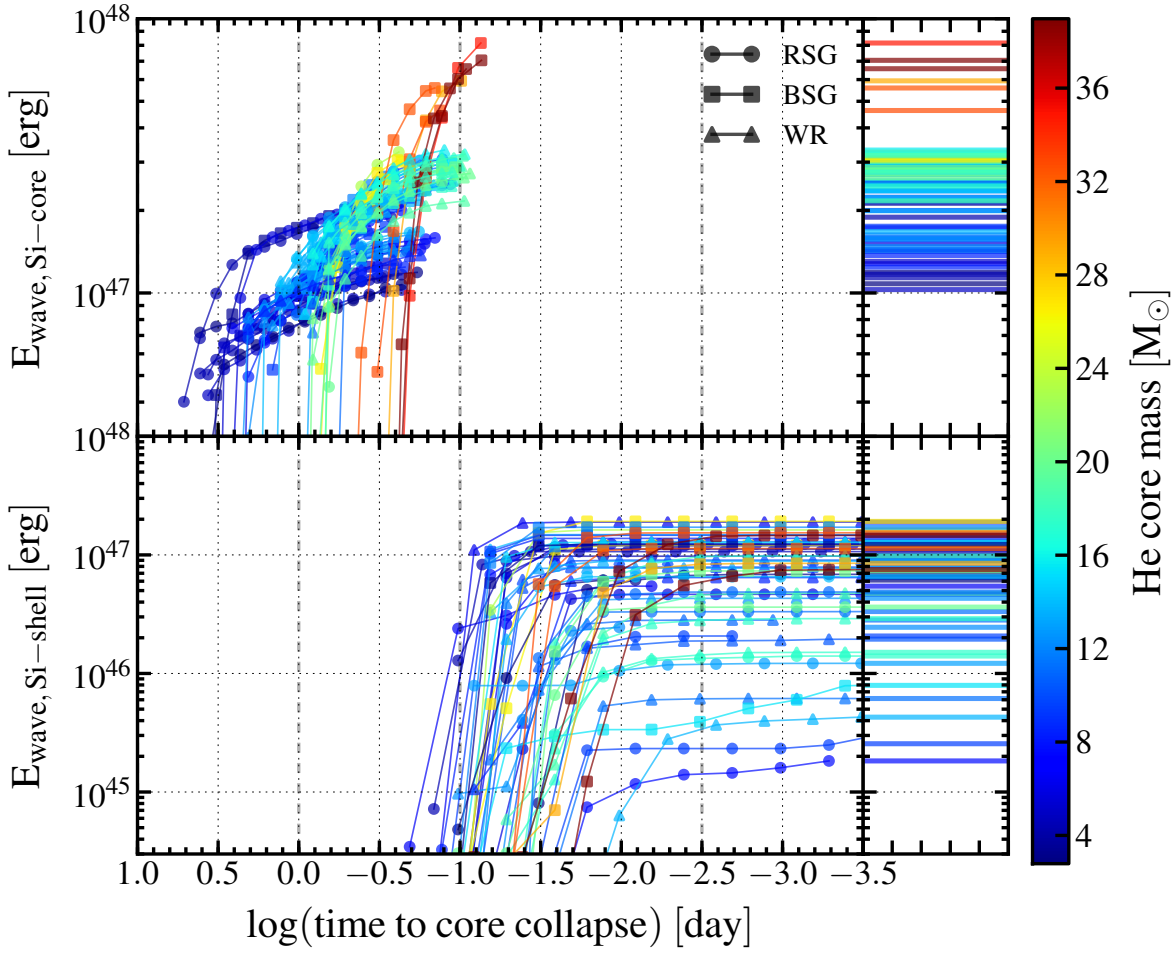

Figure 5.9: Wave energy excited (see eqn. 5.14) during core (top left panel) and shell silicon burning (bottom left panel) for each of the progenitors that satisfies the super-Eddington and leakage conditions, plotted against time to core collapse *in days*. The top right panel gives the total (cumulative) wave energy excited over the whole core-Si burning phase, while the bottom right gives the total energy excited during shell-Si burning (or the total at $\log(t_{cc}/\mathrm{day}) \sim -3.5$, whichever occurs first). Colors and symbols are as described for Fig. 5.7.

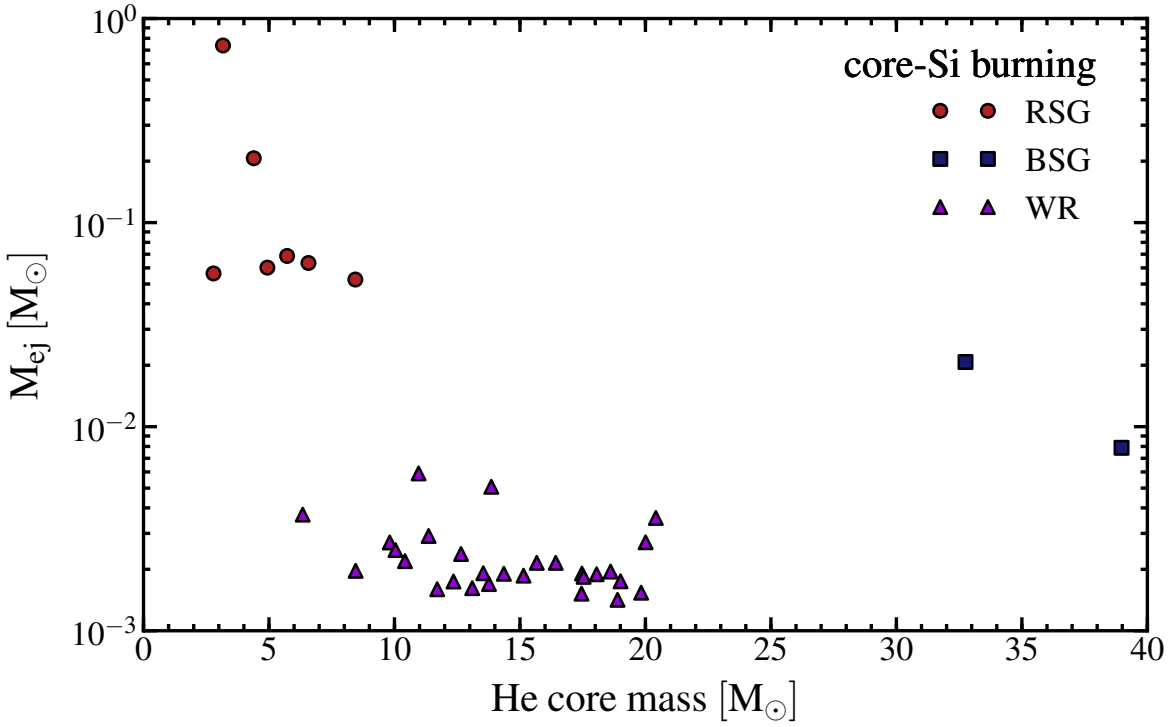

Figure 5.10: Potential mass unbound by waves generated during core-Si burning. Colors and symbols are as in fig. 5.8. As for the earlier burning phases, there is a clear delineation in M_{ej} by progenitor type due to differences in the envelope binding energy. For the giant progenitors, there is not enough time before core collapse for the wave-energy deposition to eject material beyond the stellar radius. Instead, wave energy will significantly restructure the stellar envelope prior to explosion.

depends on the initial mass function, the connection between ZAMS and helium core masses, and the subset of massive stars that can explode, we note that the rate of wave-driven mass loss we find is comparable to the rate of Type IIn SNe, which are ~ 10 per cent of core collapse SNe (Li et al. 2011). Progenitors with small helium cores are susceptible to early mass loss events, up to $\sim 10\,\mathrm{yr}$ prior to core collapse, and giants with weakly bound envelopes produce the largest events, potentially ejecting multiple solar masses of material out to $\sim 100\mathrm{s}\,\mathrm{AU}$. At silicon burning, this process can inflate compact Wolf-Rayet like progenitors (without hydrogen envelopes) to giants with helium envelopes that extend to $\sim 100\mathrm{s}\,\mathrm{R}_\odot$.

Table 5.2 summarizes the results of our calculations (see also Figs. 5.7—5.11). For each model, the time to core collapse (t_{cc}) for each of the neon, oxygen and silicon burning phases is given whenever these phases occur convectively. The wave energy reservoir ($\mathrm{E}_{\mathrm{wave}}$) for each burning phase is given for models in which convectively excited waves can tunnel out of the core and carry a super-Eddington luminosity into the envelope. Finally, when this excited wave energy can plausibly drive an outflow on a timescale shorter than t_{cc}, we present the potential ejecta mass (M_{ej}) and the radius that ejecta reaches prior to explosion (R_{ej}). Our results demonstrate that the lowest core mass progenitors are most likely to produce massive, $\sim \mathrm{M}_\odot$, extended, $\lesssim 300\,\mathrm{AU}$, circumstellar environments. While compact WR progenitors are less likely to generate a massive circumstellar medium, wave excitation and damping during Si burning can inflate WR progenitors to giant radii ($\sim 100\mathrm{s}\,\mathrm{R}_\odot$).

Given that the wave luminosity excited by core carbon fusion is never super-Eddington, the earliest core burning phase that might lead to wave-driven mass loss is neon fusion. For the lowest core masses, the onset of super-Eddington wave luminosities may be as early as $\sim 10\,\mathrm{yr}$ before core collapse. Figure 5.11 shows the earliest potential onset of wave-driven mass loss (t_{onset}) as a function of helium core mass. This highlights the well known (e.g., Woosley et al. 2002) correspondence between burning duration and core mass, which is one of the key features of our specific mass loss mechanism. For wave-driven mass loss events, the timing of a pre-SN outburst can be used to place an upper limit on the helium core mass of the progenitor, which can in turn be constrained by modeling the associated SN. For example, an event that occurs more than a month prior to core collapse requires a progenitor with a helium core mass $\lesssim 15\,\mathrm{M}_\odot$. The complex interplay between mixing and mass loss, each dependent on both rotation and metallicity, makes the further inference from helium core mass to ZAMS mass, metallicity and rotation much more uncertain.

5.6 Directions for future work

In this work, we have outlined how wave energy, transported from the core and deposited in the stellar envelope, could lead to large outflows in a subset of SN progenitors within ~ 10 years of core collapse. The conditions we have investigated are necessary for wave-driven mass loss, but it is as yet unclear if they are sufficient. Further (likely hydrodynamic) calculations are necessary to investigate both the excitation and damping of waves in SN

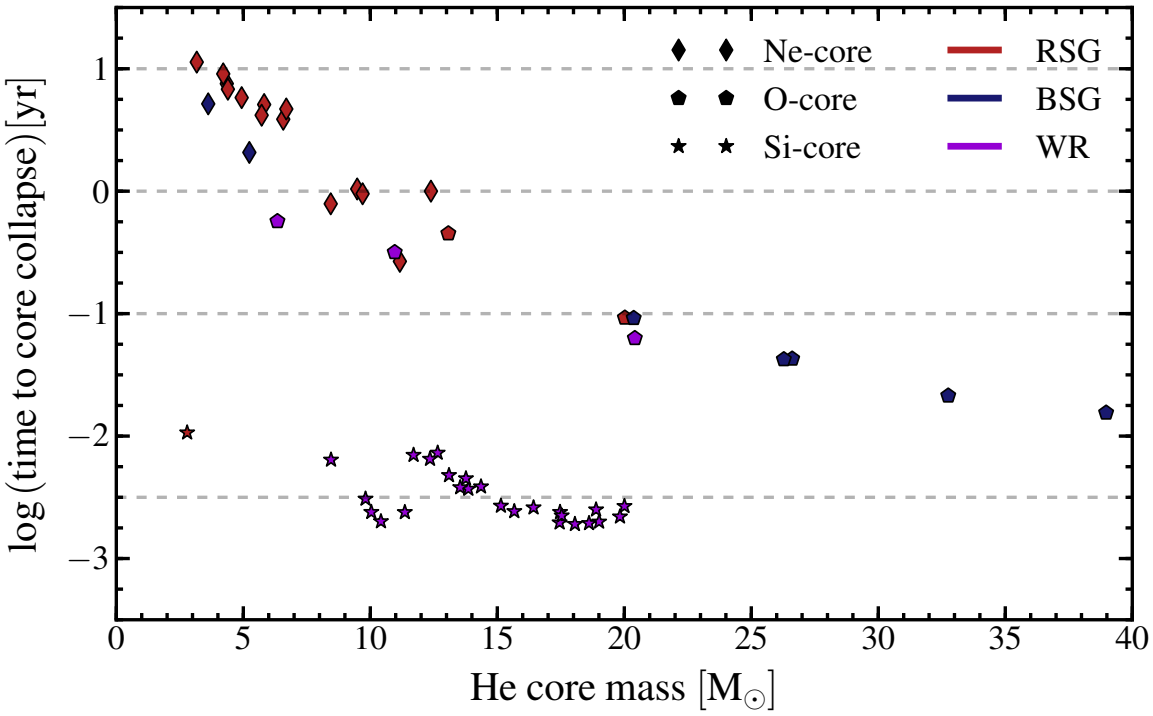

Figure 5.11: Earliest potential onset of wave-driven mass loss for SN progenitors, plotted as a function of helium core mass. Symbols denote the phase of burning corresponding to the earliest potential onset, with diamonds for Ne-core burning, pentagons for O-core, and stars for Si-core. Colors represent progenitor type as in previous figures. Grey dashed lines mark 10 years, 1 year, 1 month, and 1 day prior to core collapse (from top to bottom). Note the correspondence between $t_{\rm onset}$ and $\rm M_{He}$, with lower core masses producing wave-driven mass loss earlier in evolution.

Table 5.2: Wave-driven mass loss results

					core Ne burning					core O burning					core Si burning				
M_{ZAMS}	Z_{init}	Ω/Ω_{crit}	Mass Loss	Class	t^*_{cc}	$E_{w,46}$ †	M_{ej} ‡	$v^‡_{esc}$	R_{ej} ‡	t^*_{cc}	$E_{w,46}$ †	M_{ej} ‡	$v^‡_{esc}$	R_{ej} ‡	t^*_{cc}	$E_{w,46}$ †	M_{ej} ‡	$v^‡_{esc}$	R_{ej} ‡
$[M_\odot]$	$[Z_\odot]$				[yr]	[erg]	$[M_\odot]$	[km/s]	[AU]	[yr]	[erg]	$[M_\odot]$	[km/s]	[AU]	[day]	[erg]	$[M_\odot]$	[km/s]	$[R_\odot]$
12	0	0.00	0.8 (v+dj)	RSG	11.41	3.3	0.31	103	249.8	6.27	3.9	–	–	–	5.06	11.9	0.74	127	80.0
12	10^{-2}	0.00	0.8 (v+dj)	RSG	6.89	2.8	0.30	97	141.2	4.38	4.8	–	–	–	3.87	11.7	0.21	238	114.7
12	10^{-1}	0.00	0.8 (v+dj)	RSG	7.65	3.0	0.43	83	135.4	4.43	4.3	–	–	–	4.74	11.4	–	–	–
12	1.0	0.00	0.8 (v+dj)	RSG	9.16	3.0	0.71	65	126.7	5.23	4.0	0.94	65	72.0	5.85	18.9	–	–	–
12	1.0	0.20	0.6 (v+dj)	RSG	6.13	1.9	0.41	68	88.1	2.94	5.3	–	–	–	3.98	10.3	$6.0\ 10^{-2}$	414	204.8
12	1.0	0.50	0.6 (v+dj)	RSG	9.23	1.4	–	–	–	3.72	5.5	–	–	–	3.90	10.8	$5.6\ 10^{-2}$	439	212.4
12	1.0	0.80	0.6 (v+dj)	RSG	3.90	2.5	0.55	67	55.6	2.72	7.1	–	–	–	3.00	12.8	$6.3\ 10^{-2}$	450	167.6
15	0	0.00	0.8 (v+dj)	BSG	5.19	3.3	$3.5\ 10^{-2}$	307	336.9	3.13	5.7	–	–	–	5.17	21.2	–	–	–
15	10^{-2}	0.00	0.8 (v+dj)	RSG	3.83	2.0	–	–	–	2.00	7.0	–	–	–	2.63	15.1	–	–	–
15	10^{-1}	0.00	0.8 (v+dj)	RSG	5.16	1.8	0.35	73	79.5	2.16	9.2	–	–	–	2.36	14.2	–	–	–
15	1.0	0.00	0.8 (v+dj)	RSG	4.51	2.3	0.51	67	64.5	2.10	9.7	2.35	64	28.5	2.99	21.5	$6.9\ 10^{-2}$	561	208.4
15	1.0	0.50	0.6 (v+dj)	RSG	4.90	1.7	0.37	67	69.3	2.53	5.8	–	–	–	2.28	14.4	–	–	–
15	1.0	0.80	0.6 (v+dj)	RSG	1.15	1.0	0.11	93	22.6	0.56	17.2	0.52	182	21.6	1.00	30.7	–	–	–
20	0	0.00	0.8 (v+dj)	BSG	2.10	2.2	$9.7\ 10^{-3}$	478	212.0	1.20	8.9	–	–	–	3.73	13.0	–	–	–
20	10^{-2}	0.00	0.8 (v+dj)	RSG	0.65	3.2	–	–	–	0.44	16.4	–	–	–	1.35	20.0	–	–	–
20	10^{-1}	0.00	0.8 (v+dj)	RSG	2.24	1.5	–	–	–	1.35	8.1	–	–	–	2.47	12.4	–	–	–
20	1.0	0.00	0.8 (v+dj)	RSG	0.81	3.3	0.59	75	12.9	0.47	18.5	0.99	136	13.5	1.14	22.3	$5.3\ 10^{-2}$	653	92.7
20	1.0	0.20	0.6 (v+dj)	RSG	1.75	1.8	–	–	–	0.98	11.8	–	–	–	1.75	15.9	–	–	–
20	1.0	0.50	0.6 (v+dj)	RSG	0.96	2.4	0.40	78	15.9	0.60	–	–	–	–	2.38	15.7	–	–	–
20	1.0	0.80	0.6 (v+dj)	WR	0.88	–	–	–	–	0.35	23.2	$4.8\ 10^{-3}$	2201	163.4	0.76	29.4	$5.9\ 10^{-3}$	2239	211.0
25	0	0.00	0.8 (v+dj)	BSG	0.51	3.4	–	–	–	0.31	–	–	–	–	1.53	17.5	–	–	–
25	10^{-2}	0.00	0.8 (v+dj)	RSG	0.60	2.0	–	–	–	0.31	25.5	–	–	–	0.66	28.8	–	–	–
25	10^{-1}	0.00	0.8 (v+dj)	RSG	0.34	3.8	–	–	–	0.26	23.7	–	–	–	1.10	23.7	–	–	–
25	1.0	0.00	0.8 (v+dj)	RSG	0.27	3.9	0.29	115	6.6	0.17	35.8	0.37	311	11.1	0.74	24.9	–	–	–
25	1.0	0.20	0.6 (v+dj)	RSG	1.06	1.4	0.10	118	26.7	0.48	16.9	–	–	–	1.00	30.4	–	–	–
25	1.0	0.50	0.6 (v+dj)	RSG	0.90	1.4	–	–	–	0.46	13.6	0.33	201	19.6	1.05	28.6	–	–	–
25	1.0	0.80	0.6 (v+dj)	WR	0.99	–	–	–	–	0.33	–	–	–	–	0.87	25.6	$2.9\ 10^{-3}$	2974	321.9
30	0	0.00	0.8 (v+dj)	BSG	0.77	0.6	–	–	–	0.41	20.5	–	–	–	0.99	27.0	–	–	–
30	10^{-2}	0.00	0.8 (v+dj)	RSG	0.96	1.4	–	–	–	0.52	–	–	–	–	2.08	16.7	–	–	–
30	10^{-1}	0.00	0.8 (v+dj)	RSG	0.71	–	–	–	–	0.39	25.3	–	–	–	1.18	25.1	–	–	–
30	1.0	0.00	0.8 (v+dj)	WR	0.73	–	–	–	–	0.39	–	–	–	–	1.35	19.9	$5.1\ 10^{-3}$	1987	333.7
30	1.0	0.20	0.6 (v+dj)	BSG	0.33	–	–	–	–	0.19	–	–	–	–	1.01	29.8	–	–	–
30	1.0	0.50	0.6 (v+dj)	BSG	–	–	–	–	–	0.16	–	–	–	–	0.86	28.2	–	–	–
30	1.0	0.80	0.6 (v+dj)	WR	1.32	–	–	–	–	0.67	–	–	–	–	2.66	14.8	$2.4\ 10^{-3}$	2498	825.9
40	0	0.00	0.8 (v+dj)	RSG	–	–	–	–	–	0.10	46.1	–	–	–	0.78	25.5	–	–	–
40	10^{-2}	0.00	0.8 (v+dj)	RSG	–	–	–	–	–	0.09	43.6	0.48	302	5.9	0.68	28.0	–	–	–
40	10^{-1}	0.00	0.8 (v+dj)	BSG	–	–	–	–	–	0.09	46.1	0.34	368	7.1	0.71	28.7	–	–	–
40	1.0	0.00	v+n	WR	0.34	–	–	–	–	0.18	–	–	–	–	0.87	25.1	$2.5\ 10^{-3}$	3185	345.5
40	1.0	0.00	0.8 (v+dj)	WR	0.73	–	–	–	–	0.37	–	–	–	–	1.75	15.7	$1.6\ 10^{-3}$	3126	678.3
40	1.0	0.20	0.6 (v+dj)	WR	–	–	–	–	–	0.06	64.7	$7.9\ 10^{-3}$	2868	38.1	1.03	30.2	$3.6\ 10^{-3}$	2914	373.0
40	1.0	0.50	0.6 (v+dj)	WR	–	–	–	–	–	0.06	–	–	–	–	0.98	27.3	$2.7\ 10^{-3}$	3177	385.2
40	1.0	0.80	0.6 (v+dj)	WR	0.59	–	–	–	–	0.30	–	–	–	–	1.64	21.8	$1.7\ 10^{-3}$	3598	734.5
50	0	0.00	0.8 (v+dj)	RSG	–	–	–	–	–	0.04	82.6	–	–	–	0.86	32.7	–	–	–
50	10^{-2}	0.00	0.8 (v+dj)	BSG	–	–	–	–	–	0.04	82.5	0.57	382	3.4	0.90	31.2	–	–	–
50	10^{-1}	0.00	0.8 (v+dj)	BSG	–	–	–	–	–	0.04	83.6	0.45	430	3.9	0.91	30.5	–	–	–
50	1.0	0.00	0.8 (v+dj)	WR	0.96	–	–	–	–	0.50	–	–	–	–	2.46	16.3	$1.7\ 10^{-3}$	3063	933.9
50	1.0	0.00	v+n	WR	0.78	–	–	–	–	0.28	–	–	–	–	0.73	25.1	$2.2\ 10^{-3}$	3395	309.2
50	1.0	0.20	0.6 (v+dj)	WR	–	–	–	–	–	0.03	–	–	–	–	0.87	–	–	–	–
50	1.0	0.50	0.6 (v+dj)	WR	–	–	–	–	–	0.04	–	–	–	–	0.83	–	–	–	–
50	1.0	0.80	0.6 (v+dj)	WR	–	–	–	–	–	0.23	–	–	–	–	1.41	24.7	$1.9\ 10^{-3}$	3614	633.4

Continued on Next Page...

Table 5.2 — Continued

					core Ne burning					core O burning					core Si burning				
M_{ZAMS} [$M_\odot$]	Z_{init} [$Z_\odot$]	Ω/Ω_{crit}	Mass Loss	Class	t^*_{cc} [yr]	$E_{w,46}$ † [erg]	M_{ej} ‡ [$M_\odot$]	$v^\ddagger_{esc}$ [km/s]	R_{ej} ‡ [AU]	t^*_{cc} [yr]	$E_{w,46}$ † [erg]	M_{ej} ‡ [$M_\odot$]	$v^\ddagger_{esc}$ [km/s]	R_{ej} ‡ [AU]	t^*_{cc} [day]	$E_{w,46}$ † [erg]	M_{ej} ‡ [$M_\odot$]	$v^\ddagger_{esc}$ [km/s]	R_{ej} ‡ [$R_\odot$]
60	0	0.00	0.8 (v+dj)	BSG	–	–	–	–	–	0.02	147.5	–	–	–	0.35	59.4	–	–	–
60	10^{-2}	0.00	0.8 (v+dj)	BSG	–	–	–	–	–	0.02	136.1	–	–	–	0.59	55.9	–	–	–
60	10^{-1}	0.00	0.8 (v+dj)	BSG	–	–	–	–	–	0.02	153.0	$9.2\ 10^{-2}$	1296	5.8	0.41	46.3	$2.1\ 10^{-2}$	1497	75.5
60	1.0	0.00	v+n	WR	1.24	–	–	–	–	0.64	–	–	–	–	2.56	14.2	$1.6\ 10^{-3}$	2989	948.9
60	1.0	0.00	0.8 (v+dj)	WR	–	–	–	–	–	0.16	–	–	–	–	0.98	23.6	$1.9\ 10^{-3}$	3567	435.3
60	1.0	0.20	0.6 (v+dj)	WR	–	–	–	–	–	0.02	–	–	–	–	0.45	–	–	–	–
60	1.0	0.50	0.6 (v+dj)	WR	–	–	–	–	–	0.04	–	–	–	–	0.68	–	–	–	–
60	1.0	0.80	0.6 (v+dj)	WR	–	–	–	–	–	0.16	–	–	–	–	0.89	33.2	$2.2\ 10^{-3}$	3939	433.8
70	0	0.00	0.8 (v+dj)	BSG	–	–	–	–	–	0.02	204.7	–	–	–	0.29	81.6	–	–	–
70	10^{-2}	0.00	0.8 (v+dj)	BSG	–	–	–	–	–	0.02	194.5	–	–	–	0.29	70.5	–	–	–
70	10^{-1}	0.00	0.8 (v+dj)	BSG	–	–	–	–	–	0.02	203.9	$2.7\ 10^{-2}$	2756	9.0	0.30	65.7	$7.9\ 10^{-3}$	2896	106.9
70	1.0	0.00	v+n	WR	0.50	–	–	–	–	0.25	–	–	–	–	1.39	22.3	$1.9\ 10^{-3}$	3423	590.9
70	1.0	0.00	0.8 (v+dj)	WR	–	–	–	–	–	0.10	–	–	–	–	0.72	24.5	$1.5\ 10^{-3}$	4026	358.7
70	1.0	0.20	0.6 (v+dj)	WR	–	–	–	–	–	0.04	–	–	–	–	1.01	–	–	–	–
70	1.0	0.50	0.6 (v+dj)	WR	–	–	–	–	–	0.03	–	–	–	–	0.43	–	–	–	–
70	1.0	0.80	0.6 (v+dj)	WR	–	–	–	–	–	0.14	–	–	–	–	0.95	32.0	$2.2\ 10^{-3}$	3869	457.2
80	1.0	0.00	0.8 (v+dj)	WR	–	–	–	–	–	0.07	–	–	–	–	0.92	21.7	$1.4\ 10^{-3}$	3918	445.6
80	1.0	0.00	v+n	WR	2.95	–	–	–	–	1.57	–	–	–	–	2.34	13.7	$2.0\ 10^{-3}$	2646	767.7
80	1.0	0.20	0.6 (v+dj)	WR	–	–	–	–	–	0.07	–	–	–	–	0.80	26.3	$1.5\ 10^{-3}$	4151	413.5
80	1.0	0.50	0.6 (v+dj)	WR	–	–	–	–	–	0.09	–	–	–	–	0.71	31.6	$1.9\ 10^{-3}$	4039	355.4
80	1.0	0.80	0.6 (v+dj)	WR	–	–	–	–	–	0.11	–	–	–	–	0.82	27.6	$1.8\ 10^{-3}$	3884	394.3
100	1.0	0.00	0.8 (v+dj)	WR	0.33	–	–	–	–	0.22	–	–	–	–	1.12	23.6	$2.7\ 10^{-3}$	2957	411.9
100	1.0	0.00	v+n	WR	1.35	–	–	–	–	0.60	14.8	$3.7\ 10^{-3}$	2020	254.9	1.69	17.3	$3.7\ 10^{-3}$	2164	454.3
100	1.0	0.20	0.6 (v+dj)	WR	–	–	–	–	–	0.09	–	–	–	–	0.73	28.9	$1.7\ 10^{-3}$	4075	368.6
100	1.0	0.50	0.6 (v+dj)	WR	–	–	–	–	–	0.10	–	–	–	–	0.70	31.0	$1.9\ 10^{-3}$	4061	351.4
100	1.0	0.80	0.6 (v+dj)	WR	–	–	–	–	–	0.11	–	–	–	–	0.87	29.1	$1.9\ 10^{-3}$	3918	424.9

* A value is given whenever burning occurs convectively, otherwise − is given.
† Wave energy excited in units of 10^{46} erg; a value is given whenever convectively excited waves meet the super-Eddington and leakage conditions, otherwise − is given.
‡ A value is given whenever the super-Eddington, leakage and outflow conditions are met, otherwise − is given.

progenitors. Both multi-dimensional hydrodynamic simulations (like those by, e.g., Rogers et al. 2006; Browning et al. 2004) and observational constraints (as described in Chapter 3) would provide valuable constraints on the spectrum of wave excitation and thus how much of the full wave energy reservoir can reach the stellar envelope.

Multi-dimensional hydrodynamical simulations are also needed to better understand the behavior of super-Eddington stellar envelopes. Some authors, including Soker (2013), have suggested that envelope inflation is a more likely outcome than mass ejection or the formation of a super-Eddington wind, which we have argued for (Shaviv 2001; Owocki et al. 2004, have also argued for the latter). Detailed simulations would lead to better characterization of winds driven by a super-Eddington continuum that is, to order of magnitude, unable to energetically support the outflow implied by simple 1-D sonic point arguments.

Some of our progenitors are susceptible to wave-driven mass loss at multiple stages during their evolution to collapse. However, at each phase, we have investigated our 1-D stellar evolution model without any enhanced mass loss during prior phases. Future efforts to quantify the potential effect of wave-driven mass loss on the subsequent evolution of a star are necessary to understand the full evolution of progenitors that experience pre-SN outbursts. It is unclear how wave-driven mass loss events could affect the future evolution of the stellar core and envelope, and thus any potential further wave-driven mass loss.

Throughout our investigation, we have ignored the effect of rotation on the excitation, propagation and damping of waves. However, these effects may be important, especially for our rapidly rotating progenitors. The excitation of modes depends on the statistical properties of convection, which are different in rapidly rotating stars. Rotation also affects the shape of wave propagation cavities and can introduce critical damping layers (e.g., Rogers et al. 2012). We intend to investigate these potential effects in future work.

Acknowledgments

We would like to thank Bill Paxton for invaluable support with MESA. We would also like to thank David Arnett, Lars Bildsten, Matteo Cantiello, Tony Piro and Dan Kasen for fruitful discussions. JS would like to thank the organizers and attendees of the Workshop on Outstanding Problems in Massive Star Research - The Final Stages in Minneapolis, MN in 2012 for useful discussions. This work was partially supported by a Simons Investigator award from the Simons Foundation to EQ, the David and Lucile Packard Foundation, and the Thomas and Alison Schneider Chair in Physics at UC Berkeley. Further support was provided by NASA Headquarters under the NASA Earth and Space Science Fellowship Program - Grant 10-Astro10F-0030.

Appendix A: Massive star models

We use version 4789 of the `MESA star` stellar evolution code (Paxton et al. 2011) to construct evolutionary sequences of massive stars from the zero-age main sequence (ZAMS) to core collapse. We employed four separate inlists to evolve each progenitor from start to finish. The first generates ZAMS models. For masses below 30 $M_\odot$, we use the following non-default parameters

```
create_pre_main_sequence_model = .true.
mesh_delta_coeff = 0.5
Lnuc_div_L_upper_limit = 0.9
overshoot_f_above_burn_h = 0.335
overshoot_f0_above_burn_h = 0.
overshoot_step_fraction = 1.
```

with

```
relax_Z = .true.
new_Z = <value>
```

for non-solar metallicities and

```
change_rotation_flag = .true.
new_rotation_flag = .true.
set_omega_div_omega_crit = .true.
new_omega_div_omega_crit = <value>
```

for rotating models.

Above 30 $M_\odot$, we read in an analogous (in terms of rotation and metallicity) 30 $M_\odot$ model stopped at `Lnuc_div_L_upper_limit = 0.1` and use

```
relax_mass_scale = .true.
new_mass = <value>
```

instead of `create_pre_main_sequence_model = .true.`.

The next inlist evolves the ZAMS models through the main sequence using

```
change_v_flag = .true.
new_v_flag = .true.
set_rate_c12ag = 'Kunz'
set_rate_n14pg = 'Imbriani'
set_rate_3a = 'Fynbo'
kappa_file_prefix = 'gs98'
mesh_delta_coeff = 0.5
use_Type2_opacities = .true.
mixing_length_alpha = 1.5
use_Henyey_MLT = .true.
```

```
use_Ledoux_criterion = .true.
alpha_semiconvection = 0.1
thermo_haline_coeff = 2.0
T_mix_limit = 0
max_iter_for_resid_tol1 = 3
tol_residual_norm1 = 1d-5
max_tries = 50
max_tries_for_retry = 50
max_tries_after_backup = 50
max_tries_after_backup2 = 50
delta_lgL_He_limit = -1
delta_lgP_limit = -1
delta_lgTeff_limit = 0.5
delta_lgL_limit = 0.5
delta_lgRho_cntr_limit = 0.02
dX_nuc_drop_limit = 5d-3
```

with overshoot above the H-burning core turned on as during the pre-MS evolution above. The envelope is allowed to more efficiently mix using the "enhanced MLT" scheme with `okay_to_reduce_gradT_excess = .true.` and velocities are limited to the stellar core using

```
velocity_logT_lower_bound = 9
velocity_Z_lower_bound =  10
```

Resolution is increased by 0.4 in all transition regions. The mass loss schemes are either

```
RGB_wind_scheme = 'Dutch'
AGB_wind_scheme = 'Dutch'
Dutch_wind_lowT_scheme = 'de␣Jager'
RGB_to_AGB_wind_switch = 1d-4
```

or

```
RGB_wind_scheme = 'Dutch'
AGB_wind_scheme = 'Dutch'
Dutch_wind_lowT_scheme = 'Nieuwenhuijzen'
RGB_to_AGB_wind_switch = 1d-4
```

with `Dutch_wind_eta` set as described in §5.3. For rotating models, the diffusion coefficients for rotational mixing are set as the following

```
D_SH_factor =  0.0
D_SSI_factor = 1.16
D_ES_factor =  1.16
D_GSF_factor = 1.16
```

The models are stopped when they reach the end of the MS, controlled by the parameters

```
xa_central_lower_limit_species(1) = 'h1'
xa_central_lower_limit(1) = 1e-8
```

Beyond the MS, we turn off the overshoot by setting

```
overshoot_f_above_burn_h = 0.0
overshoot_f0_above_burn_h = 0.
overshoot_step_fraction = 0.
```

and evolve the models to central carbon exhaustion at

```
xa_central_lower_limit_species(1) = 'c12'
xa_central_lower_limit(1) = 1e-6
```

Finally, we run the models from neon and oxygen burning to core collapse at lower resolution by setting `mesh_delta_coeff = 1.0`.

This procedure works uninterrupted for the majority of our model grid. However, in some cases it was necessary to change a few of `MESA star`'s other parameters to aid convergence. For massive stars in which the envelope convection zone reaches deep down towards the hydrogen burning shell during post-ms evolution, we sometimes needed to increase `dH_div_H_limit` to allow relatively large changes in fractional hydrogen abundance due to the changing mesh at the convective boundary. In a few cases, we needed to increase solver tolerances (`tol_correction_norm` and `tol_max_correction`) to ten or 30 times the default during the final evolutionary phases to reach core collapse.

Bibliography

Aerts, C., Briquet, M., Degroote, P., Thoul, A., & van Hoolst, T. 2011, A&A, 534, A98

Aerts, C., Christensen-Dalsgaard, J., & Kurtz, D. W. 2010, Asteroseismology, 1st edn. (Springer), 866

Aerts, C., Puls, J., Godart, M., & Dupret, M.-A. 2009, A&A, 508, 409

Aizenman, M. L., & Cox, J. P. 1975, ApJ, 195, 175

Appenzeller, I. 1970, A&A, 9, 216

Appourchaux, T., Fröhlich, C., Andersen, B., et al. 2000, ApJ, 538, 401

Appourchaux, T., Belkacem, K., Broomhall, A.-M., et al. 2010, A&A Rev., 18, 197

Arnett, D., Meakin, C., & Young, P. A. 2009, ApJ, 690, 1715

Arnett, W. D., & Meakin, C. 2011, ApJ, 733, 78

Auvergne, M., Bodin, P., Boisnard, L., et al. 2009, A&A, 506, 411

Balona, L. A., Pigulski, A., Cat, P. D., et al. 2011, MNRAS, 413, 2403

Baraffe, I., Heger, A., & Woosley, S. E. 2001, ApJ, 550, 890

Beck, P. G., Bedding, T. R., Mosser, B., et al. 2011, Science, 332, 205

Bedding, T. R. 2011, ArXiv e-prints, arXiv:1107.1723 [astro-ph.SR]

Bedding, T. R., Mosser, B., Huber, D., et al. 2011, Nature, 471, 608

Belkacem, K., Samadi, R., Goupil, M.-J., & Dupret, M.-A. 2008, A&A, 478, 163

Belkacem, K., Samadi, R., Goupil, M. J., et al. 2009a, A&A, 494, 191

Belkacem, K., Samadi, R., Goupil, M.-J., et al. 2009b, Science, 324, 1540

Blomme, R., Mahy, L., Catala, C., et al. 2011, A&A, 533, A4

Böhm-Vitense, E. 1958, ZAp, 46, 108

Bouret, J.-C., Lanz, T., & Hillier, D. J. 2005, A&A, 438, 301

Briquet, M., Morel, T., Thoul, A., et al. 2007, MNRAS, 381, 1482

Brott, I., de Mink, S. E., Cantiello, M., et al. 2011, A&A, 530, A115

Browning, M. K., Brun, A. S., & Toomre, J. 2004, ApJ, 601, 512

Burbidge, E. M., Burbidge, G. R., Fowler, W. A., & Hoyle, F. 1957, Rev. Mod. Phys., 29, 547

Cantiello, M., Langer, N., Brott, I., et al. 2009, Astronomy and Astrophysics, 499, 279

Castor, J. I., Abbott, D. C., & Klein, R. I. 1975, ApJ, 195, 157

Chevalier, R. A. 2012, ApJ, 752, L2

Chevalier, R. A., & Fransson, C. 1994, ApJ, 420, 268

Chevalier, R. A., & Irwin, C. M. 2011, ApJ, 729, L6

Chomiuk, L., Chornock, R., Soderberg, A. M., Berger, E., & Chevalier, R. A. e. a. 2011, ApJ, 743, 114
Christensen-Dalsgaard, J. 2002, Reviews of Modern Physics, 74, 1073
—. 2008a, Ap&SS, 316, 113
—. 2008b, Ap&SS, 316, 113
Christensen-Dalsgaard, J., Monteiro, M. J. P. F. G., Rempel, M., & Thompson, M. J. 2011, MNRAS, 414, 1158
Chugai, N. N., & Danziger, I. J. 1994, MNRAS, 268, 173
Clayton, D. D. 1984, Principles of stellar evolution and nucleosynthesis. (Chicago: The University of Chicago Press)
Cox, J. P. 1980, Theory of stellar pulsation (Princeton: Princeton University Press)
De Cat, P. 2007, Communications in Asteroseismology, 150, 167
de Jager, C., Nieuwenhuijzen, H., & van der Hucht, K. A. 1988, A&AS, 72, 259
Dessart, L., Livne, E., & Waldman, R. 2010, MNRAS, 405, 2113
Dupret, M.-A., Belkacem, K., Samadi, R., et al. 2009, A&A, 506, 57
Dziembowski, W. 1977, Acta Astron., 27, 203
Eddington, A. S. 1926, The Internal Constitution of the Stars (Cambridge: Cambridge Univ. Press)
Eggleton, P. P. 1971, MNRAS, 151, 351
Falk, S. W., & Arnett, W. D. 1977, ApJS, 33, 515
Filippenko, A. V. 1997, ARA&A, 35, 309
Foley, R. J., Smith, N., Ganeshalingam, M., et al. 2007, ApJ, 657, L105
Fox, O. D., Filippenko, A. V., Skrutskie, M. F., et al. 2013, ArXiv e-prints, arXiv:1304.0248 [astro-ph.SR]
Fraser, M., Inserra, C., Jerkstrand, A., et al. 2013, ArXiv e-prints, arXiv:1303.3453 [astro-ph.SR]
Fullerton, A. W., Massa, D. L., & Prinja, R. K. 2006, ApJ, 637, 1025
Fynbo, H. O. U., Diget, C. A., Bergmann, U. C., et al. 2005, Nature, 433, 136
Gal-Yam, A. 2012, Science, 337, 927
Garcia Lopez, R. J., & Spruit, H. C. 1991, ApJ, 377, 268
Ginzburg, S., & Balberg, S. 2012, ApJ, 757, 178
Gizon, L., Birch, A. C., & Spruit, H. C. 2010, ARA&A, 48, 289
Glatzel, W. 1998, in Astronomical Society of the Pacific Conference Series, Vol. 135, A Half Century of Stellar Pulsation Interpretation, ed. J. P. Mutschlecner & D. S. King, 89
Glatzel, W. 2005, in Astronomical Society of the Pacific Conference Series, Vol. 332, The Fate of the Most Massive Stars, ed. R. Humphreys & K. Stanek, 22
Glatzel, W. 2008, in Astronomical Society of the Pacific Conference Series, Vol. 391, Hydrogen-Deficient Stars, ed. A. Werner & T. Rauch, 307
Glatzel, W., & Kiriakidis, M. 1993, MNRAS, 262, 85
Glatzel, W., Kiriakidis, M., Chernigovskij, S., & Fricke, K. J. 1999, MNRAS, 303, 116
Goldreich, P., & Kumar, P. 1990, ApJ, 363, 694

Goldreich, P., & Nicholson, P. D. 1977, Icarus, 30, 301
Grevesse, N., & Sauval, A. J. 1998, Space Sci. Rev., 85, 161
Heger, A., Fryer, C. L., Woosley, S. E., Langer, N., & Hartmann, D. H. 2003, ApJ, 591, 288
Heger, A., Langer, N., & Woosley, S. E. 2000, ApJ, 528, 368
Henyey, L. G., Forbes, J. E., & Gould, N. L. 1964, ApJ, 139, 306
Herwig, F. 2000, A&A, 360, 952
Humphreys, R. M., & Davidson, K. 1994, PASP, 106, 1025
Imbriani, G., Costantini, H., Formicola, A., et al. 2005, European Physical Journal A, 25, 455
Kawaler, S. D. 1988, ApJ, 334, 220
Kiewe, M., Gal-Yam, A., Arcavi, I., et al. 2012, ApJ, 744, 10
Kippenhahn, R., & Weigert, A. 1990, Stellar Structure and Evolution (Berlin: Springer Publishing House)
Koch, D. G., Borucki, W. J., Basri, G., et al. 2010, ApJ, 713, L79
Kumar, P., & Quataert, E. J. 1997, ApJ, 475, L143
Kumar, P., Quataert, E. J., & Bahcall, J. N. 1996, ApJ, 458, L83
Kumar, P., Talon, S., & Zahn, J. 1999, ApJ, 520, 859
Kunz, R., Fey, M., Jaeger, M., et al. 2002, ApJ, 567, 643
Lamers, H. J. G. L. M., & Cassinelli, J. P. 1999, Introduction to Stellar Winds (Cambridge: Cambridge University Press)
Langer, N., Fricke, K. J., & Sugimoto, D. 1983, A&A, 126, 207
Lebreton, Y., & Goupil, M. J. 2012, A&A, 544, L13
Lecoanet, D., & Quataert, E. 2013, MNRAS, 430, 2363
Ledoux, P. 1941, ApJ, 94, 537
Li, W., Leaman, J., Chornock, R., et al. 2011, MNRAS, 412, 1441
Maeder, A., & Meynet, G. 2000, ARA&A, 38, 143
Marigo, P., Girardi, L., Chiosi, C., & Wood, P. R. 2001, A&A, 371, 152
Massey, P. 2003, ARA&A, 41, 15
Mauerhan, J. C., Smith, N., Filippenko, A. V., et al. 2013, MNRAS, 430, 1801
McKee, C. F. 1986, Ap&SS, 118, 383
Meakin, C. A., & Arnett, D. 2006, The Astrophysical Journal, 637, L53, (c) 2006: The American Astronomical Society
Meakin, C. A., & Arnett, D. 2007, ApJ, 667, 448
Merryfield, W. J. 1995, ApJ, 444, 318
Miller, A. A., Smith, N., Li, W., et al. 2010, AJ, 139, 2218
Miller, A. A., Chornock, R., Perley, D. A., et al. 2009, ApJ, 690, 1303
Moriya, T. J., & Tominaga, N. 2012, ApJ, 747, 118
Murphy, J. W., Burrows, A., & Heger, A. 2004, ApJ, 615, 460
Nieuwenhuijzen, H., & de Jager, C. 1990, A&A, 231, 134
Noels, A. 1998, A Half Century of Stellar Pulsation Interpretation: A Tribute to Arthur N. Cox, 135, 400

Ofek, E. O., Cameron, P. B., Kasliwal, M. M., et al. 2007, ApJ, 659, L13
Ofek, E. O., Rabinak, I., Neill, J. D., et al. 2010, ApJ, 724, 1396
Ofek, E. O., Sullivan, M., Cenko, S. B., et al. 2013, Nature, 494, 65
Ogilvie, G. I., & Lesur, G. 2012, MNRAS, 422, 1975
Owocki, S. 2009, arXiv, astro-ph.SR, 0908.1565v2
Owocki, S. P., Gayley, K. G., & Shaviv, N. J. 2004, ApJ, 616, 525
Papaloizou, J. C. B. 1973, MNRAS, 162, 169
Pastorello, A., Smartt, S. J., Mattila, S., et al. 2007, Nature, 447, 829
Paxton, B., Bildsten, L., Dotter, A., et al. 2011, ApJS, 192, 3
Paxton, B., Cantiello, M., Arras, P., et al. 2013, ArXiv e-prints, arXiv:1301.0319 [astro-ph.SR]
Penev, K., Barranco, J., & Sasselov, D. 2009a, ApJ, 705, 285
Penev, K., & Sasselov, D. 2011, ApJ, 731, 67
Penev, K., Sasselov, D., Robinson, F., & Demarque, P. 2009b, ApJ, 704, 930
Press, W. H. 1981, ApJ, 245, 286
Quataert, E., & Shiode, J. 2012, MNRAS, 423, L92
Quimby, R. M., Kulkarni, S. R., Kasliwal, M. M., Gal-Yam, A., & Arcavi, I. e. a. 2011, Nature, 474, 487
Rakavy, G., Shaviv, G., & Zinamon, Z. 1967, ApJ, 150, 131
Rogers, F. J., & Iglesias, C. A. 1992, ApJS, 79, 507
Rogers, T. M., & Glatzmaier, G. A. 2005, MNRAS, 364, 1135
—. 2006, ApJ, 653, 756
Rogers, T. M., Glatzmaier, G. A., & Jones, C. A. 2006, ApJ, 653, 765
Rogers, T. M., Lin, D. N. C., & Lau, H. H. B. 2012, ApJ, 758, L6
Rosenblum, E., Garaud, P., Traxler, A., & Stellmach, S. 2011, ApJ, 731, 66
Saio, H. 2011, MNRAS, 412, 1814
Samadi, R., Belkacem, K., Goupil, M. J., et al. 2010, Ap&SS, 328, 253
Schlegel, E. M. 1990, MNRAS, 244, 269
Schwarzschild, M., & Härm, R. 1959, ApJ, 129, 637
Shaviv, N. J. 2001, Monthly Notices of the Royal Astronomical Society, 326, 126, (c) 2001 The Royal Astronomical Society
Shiode, J. H., Quataert, E., & Arras, P. 2012, MNRAS, 423, 3397
Shiode, J. H., Quataert, E., Cantiello, M., & Bildsten, L. 2013, MNRAS, 430, 1736
Simon, N. R., & Stothers, R. 1970, A&A, 6, 183
Simón-Díaz, S., Castro, N., Herrero, A., et al. 2011, ArXiv e-prints, arXiv:1111.1337 [astro-ph.SR]
Smartt, S. J. 2009, ARA&A, 47, 63
Smith, N. 2011, in IAU Symposium, Vol. 272, IAU Symposium, ed. C. Neiner, G. Wade, G. Meynet, & G. Peters, 571
Smith, N., Chornock, R., Silverman, J. M., Filippenko, A. V., & Foley, R. J. 2010, ApJ, 709, 856

Smith, N., Gehrz, R. D., Hinz, P. M., et al. 2003, AJ, 125, 1458
Smith, N., & McCray, R. 2007, ApJ, 671, L17
Smith, N., & Owocki, S. P. 2006, ApJ, 645, L45
Smith, N., Li, W., Foley, R. J., et al. 2007, ApJ, 666, 1116
Soker, N. 2013, ArXiv e-prints, arXiv:1302.5037 [astro-ph.HE]
Sonoi, T., & Shibahashi, H. 2012, PASJ, 64, 2
Sonoi, T., & Umeda, H. 2011, MNRAS, L389
Spruit, H. C. 2002, A&A, 381, 923
Suárez-Madrigal, A., Krumholz, M., & Ramirez-Ruiz, E. 2013, ArXiv e-prints, arXiv:1304.2317 [astro-ph.SR]
Turner, N. J., Yorke, H. W., Socrates, A., & Blaes, O. M. 2004, in Revista Mexicana de Astronomia y Astrofisica Conference Series, Vol. 22, Revista Mexicana de Astronomia y Astrofisica Conference Series, ed. G. Garcia-Segura, G. Tenorio-Tagle, J. Franco, & H. W. Yorke, 54
Unno, W., Osaki, Y., Ando, H., Saio, H., & Shibahashi, H. 1989, Nonradial oscillations of stars, 2nd ed. (Tokyo: University of Tokyo Press)
Uytterhoeven, K., Moya, A., Grigahcène, A., et al. 2011, A&A, 534, A125
Van Dyk, S. D., & Matheson, T. 2012, in Astrophysics and Space Science Library, Vol. 384, Astrophysics and Space Science Library, ed. K. Davidson & R. M. Humphreys, 249
Vink, J. S. 2011, Astrophysics and Space Science, 336, 163
Vink, J. S., de Koter, A., & Lamers, H. J. G. L. M. 2001, A&A, 369, 574
Winget, D. E., & Kepler, S. O. 2008, ARA&A, 46, 157
Wolff, S. C., Strom, S. E., Dror, D., Lanz, L., & Venn, K. 2006, AJ, 132, 749
Woosley, S. E., Heger, A., & Weaver, T. A. 2002, Reviews of Modern Physics, 74, 1015
Yoon, S.-C., & Cantiello, M. 2010, ApJ, 717, L62
Zahn, J.-P. 1989, A&A, 220, 112
Ziebarth, K. 1970, ApJ, 162, 947